

Iron spin crossovers at high pressures and temperatures and their effects on materials relevant to the Earth's lower mantle and core

Von der der Bayreuther Graduiertenschule für Mathematik und Naturwissenschaften
(BayNAT)

der Universität Bayreuth

zur Erlangung der Würde eines
Doktors der Naturwissenschaften

– Dr. rer. nat. –

genehmigte

Dissertation

Vorgelegt durch

Clemens Prescher, Dipl.-Min.

aus Weida

Bayreuth, 2012

Die vorliegende Arbeit wurde in der Zeit von November 2009 bis November 2012 in Bayreuth am Bayerischen Geoinstitut unter Betreuung von Herrn Prof. Dr. Falko Langenhorst und Prof. Dr. Leonid Dubrovinsky angefertigt.

Vollständiger Abdruck der von der Bayreuther Graduiertenschule für Mathematik und Naturwissenschaften (BayNAT) der Universität Bayreuth genehmigten Dissertation zur Erlangung des akademischen Grades eines Doktors der Naturwissenschaften (Dr. rer. nat.).

Dissertation eingereicht: 9.11.2012

Zulassung durch die Promotionskommission: 14.11.2012

Tag des wissenschaftlichen Kolloquiums: 22.02.2013

Amtierender Direktor:

Prof. Dr. Franz Xaver Schmid

Prüfungsausschuss:

Prof. Dr. Leonid Dubrovinsky (Erstgutachter)

Prof. Dr. Tomoo Katsura (Zweitgutachter)

Prof. Dr. Jürgen Senker (Vorsitzender)

Prof. Dr. Falko Langenhorst

Prof. Dr. Hans Keppler (Drittgutachter)

Dedicated to my brother Ronald who taught me so
much without ever saying any word.

RIP

Neither you nor anybody else knows with any certainty what is going on in the interior of this globe, since not the twelve thousandth part of its radius is known; science is eminently perfectible; and every new theory is soon routed by a newer.

(A journey to the center of the Earth, Jules Verne)

Abstract

Iron is the most abundant element by mass in the Earth. The iron content and its spin or oxidation state have a major influence on the physical properties of the main phases in the Earth's interior. Therefore it is of vast importance to understand the behavior of iron in mineral phases at the temperature and pressure conditions of the Earth's interior. This cumulative thesis investigates Fe spin crossovers in iron-containing magnesium aluminum silicates, iron-bearing silicate glasses, the iron carbide Fe_3C and the effect of Fe spin crossovers on the Fe/Mg partitioning between perovskite and ferropericlae in pyrolitic model system of the Earth's lower mantle. The goal is first to understand the nature of the Fe spin crossover in respect to its oxidation state and second to estimate the consequences of their occurrence to processes and the structure in the Earth. Central tools in these studies are laser heated diamond anvil cells, to reach the pressure and temperature conditions of the Earth's interior, Mössbauer spectroscopy, which is a sensitive probe for detecting structural and spin changes in Fe-bearing materials, and analytical transmission electron microscopy, as a probe of chemistry and oxidation state on the nm-scale. In this cumulative thesis I present the results of five research articles. For the analysis of conventional and recently developed synchrotron energy domain Mössbauer spectra the computer program *MossA* is introduced, which builds the basis for the analysis and interpretation of the results for the other studies. Based on synchrotron Mössbauer spectroscopy and electrical conductivity measurements of Fe-bearing silicate aluminum perovskite it is shown that Fe^{3+} occupies the dodecahedral A-site of the perovskite structure and remains in the high-spin state throughout the pressure and temperature conditions of the Earth's lower mantle. Furthermore, a study on the electronic behavior of Fe in a Fe^{2+} -rich aluminous silicate glass and a Fe^{3+} -rich sodium silicate glass infers that no sharp high spin to low spin crossover occurs in silicate melts in the Earth's lower mantle. This result excludes the possibility of negatively buoyant melts in the lower mantle in an early magma ocean solely due to strong preferential partitioning of iron into the melt phase, which would be induced by a Fe low-spin bearing melt. New insights into to decoupled partitioning behavior of Fe^{2+} and Fe^{3+} between the two dominant phases of the Earth's lower mantle, perovskite and ferropericlae, are presented. The intermediate spin to low spin crossover of Fe^{2+} in perovskite at about 110 GPa seems to have a strong effect on partitioning and oxidation state of Fe. It leads to a change of the partitioning behavior of Fe between perovskite and ferropericlae and induces a reduction of Fe^{3+} to Fe^{2+} in perovskite. Finally, a Mössbauer spectroscopic and single-crystal x-ray diffraction study of Fe_3C reveals a two-stage loss of magnetism in Fe_3C at high pressures at room temperature: a ferro- to paramagnetic transition around 8-10 GPa and a para- to nonmagnetic transition at about 22 GPa.

Zusammenfassung

Eisen ist bezogen auf die Masse das am häufigsten vorkommende Element in der Erde. Die Eisenkonzentration sowie Spin- und Oxidationszustände des Eisens haben einen starken Einfluss auf die physikalischen Eigenschaften der Hauptminerale des Erdinneren. Daher ist es von großer Bedeutung, das Verhalten von Eisen in Mineralen unter den Druck- und Temperaturbedingungen des Erdinneren zu verstehen. In der vorliegenden kumulativen Dissertation werden Spinübergänge in eisenhaltigen Magnesium-Aluminium-Silikaten, eisenhaltigen Silikatgläsern, dem Carbid Fe_3C und der Effekt dieser Übergänge auf die Fe/Mg-Verteilung zwischen Perowskit und Ferroperiklas in einem pyrolitischen Modellsystem des unteren Erdmantels untersucht. Das Ziel dieser Dissertation besteht zunächst darin, die Art der Spinübergänge des Eisens in Bezug zu seiner Wertigkeit zu verstehen und darauf aufbauend die Konsequenzen von Spinübergängen für die Prozesse und den Aufbau des Erdinneren abzuschätzen. Im Rahmen der Arbeit wurden hauptsächlich Laser-geheizte Diamantstempelzellen zum Erreichen der Druck- und Temperaturbedingungen, Mößbauer-Spektroskopie für die Bestimmung der strukturellen und Spinübergänge in eisenhaltigen Materialien und analytische Transmissionselektronenmikroskopie für die Bestimmung der Elementkonzentrationen sowie der Oxidationstufen des Eisens im nm-Maßstab genutzt. Die vorliegende kumulative Dissertation beinhaltet die Ergebnisse von fünf Einzelstudien. Es wird das Computerprogramm *MossA* eingeführt, das zur Analyse von konventionellen und energieaufgelösten Synchrotron Mössbauer-Spektren dient und damit die Basis für die Interpretation aller hier präsentierten Einzelstudien bildet. Auf der Grundlagen von Synchrotron Mössbauer-Spektroskopie und elektrischen Leitfähigkeitsmessungen von eisenhaltigem Aluminium-Silikat-Perowskit wird gezeigt, dass Fe^{3+} ausschließlich die dodekaedrisch koordinierte A-Position der Perowskit-Struktur besetzt und dass Fe^{3+} im High-Spin-Zustand unter den Druck- und Temperaturbedingungen des unteren Erdmantels bleibt. Des Weiteren zeigt eine Untersuchung des Spinzustands von Fe in Fe^{2+} -reichem Aluminium-Silikat-Glas und Fe^{3+} -reichem Natrium-Silikat-Glas, dass keine abrupten Spinübergänge des Eisens in Silikatschmelzen unter Bedingungen des unteren Erdmantels erfolgen. Durch diese Ergebnisse kann ausgeschlossen werden, dass Silikatschmelzen im unteren Erdmantel allein durch die starke Anreicherung von Fe relativ zur Festphase, welche durch die Stabilität von Fe im Low-Spin Zustand in der Silikatschmelze induziert würde, dichter wird als das umgebende Festgestein. Neue Erkenntnisse wurden über die Elementverteilung von Fe^{2+} und Fe^{3+} zwischen den beiden Hauptmineralphasen des unteren Erdmantels, Ferroperiklas und Perowskit, erzielt. Es wird gezeigt, dass der Übergang vom intermediären Spin-Zustand zum Low-Spin-Zustand von Fe^{2+} bei ca. 110 GPa einen starken Effekt auf die Elementverteilung und den Oxidationsstatus von Eisen hat. Dieser führt erstens zu einer Änderung der

Elementverteilung und verursacht des Weiteren eine Reduktion von Fe^{3+} zu Fe^{2+} im Perowskit. Zum Abschluss wird in einer Studie mittels Mössbauer-Spektroskopie und Einkristall-Röntgenbeugung gezeigt, dass Fe_3C seinen Magnetismus unter Druck bei Raumtemperatur in zwei Schritten verliert. Ein Übergang von ferro- zu paramagnetisch findet bei 8-10 GPa und ein Übergang von para- zu nicht-magnetisch findet bei ca. 22 GPa statt.

Acknowledgements

I thank my scientific advisors Prof. Dr. Falko Langenhorst and Prof. Dr. Leonid Dubrovinsky for their guidance, patience and especially their optimism. I am grateful that I had the opportunity to work with both and that they always encouraged me to come up with my own ideas. Further I also want to thank Dr. Catherine McCammon for her assistance with Mössbauer spectroscopy, the critical reviewing of my scientific manuscripts and her open door for all my questions to come. It was a great pleasure to work in the highly professional and well organized environment of the Bayerisches Geoinstitut. I thank all of its present and former members for the inspiring discussions. I want to especially thank Uwe Dittmann and Hubert Schulze for their outstanding sample preparation skills, Gertrud Gollner, Petra Buchert, Lydia Kison-Herzing, Detlef Krausse and Dr. Stefan Keyssner for their help and support. I am particularly grateful for the assistance of Dr. Nobuyoshi Miyajima during my TEM sessions. Dr. Kilian Pollok is thanked for the help provided in the FIB preparation. Dr. Tiziana Boffa Ballaran is thanked for her support in the X-ray diffraction laboratory and for the help with the analysis of single-crystal X-ray diffraction data. In addition I would like to offer my special thanks to Dr. Vitali Prakapenka, Dr. Marco Merlini, Dr. Alexander Chumakov and Dr. Michael Hanfland for their assistance during synchrotron radiation experiments. The research of my PhD was funded by the ENB program "Structure, Reactivity and Properties of Oxide Materials" of the Bavarian State Ministry of Science, Research and the Arts.

I would also like to thank my office mates and fellow colleagues for their support and friendship. Particular thanks go to Dr. Juliane Hopf, Dr. Geertje Ganskow, Dr. Linda Lerchbaumer, Antje Vogel, Mattia Giannini, Dr. Dennis Harries, Dr. Alexander Kurnosov, Dr. Konstantin Glazyrin and Dr. Yoichi Nakajima.

Explicitly I want to thank my parents Elke Künzel and Johannes Prescher for their constant support and trust. My deepest gratitude further goes to Amrei Pirzer for the wonderful time in the final year of my PhD.

Table of Contents

Abstract	4
Zusammenfassung	5
Acknowledgements.....	7
List of Figures	11
List of Tables	13
1 Introduction	14
1.1 Background and motivation	14
1.1.1 Structure and mineralogical composition of the Earth's interior.....	14
1.1.2 Oxidation state and spin state of Fe in the Earth's lower mantle	16
1.1.3 Motivation	18
1.2 Experimental methods	20
1.2.1 Laser heated diamond anvil cell technique	20
1.2.2 Powder and single crystal x-ray diffraction in a diamond anvil cell	22
1.2.3 Conventional and Synchrotron Mössbauer spectroscopy.....	23
1.2.4 Focused ion beam preparation.....	25
1.2.5 Transmission electron microscopy.....	27
1.3 Detailed summary and linkage of research studies	28
1.4 List of manuscripts and statement of author's contribution	34
2 MossA – a program for analyzing energy-domain Mössbauer spectra from conventional and synchrotron sources	36
2.1 Abstract.....	36
2.2 Introduction	36
2.3 Theory	37
2.4 Program features.....	38
2.5 Example workflow.....	40
2.6 Distribution	41

2.7	Acknowledgements.....	41
3	<i>Effect of iron oxidation state on the electrical conductivity of the Earth's lower mantle</i>	42
3.1	Abstract.....	42
3.2	Manuscript	42
3.3	Methods.....	48
3.4	Supplementary information	49
3.4.1	Synchrotron Mössbauer source.....	49
3.4.2	Sample synthesis.....	51
3.4.3	DAC experiments	51
3.4.4	Laser heating.....	52
3.4.5	SMS spectrum fitting.....	53
3.4.6	Cation site distribution in the perovskite structure	55
3.4.7	Electrical conductivity measurements.....	56
4	<i>Iron spin state in silicate glass at high pressure: implications for melts in the Earth's lower mantle</i>	58
4.1	Abstract.....	58
4.2	Introduction	58
4.3	Experimental details.....	59
4.4	Results.....	61
4.5	Discussion.....	63
4.6	Acknowledgements.....	67
5	<i>The effect of Fe spin crossovers on its partitioning behavior and oxidation state in a pyrolitic Earth's lower mantle system.....</i>	69
5.1	Abstract.....	69
5.2	Manuscript	69
5.3	Materials and methods	74

6	<i>Structurally hidden magnetic transitions in Fe₃C at high pressures</i>	78
6.1	Abstract.....	78
6.2	Introduction	78
6.3	Experimental details.....	79
6.4	Results and Discussion	80
6.5	Conclusion.....	84
6.6	Acknowledgements.....	84
6.7	Supplementary information	85
7	<i>References</i>	90
	Erklärung.....	101

List of Figures

Chapter 1

<i>Figure 1-1</i> Mineral volume fraction of the Earth's mantle in pyrolite model composition.....	15
<i>Figure 1-2</i> Diagrams for the crystal field splitting of iron in octahedral and dodecahedral sites.....	17
<i>Figure 1-3</i> Schematic drawing of a four-pin modified Merrill-Bassett diamond anvil cell	21
<i>Figure 1-4</i> Hyperfine interactions for ^{57}Fe nuclei	24
<i>Figure 1-5</i> Focused ion beam and secondary electron pictures of the sample preparation for TEM.	26
<i>Figure 1-6</i> Example electron energy loss spectrum (EELS) of the Fe $L_{2,3}$ edge in perovskite.....	28

Chapter 2

<i>Figure 2-1</i> Calibration of the FWHM of a Lorentzian-squared source line	39
<i>Figure 2-2</i> MossA user interface during the fitting process.	40

Chapter 3

<i>Figure 3-1</i> SMS spectra of $\text{Mg}_{0.6}\text{Fe}_{0.4}\text{Si}_{0.63}\text{Al}_{0.37}\text{O}_3$ perovskite at room temperature showing their evolution with pressure.....	44
<i>Figure 3-2</i> Pressure variation of FeAlPv hyperfine parameters (CS and QS).....	45
<i>Figure 3-3</i> Relative change of electrical conductivity of FeAlPv as a function of pressure	47
<i>Figure 3-S1</i> Optical scheme for SMS experiment for high-pressure studies..	50
<i>Figure 3-S2</i> SMS spectrum of 25 μm thick natural α -iron foil used for energy calibration.....	51
<i>Figure 3-S3</i> SMS spectrum of $\text{K}_2\text{Mg}^{57}\text{Fe}(\text{CN})_6$ used to monitor the source linewidth.	51
<i>Figure 3-S4</i> Room temperature Mössbauer spectra of FeAlPv samples at high pressure	54
<i>Figure 3-S5</i> Room temperature Mössbauer spectra of $\text{Mg}_{0.78}\text{Fe}_{0.2}\text{Al}_{0.05}\text{Si}_{0.97}\text{O}_3$ perovskite at 86 GPa taken before and after laser heating.....	55
<i>Figure 3-S6</i> Influence of pressure on the resistance of $\text{Mg}_{0.60}\text{Fe}_{0.40}\text{Si}_{0.63}\text{Al}_{0.37}\text{O}_3$ perovskite	57

Chapter 4

<i>Figure 4-1</i> Selected Mössbauer spectra of the F2B glass and variation in CS and QS of Fe^{2+} with pressure.....	61
<i>Figure 4-2</i> Selected Mössbauer spectra of the NFS glass.	62
<i>Figure 4-3</i> Variation of CS and QS for Fe^{2+} and Fe^{3+} with pressure in NFS glass	63
<i>Figure 4-4</i> Variation of CS and QS for Fe^{2+} and Fe^{3+} in glasses.	66

Chapter 5

Figure 5-1 Variations of the Fe-Mg K_D and Fe^{2+} -Mg K_D between Mg-Pv and Fp in pyrolite.....	71
Figure 5-2 $Fe^{3+}/\Sigma Fe$ ratios for Pv and Fp with pressure.	72
Figure 5-S1 Calculated Fe^{3+} -Mg K_D between Mg-Pv and Fp in pyrolite.....	77
Figure 5-S2 Incorporation mechanism of Fe^{3+} and Al in Mg-Pv.	77

Chapter 6

Figure 6-1 Volume-pressure data for Fe_3C	81
Figure 6-2 Selected ambient temperature Mössbauer spectra of Fe_3C at high pressure.	82
Figure 6-3 Variation of CS and BHF of Fe_3C with pressure.....	83
Figure 6-S1 Crystal structure of Fe_3C	85
Figure 6-S2 Variation of FWHM of Fe_3C	88
Figure 6-S3 Calculated change in mean squared velocity of Fe_3C due to the ferromagnetic to paramagnetic transition.	88
Figure 6-S4 Evolution of Fe-Fe distances in Fe_3C with pressure.....	89
Figure 6-S5 Variation of mean carbon-iron distance with pressure.....	89

List of Tables

Chapter 3

Table 3-S1 Experimental details and sample compositions.....52

Chapter 5

Table 5-S1 Experimental conditions of the laser heated diamond anvil cell experiments.....76

Table 5-S2 Element compositions of Fp and Mg-Pv.....76

Chapter 6

Table 6-S1 Results of single crystal X-ray diffraction refinement of Fe₃C at different pressures.86

1 Introduction

1.1 Background and motivation

1.1.1 Structure and mineralogical composition of the Earth's interior

The interior of the Earth is ideally considered to be layered into several shells, which are defined by their chemical, elastic or rheological properties. The most widely used models for the Earth's interior come from global inversion of seismological data, e.g. the “preliminary reference Earth model” (PREM) (Dziewonski and Anderson, 1981). The division into layers is based on discontinuous changes in seismic P-wave and S-wave velocities, which are induced by phase transformations of major rock-forming minerals (Fig. 1-1) or a complete change in chemistry.

The Earth's interior can be divided into three main geospheres: the crust, the mantle and the core. The continental crust and the oceanic crust have an average thickness of 35 km and 7 km, respectively. The transition from the crust to the Earth's mantle is marked by a change from crustal rocks to a peridotitic upper mantle composition, thus, there is a change in chemistry and in physical properties, such as density and elasticity.

The Earth's mantle extending down to 2890 km depth is subdivided into an upper and a lower mantle based on structural phase transformations of the olivine $(\text{Mg,Fe})_2\text{SiO}_4$ component. In the upper mantle olivine is stable up to 410 km, where it then transforms to its high pressure polymorph – wadsleyite with a modified spinel structure. At a depth of ~520 km wadsleyite transforms to a spinel-structured phase – ringwoodite. The border between the upper and lower mantle occurs at ~660 km depth, where ringwoodite disproportionates into $(\text{Mg,Fe})\text{O}$ ferropericlae (Fp) and $(\text{Mg,Fe})(\text{Si,Al})\text{O}_3$ magnesium silicate perovskite (Mg-Pv). The depth range from 410 km down to 660 km is called the transition zone. The remaining non-olivine components of the Earth's upper mantle (cpx – clinopyroxene and opx – orthopyroxene) undergo gradual transitions with depth, which are smeared out over several tens of kilometers (Fig. 1-1). Those phase transformations, therefore, lead only to changes in slope of the seismic velocity curves versus depth rather than causing discontinuities. The mineralogy of the Earth's lower mantle in contrast is relatively simple; the modal abundances are ~7% CaSiO_3 calcium perovskite, ~13% Fp and 80% Mg-Pv. A distinct layer was found at the base of the lower mantle at ~2600 km depth called D''. It is possibly caused by a phase transition of the Mg-Pv to post-perovskite phase (PPv) (Murakami et al., 2004). The PPv structure is composed of stacked SiO_6 octahedral sheets along the b-

Chapter 1 Introduction

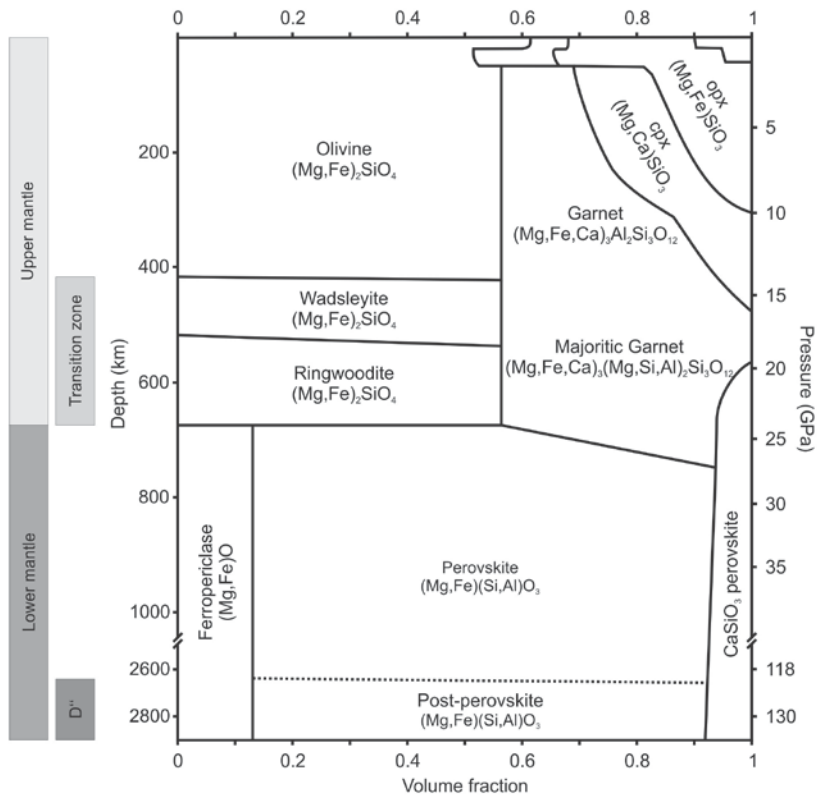


Figure 1-1 Mineral volume fraction of the Earth's mantle in pyrolite model composition (Ringwood, 1991; Stixrude and Lithgow-Bertelloni, 2005, 2011). Modified after Frost (2008). opx – orthopyroxene; cpx – clinopyroxene.

axis. The Mg^{2+} and Fe^{2+} cations are located in between the octahedral layers. The structure is similar to that of CaIrO_3 .

The Earth's core ranges from 2890 km depth to the center of the Earth at 6371 km depth. It is divided into two parts: (1) a liquid outer core, through which shear waves cannot pass, and (2) a solid inner core. Based on cosmo-chemical abundances of the elements in the solar system, meteoritic records and mean density of the Earth, the core is suggested to be primarily composed of a $\text{Fe}_{1-x}\text{Ni}_x$ ($0.5 \text{ wt.\%} \leq x \leq 20 \text{ wt.\%}$) alloy. However, the density of this alloy is slightly higher than the densities estimated from seismic wave velocities of the Earth's core. The relative density deficits of the core to solid iron vary from 6%-10% for the outer core (Stevenson, 1981; Anderson and Isaak, 2002), and 1% to 3% for the inner core (Jephcoat and Olson, 1987; Shearer and Masters, 1990; Stixrude et al., 1997; Dubrovinsky et al., 2000). The density deficit can be explained by the addition of light elements alloying with the $\text{Fe}_{1-x}\text{Ni}_x$ alloy. From cosmo-chemical constraints several suitable candidates have been proposed: H, O, C, S, Si and N (Allègre et al., 1995; McDonough and Sun, 1995) and several iron oxides, carbides and nitrides are

Chapter 1 Introduction

known to occur in iron-meteorites, which are believed to resemble planetary cores. However, till now there has been no final conclusion which light element or elements are accounting for the density deficit in the Earth's core (McSween, 1999).

1.1.2 Oxidation state and spin state of Fe in the Earth's lower mantle

As discussed in the previous section, the mineralogical composition of the Earth's lower mantle is considered to be relatively homogeneous. However, more and more detailed studies of seismic wave velocities in the Earth's lower mantle discover small anomalies which cannot be attributed to remnant slabs or ascending plumes (e.g. Trampert et al., 2004). In the last decade Fe spin crossovers, which occur at pressure and temperature conditions of the Earth's lower mantle, have been proposed to provide possible explanations for these anomalies (e.g. Badro et al., 2003).

The oxidation state of iron in Fp is mainly Fe^{2+} with a minor contribution of Fe^{3+} (2-15 %). Fe^{2+} in Fp occupies octahedral coordinated sites resulting in a splitting of the five 3d energy levels split into three lower t_{2g} and two higher e_g energy levels (Fig. 1-2). The energy levels are separated by the crystal field splitting energy Δ_c (Burns, 1993). At low pressures the high spin (HS) configuration with two paired and four unpaired electrons is stable. However, with increasing pressure Δ_c increases and at a certain pressure becomes larger than the spin-pairing energy, which makes the low spin (LS) configuration (6 paired electrons occupying the t_{2g} levels) energetically more favorable. The onset of this spin crossover has been estimated to be at ~ 50 GPa at room temperature (Badro et al., 2003a; Lin et al., 2005). Nevertheless, the spin crossover of Fe^{2+} is expected to occur over a very large pressure/depth interval due to iron-iron interactions, small variations in coordination environments between different iron atoms and thermal broadening. The Fe^{2+} HS-LS spin crossover region at geotherm temperatures has been estimated to occur from ~ 60 GPa to ~ 120 GPa (Sturhahn et al., 2005; Lin, Vankó, et al., 2007; Mao et al., 2011). So far there have been no reports of spin transitions of Fe^{3+} in Fp at high pressures and temperatures.

The most abundant phase in the Earth's lower mantle, Mg-Pv ($\text{Mg,Fe}(\text{Si,Al})\text{O}_3$), contains iron in Fe^{2+} and Fe^{3+} oxidation state. The Fe^{3+} content is either charge balanced by (1) oxygen vacancies when Fe^{3+} is occupying the octahedral B-site or (2) by charge coupled substitution of $\text{Fe}^{3+}\text{-Al}^{3+}$ for $\text{Mg}^{2+}\text{-Si}^{4+}$ (Lauterbach et al., 2000; Frost and Langenhorst, 2002), whereby the latter seems to be more favorable at higher pressures and with higher concentrations of Fe^{3+} and Al. The Fe^{3+} content in Mg-Pv is primarily controlled by its Al content (McCammon, 1997; Lauterbach et al., 2000; Frost and Langenhorst, 2002) and is contrary to expectations independent of oxygen fugacity (Frost et al., 2004). The ABO_3 Mg-Pv structure exhibits a dodecahedrally coordinated A-site and an octahedral coordinated B-Site. Fe^{2+} only

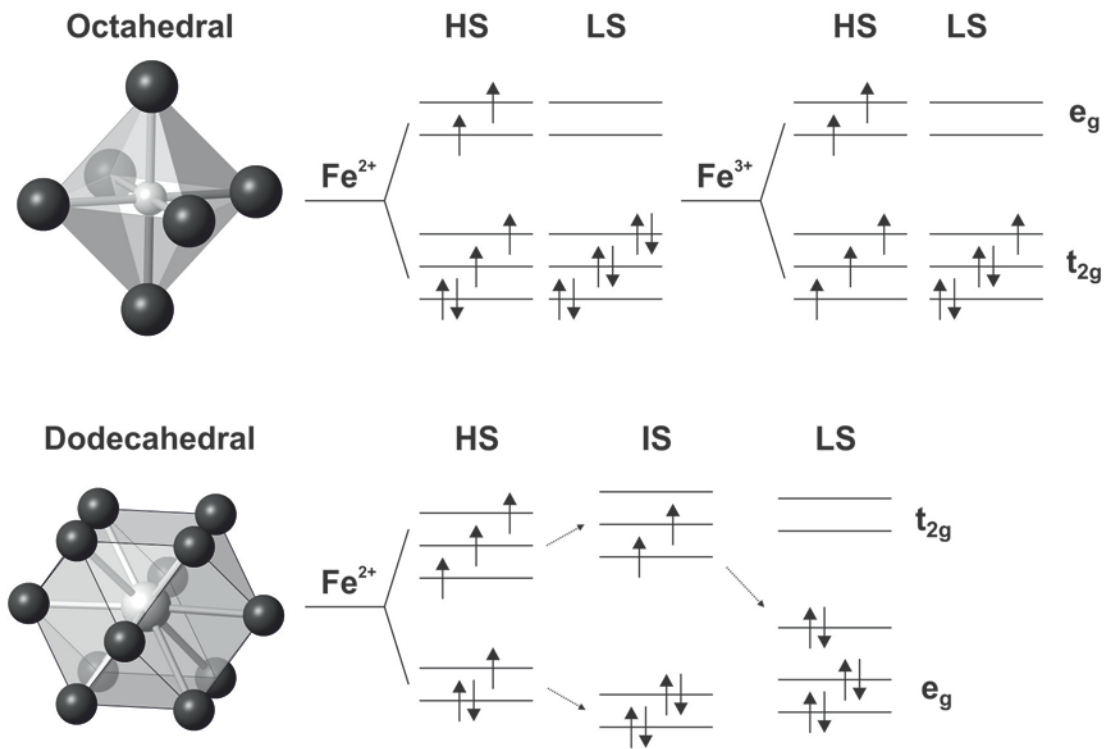


Figure 1-2 Diagrams for the crystal field splitting of iron in octahedral and dodecahedral sites occurring in minerals of the Earth's lower-mantle. Electronic configurations for iron as (2+) or (3+) are shown for high-spin (HS), intermediate-spin (IS) (dodecahedral site) and low-spin (LS). Modified after Lin and Wheat (2011).

occupies the dodecahedrally coordinated A-site. This coordination environment leads to a splitting of the five 3d electron energy levels into two lower e_g and three higher t_{2g} energy levels (Fig. 1-2) (Burns, 1993). This energy splitting leads to three possible spin configurations: (1) HS state with four unpaired and two paired electrons; (2) intermediate spin state with four paired and two unpaired electrons; and (3) LS state with 6 paired electrons. On the contrary, Fe^{3+} has been reported to occupy the dodecahedrally coordinated A-site and/or the octahedrally coordinated B-site of the Mg-Pv structure. For Fe^{3+} only two spin configurations are stable in either of both environments: (1) HS state with five unpaired electrons and (2) LS state with four paired and one unpaired electron. The reported spin crossovers of Fe^{2+} and Fe^{3+} are less consistent with each other than in Fp. Some authors propose an onset of a gradual Fe^{2+} HS-IS crossover at 35 GPa with Fe^{3+} staying in HS state (McCammon et al., 2008; Narygina et al., 2009), whereas others suggest that Fe^{2+} and Fe^{3+} occupying the A-site remain in HS state, and only Fe^{3+} occupying the B-site undergoes HS-LS crossover at 40-60 GPa (Jackson et al., 2005; Catalli et al., 2010,

Chapter 1 Introduction

2011). Additionally, it has been proposed that Fe^{2+} becomes LS in Mg-Pv at about 110 GPa at high temperatures (McCammon et al., 2010).

1.1.3 Motivation

The main goal of this thesis is to understand the electronic behavior of iron on the physical properties of materials in the Earth's lower mantle and the Earth's core. We therefore investigated the physical and chemical consequences of spin crossovers in several case studies.

Since the present results on spin crossovers in Mg-Pv are quite controversial with regard to the nature of spin transitions, we decided to apply a new synchrotron-based method of Mössbauer spectroscopy (SMS) to four different Mg-Pv compositions. SMS enables the collection of Mössbauer spectra with an acquisition time of several minutes of samples in a diamond anvil cell (compared to several days for conventional Mössbauer spectroscopy). The short collection time allows the measurement of energy domain Mössbauer spectroscopy in the diamond anvil cell with in-situ laser heating, with which it is possible to reach all pressure and temperature conditions present in the Earth's lower mantle.

One of the possible effects of Fe spin crossovers in Fp and Mg-Pv is the preferential partitioning of Fe into the LS bearing phase due to a gain in energy caused by the volume reduction from HS or IS to LS state. This would primarily change the Fe/Mg ratio in the co-existing minerals, resulting in changes in density, elasticity, electrical and thermal conductivity of the lower mantle assemblage due to spin crossover itself and the accompanied Mg/Fe ratio changes in Fp and Mg-Pv. It was, for example, proposed that Fe would preferentially partition into LS bearing Fp relative to HS or IS Fe-bearing Mg-Pv (Badro et al., 2003a). However, the results of experimental determinations on the partitioning behavior of Fe/Mg between Mg-Pv and Fp are diverse and partially in contradiction to each other. Some authors propose a change in partitioning behavior due to HS-LS crossover in Fp at ~40 GPa in a pyrolitic model composition (Irifune et al., 2010), whereas others report a change in partitioning behavior above ~70 GPa in a simplified MgO-FeO-SiO₂ system (16, 17). On the other hand the results of (Sinmyo et al., 2008) and (Kesson et al., 2002; Murakami et al., 2005) lack any discontinuity at the P,T conditions of the Earth's lower mantle in simplified and pyrolitic systems, respectively. Another important factor controlling the partitioning behavior of Fe is its oxidation state. In Al bearing systems Fe^{3+} is stabilized in the Mg-Pv structure which increases its Fe content relative to Fp (Frost and Langenhorst, 2002). All of the previous investigations on the partitioning behavior of Fe between Fp and Mg-Pv at conditions of the Earth's lower mantle have reported results for bulk iron content in the constituting minerals, without paying

Chapter 1 Introduction

special attention to iron oxidation state. However, the Fe^{3+} content is a major factor determining the elasticity (Glazyrin et al., subm.) and thermal conductivity (Goncharov et al., 2009; Goncharov, Prakapenka, et al., 2010) of Mg-Pv and Fp. Therefore, we decided to study the decoupled Fe^{2+} and Fe^{3+} partitioning coefficients between Mg-Pv and Fp in a pyrolitic lower mantle model composition by using laser heated diamond anvil cells, focused ion beam preparation of the recovered samples and transmission electron microscopy for chemical and oxidation state analyses. The main goal was to study possible effects of Fe^{2+} or Fe^{3+} spin crossovers in Fp and Mg-Pv on the partitioning behavior, which in turn should also change the $\text{Fe}^{3+}/\Sigma\text{Fe}$ ratio in the constituting minerals.

The present day Earth's lower mantle is believed to be mostly solid apart from some small possible melt fractions near the core mantle boundary (CMB) (Williams and Garnero, 1996; Lay et al., 2004). However, e.g. the moon-forming impact is believed to have induced a whole Earth magma ocean (Tonks and Melosh, 1993; Agnor et al., 1999). In such an environment, the density contrast between the on cooling crystallizing solids and remaining melt is a major factor influencing chemical stratification of the entire Earth. A recent study observed a sharp discontinuity in the pressure dependence of the Fe/Mg solid/melt partition at 75 GPa, resulting in a strong enrichment of Fe in the melt, which would produce a denser negatively buoyant melt. The sharp discontinuity was explained by an iron spin crossover seen in their XES data collected on $(\text{Mg}_{0.95}\text{Fe}_{0.05})\text{SiO}_3$ glass during room temperature compression. However, Andrault et al. (2012) reported a much lower degree of iron enrichment in silicate melt based on partitioning experiments at liquidus temperatures on a (Ca,Mg,Al,Si,Fe) oxide glass with chondritic composition, resulting in a melt that would be lighter than the surrounding mantle and hence would segregate upwards. In order to reconcile the difference between the results of Nomura et al. (2011) and Andrault et al. (2012), we decided to perform a Mössbauer spectroscopy study of a Fe^{2+} -rich and a Fe^{3+} -rich silicate glass measured *in situ* in a diamond anvil cell at high pressure. Mössbauer spectroscopy is a much more sensitive probe for detecting structural and spin changes in Fe-bearing materials than partitioning experiments, which can only give indirect indications of the iron spin state.

In order to understand which and to what extent specific light elements are present in the Earth's core it is of primary importance to understand possible phases of Fe with the respective light elements. Two iron carbides exist as possible carbon bearing phases in the Earth's core with different Fe-C ratio: Fe_3C and Fe_7C_3 . Both minerals are magnetic at ambient condition and undergo magnetic phase transitions at high pressures and temperatures. To extrapolate and obtain physical properties of these phases at the temperature and pressure conditions of the Earth's core it is of vast importance to understand the nature of the magnetic transitions at high pressures. However, despite the large number

Chapter 1 Introduction

of investigations, the transition pressure from the ferromagnetic state to the paramagnetic or nonmagnetic state is still highly debated. Investigations directly probing the atomic or electronic structure of iron revealed transition pressures of ~ 6 GPa by synchrotron Mössbauer spectroscopy (nuclear forward scattering) (Gao et al., 2008), 6-10 GPa by Fe K-edge x-ray magnetic circular dichroism (XMCD) (Duman et al., 2005) and 25 GPa by x-ray emission spectroscopy (Lin et al., 2004); whereas, by means of indirect methods, several different effects at higher pressures were observed which the investigators attributed to a change in the electronic state of iron: a softening of phonon frequencies observed by inelastic x-ray scattering around 68 GPa (Fiquet et al., 2009) and a change in behavior of lattice parameters above 55 GPa observed by x-ray diffraction (Ono and Mibe, 2010). Furthermore, *ab initio* calculations suggest that the nonmagnetic state becomes stable only above 60 GPa (Vocadlo et al., 2002). The span of the transition pressure range is too large to be attributed to different pressure calibrations or experimental uncertainties. If we assume that different investigations employed the same well-characterized iron carbide starting material, the only plausible explanation for the discrepancies is that different investigations probed different transitions in Fe_3C that led to different observable effects which only can be detected by specific methods. In order to clarify these transition(s), we decided to perform a Mössbauer spectroscopic and single-crystal x-ray diffraction study of Fe_3C at high pressure in a diamond anvil cell.

1.2 Experimental methods

This section gives a brief introduction to the main experimental techniques deployed in the research presented in this cumulative dissertation. Further details of operation of these and other conventional methods are given in the respective following chapters.

1.2.1 Laser heated diamond anvil cell technique

In order to understand the dynamics and properties of the Earth, we need to experimentally reproduce the conditions of the Earth's interior. These extreme conditions by means of very high pressure and temperatures can be achieved by employing the laser heated diamond anvil cell ((LH)-DAC) technique. The LHDAC allows studying materials under almost all pressure and temperature conditions relevant for the Earth's interior. It is possible to reach pressures as high as 300 GPa and temperatures as high as 6000 K simultaneously (Chandra Shekar et al., 2003).

A DAC consists of two opposing brilliant-cut diamonds mounted on metallic plates, whereby the sample sits in between the culets surrounded by a gasket material (Fig. 1-3). The pressure is increased by

Chapter 1 Introduction

tightening screws between the two metal plates and forcing the two opposed anvils together and therefore pressurizing the μm -sized sample. To transform the uniaxial pressure supplied by this mechanism, usually a pressure transmitting medium, such as noble gases or a mixture of methanol and ethanol, is used. The pressure inside the sample chamber can be evaluated by either using the fluorescence of a ruby crystal (Mao et al., 1986), measured with Raman spectroscopy, or by measuring the lattice parameters of a simple cubic material, such as Au, Ne, or MgO, and estimating the pressure using its known equation of state (Fei et al., 2007).

A unique advantage of the DAC as a static high-pressure apparatus is the transparency of diamond to electromagnetic radiation in a very broad range of the electromagnetic spectrum. Diamond is only opaque between 5 eV and 5 keV. This makes it possible to do in-situ measurements radiation in the energy range of microwaves, the far infrared (IR), visible (VIS), ultraviolet (UV) up to 5 eV and with x-rays and γ -rays above 5 KeV again. These energy ranges make it possible to measure e.g. Raman spectroscopy, infrared spectroscopy, Brillouin spectroscopy, x-ray diffraction, Mössbauer spectroscopy, x-ray inelastic scattering, or nuclear inelastic scattering in-situ at high pressure and temperature.

High temperatures in a DAC can be achieved by using either an external resistive heating or a laser heating system. In the resistive heating technique a large portion of the DAC is also heated which leads to a maximum achievable stable temperature of about 1000 K (Dubrovinskaia and Dubrovinsky, 2003) at relative low pressures due to softening of the DAC components. It is very stable and accurate in temperature, however the maximum temperature is too low to experimentally reproduce all pressure and temperature conditions in the Earth's interior. In the laser heating technique only a small part of the sample is heated, which makes it possible to access temperatures in excess of 6000 K (Chandra Shekar et

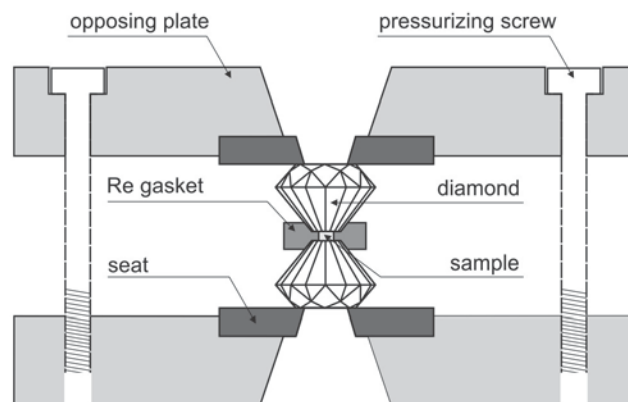


Figure 1-3 Schematic drawing of a four-pin modified Merrill-Bassett diamond anvil cell.

Chapter 1 Introduction

al., 2003). However, laser heating usually results in high temperature gradients in the sample chamber, which can lead to thermally induced diffusion (Sinmyo et al., 2011) or lateral movement of the sample. Several attempts have been made to decrease temperature gradients and stabilize laser heating in the DAC. Double sided laser heating is used to reduce the vertical gradient, and on the other side lateral gradients are reduced by transforming the Gaussian shaped laser beam to a flat top by inserting a Pi-shaper into the beam path.

In the studies presented in this work two types of DACs were used, either a modified Merrill-Basett type with opposed four-pin plates or a piston cylinder type. Culet sizes were varied according to the desired pressures which were investigated. For the high pressure experiments above 90 GPa beveled culets were used. A portable double sided laser system (Dubrovinsky et al., 2009) was used at ID09a and ID18 at the European synchrotron radiation facility (ESRF) in Grenoble, France and the installed double sided laser heating facility at GSECARS at the advanced photon source (APS) in Chicago, USA, was used for the experiments conducted there.

1.2.2 Powder and single crystal x-ray diffraction in a diamond anvil cell

X-ray diffraction (XRD) is a basic method probing the long-range order of crystalline materials. Powder XRD has long been used as the main method for studying crystal structures in-situ at high pressure and temperature in a DAC. The basic relation of XRD is Bragg's law $\lambda = 2d \sin\theta$, where λ is the x-ray wavelength, d is the crystallographic interplanar spacing and θ is the diffraction angle. By determining d-spacings of different lattice planes (hkl) the unit cell parameters of a known structure can be estimated. The variation in unit cell parameters with pressure is then used to determine P-V(-T) equations of states. With this information it is possible to model densities of different phases in the Earth's interior and to compare them with the densities estimated from seismic wave velocities (Dziewonski and Anderson, 1981).

With single crystal X-ray diffraction (SXRD) it is possible to do a full structural refinement of the crystal lattice. Subtle changes in atomic coordinates can be detected and related to structural or magnetic transitions. In the last decade SXRD in a DAC has been advanced to achieve almost the whole pressure range of the lower mantle and additionally it is now possible to perform SXRD in combination with laser-heating (Dubrovinsky et al., 2010a). A strong advantage of SXRD in DACs over powder diffraction is that only a single small grain (e.g. $10 \times 10 \times 5 \mu\text{m}^3$) is measured and no stresses develop due to the compaction of several grains lying above each other. This results in a better apparent hydrostaticity

Chapter 1 Introduction

and therefore more precise lattice parameters even without a full structural refinement of the atomic positions.

In this work we used powder XRD mainly for phase analysis and SXRD for full structural refinement and determinations of the equation of state. Angle dispersive XRD powder diffraction was conducted at GSECARS at the APS in Chicago, USA; and angle dispersive SXRD was conducted at ID09a at the ESRF in Grenoble, France. The two dimensional powder XRD scans were integrated using Fit2D software (Hammersley, 1997) and processed with the GSAS software package (Larson and Von Dreele, 2004). The SXRD data was processed using the CRYMALIS software [Oxford Diffraction (2006) CrysAlis RED, Version 1.171.31.8 Oxford Diffraction Ltd., Abingdon, Oxfordshire, UK] and the crystal structure refinements of integrated intensities were carried out using SHELX-97 WinGX version (Sheldrick, 2008).

1.2.3 Conventional and Synchrotron Mössbauer spectroscopy

Mössbauer spectroscopy allows the study of the local atomic environment around Mössbauer active atoms in a solid. It has an extremely high energy resolution which makes it possible to detect small changes in the atomic environment. It is able to distinguish between different oxidation and spin states of iron; furthermore it provides structural information such as on the coordination and geometry of crystallographic sites. However, it is a short-range probe and is only sensitive to the first two coordination shells at most. The physical principle of the Mössbauer effect is the recoilless absorption of γ -rays in solids (Mössbauer, 1958).

A Mössbauer apparatus is relatively simple and is composed of three parts, a source, an absorber and a detector. In conventional ^{57}Fe Mössbauer spectroscopy the source is a radioactive parent of the Mössbauer atom embedded in an Rh matrix producing γ -rays through nuclear decay. A usual source diameter for ^{57}Co sources is in the order of 1 cm. A smaller source with higher density of ^{57}Co in the matrix is used for high pressure studies, a so called “point-source”, which has a diameter of 0.5 mm (McCammon, 1994). The energy of the source radiation is modulated by accelerating the source back and forth, making use of the Doppler Effect. Another possibility to produce source radiation is the use of a synchrotron radiation facility. There are two techniques developed: (1) the sample is illuminated by a polychromatic white beam, inducing all ^{57}Fe to get to the excited state and monitoring the decay (Rüffer and Chumakov, 1996) or (2) using the nuclear Bragg refraction of a FeBO_3 single crystal, producing a highly monochromatic beam which is comparable to the width of γ -ray produced by natural decay of ^{57}Co (Potapkin et al., 2012). Method (1) is more difficult to analyze since the Mössbauer spectrum is recorded in the frequency domain, whereas in method (2) the Mössbauer spectrum is recorded in the

Chapter 1 Introduction

energy domain and can be analyzed in a similar way to conventional Mössbauer spectroscopy. The only difference is the lineshape of the source function, which has to be included in the fitting of the spectra.

Synchrotron Mössbauer studies are extremely versatile in the field of high pressure and high temperature science. The small beam size, which is on the order of $20 \times 20 \mu\text{m}^2$ and the relatively low acquisitions times ($\sim 5\text{-}30$ min) compared to conventional Mössbauer ($\sim 0.5\text{-}7$ days) make it possible to study the high pressure and high temperature behavior of materials simultaneously, by employing laser heating diamond anvil cell techniques. This enables the possibility to study Earth relevant materials at all conditions present in the Earth's interior.

An ^{57}Fe Mössbauer spectrum of a specific atomic site is defined by 3 different hyperfine parameters, center shift (CS), quadrupole splitting (QS) and magnetic hyperfine splitting (BHF) (Fig. 1-4) (McCammon, 2000). The CS is decomposed into two contributions, the isomer shift (IS) and the second order Doppler shift (SOD). The IS arises through the electric monopole interaction between the positive

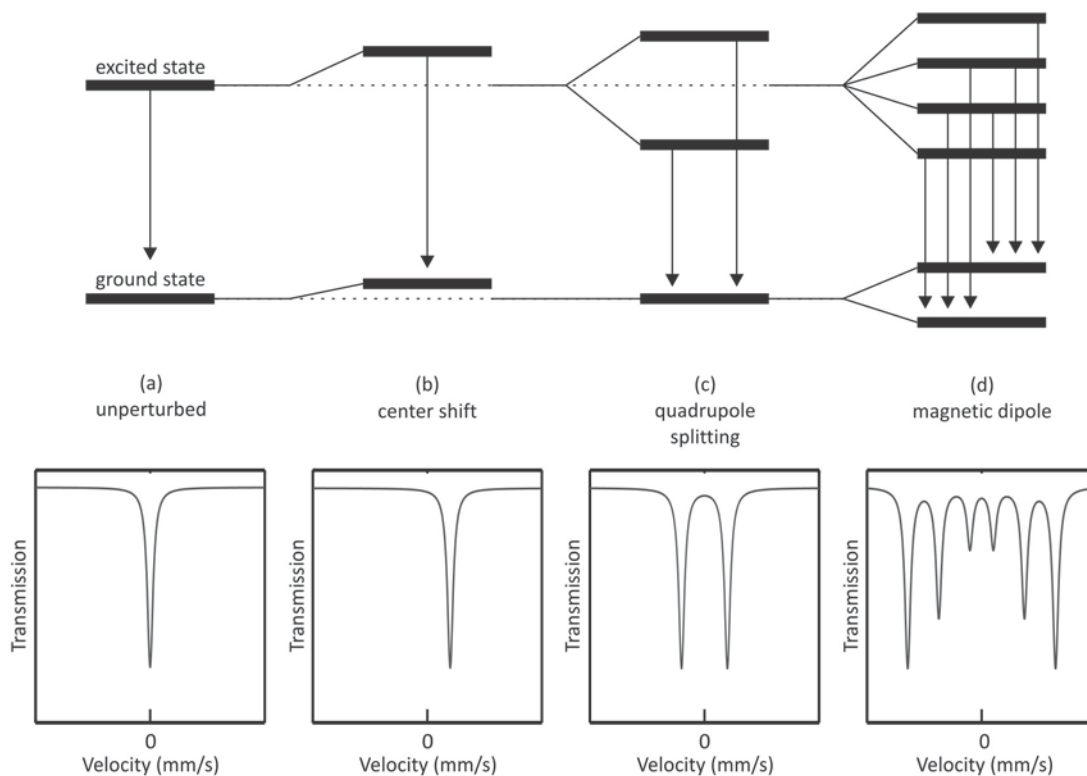


Figure 1-4 Hyperfine interactions for ^{57}Fe nuclei, showing the nuclear energy level diagram for (a) an unperturbed nucleus; (b) a change in center shift; (c) with quadrupole splitting; and (d) with magnetic dipole interaction. Each interaction is accompanied with a resulting Mössbauer spectrum. Modified after McCammon (2000).

Chapter 1 Introduction

nuclear charge and the electric field of the surrounding electrons. This results in a shift of the nuclear energy levels compared to an unperturbed nucleus. The magnitude of the shift is a function of difference in s-electron densities between the source and the absorber nuclei. The SOD arises due to atomic vibrations and is a function of temperature and the mean square velocities of the source and absorber nuclei. The QS is a measure of electric field gradient (EFG) at the nucleus. The EFG arises through a lattice term and a valence term (Ingalls, 1964). The lattice term comes from the deviation of cubic symmetry of the surrounding atoms in the crystalline lattice and the valence term comes from the asymmetry in the charge distribution of the valence electrons. For ^{57}Fe the interaction between the quadrupolar moment and the EFG splits the excited state into two levels, giving rise to a doublet with equal component linewidths and areas in the ideal random absorber case. The third parameter, BHF, arises through a dipole interaction between the magnetic field at the nucleus and the nuclear magnetic dipole moment. This causes a splitting of the nuclear energy states. For ^{57}Fe this results in a splitting of the ground state into two levels and the excited state into four levels, giving eight possible transitions. Only six transitions are allowed to occur taking into account magnetic dipole interaction selection rules. In the ideal random absorber case that gives a sextet with equal component linewidths and relative line areas with a 3:2:1:1:2:3 ratios.

CS, QS and BHF parameters of individual ^{57}Fe sites can be used as fingerprints to determine the oxidation state, coordination number or spin state. Area ratios of different sites in one material are used to assign the occupancy of iron in specific crystallographic sites and for determining the Fe^{3+} to Fe^{2+} ratio. Discontinuities in the CS, QS and BHF as function of pressure enable the detection of either a phase changes or spin crossover.

Mössbauer spectra presented in this work were either recorded in transmission mode on a constant acceleration point source Mössbauer spectrometer (McCammon, 1994) or by using synchrotron Mössbauer spectroscopy in the energy domain at ID18 at ESRF (Potapkin et al., 2012). All samples were enriched in ^{57}Fe , due to the small sample size in a DAC and the strong absorption of γ -photons by the diamond anvils. The velocity scales were calibrated relative to 25 μm Fe-foil and the spectra were fitted using the MossA software package (Prescher et al., 2012).

1.2.4 Focused ion beam preparation

In a focused ion beam (FIB) instrument an ion beam is scanned over the sample comparable to the electron beam scanning in a scanning electron microscope (SEM). A liquid metal ion source (LIMS), which is commonly a gallium source due to its low melting point ($\sim 30^\circ\text{C}$) and low vapor pressure

Chapter 1 Introduction

(Volkert and Minor, 2007), is used as source for the generation of ions. The ions are then accelerated by an electric field with energies of typically 2-30 kV and focused by electrostatic lenses. The beam interaction of the ions with the sample produces secondary electron similar to the process in an electron beam. These electrons can be detected to produce an image. However, the physically possible image resolution in modern FIB microscopes is with a lateral resolution of 10 μm higher than in a conventional SEM (Volkert and Minor, 2007).

The large size and momentum of the ions in a FIB is inherently leading to an ejection of the sample's surface atoms. However, this at first view negative effect has been made advantageous to do microscale machining of samples surfaces by combining the high resolution, controllability, and sputtering efficiency of FIB instruments. A particularly important capability of this method is the preparation of <100 nm thin lamellae for transmission electron microscope (TEM) studies. TEM slices can be obtained from selected areas of the sample which was previously very difficult or even impossible by conventional methods (e.g. milling, ultramicrotomy). This is especially useful for the preparation of samples recovered from DAC experiments. The selective capability of the FIB extraction method makes it possible to sample specifically the laser-heated part of the DAC sample (Fig. 1-5(a)).

In this work a FEI Quanta3D field-emission FIB-SEM dual beam equipped with a Pt GIS and an Omniprobe micromanipulator was used at the Institute of Geoscience, University of Jena. This instrument combines a FIB and a SEM in order to use both techniques simultaneously. The gas injection system (GIS) enables an FIB assisted chemical vapor deposition of Pt. The deposited Pt provides protection to the sample and is used as 'glue' during the extraction process (Fig. 1-5(b)). The Omniprobe

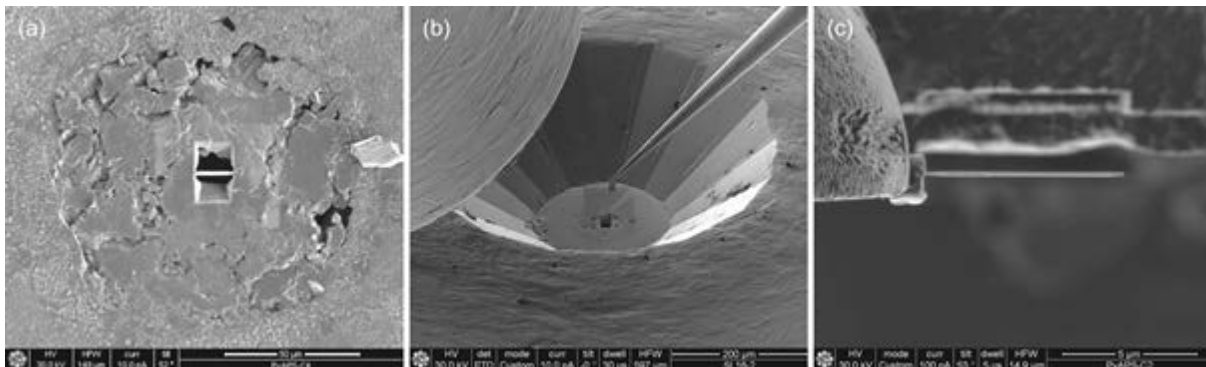


Figure 1-5 Focused ion beam and secondary electron pictures of the sample preparation for TEM. **(a)** Two trenches removed in the front and in back of the sampling position, which is protected by a layer of Pt. **(b)** Sample lift out from the gasket. **(c)** The slice is thinned to 30-100 nm thickness.

Chapter 1 Introduction

micromanipulator enables the lift-out of the sample and the attachment of the sample to a TEM copper grid where it is milled further to electron transparency (Fig. 1-5(c)).

1.2.5 Transmission electron microscopy

A transmission electron microscope (TEM) enables the structural and chemical investigation of a sample on nm scale. In a TEM electrons are accelerated with an energy of 100 to 400 keV towards the sample, whereby the sample has to be thinned to electron transparency prior to investigation (see FIB section). A wide variety of interactions occur due to the electron-sample collision, which can be used to obtain different information of the probed sample. In this work we mainly used 2 techniques: energy dispersive x-ray microanalysis (EDS) and electron energy loss spectroscopy (EELS).

EDS is used for obtaining the chemical composition of a sample. The incident electron beam ejects inner shell electrons of atoms creating an electron hole. An outer shell electron then fills the hole releasing an x-ray photon with energy similar to the energy difference between both shells, whereby those energy differences are characteristic for each element due to the different atomic structures and energy levels. By detecting the amount and energy of the different emitted x-ray photons it is possible to obtain the chemical composition. However, direct quantification of the EDS spectrum is difficult due to self-absorption of x-ray photons, whereby the degree of absorption depends on the composition, density and thickness of the sample. Therefore, usually standards with a chemical composition close to the measured sample composition are used as reference materials. In this work we used the method of van Cappellen and Doukhan (1994) to correct for absorption effects. This method is especially developed for ionic compounds. It is based on the principle of electro-neutrality of the specimen. It varies the thickness parameter in the absorption correction until the sum of all anions and cations times their respective valence state cancels out.

EELS makes use of the inelastic scattering of the transmitted electrons during electron-sample interaction, whereby the amount of energy loss is characteristic for each element in the sample. Furthermore, the fine structure of the energy-loss spectrum is sensitive to the coordination environment and oxidation state of the particular element. This enables the determination of oxidation state of elements by comparison with measurements of reference materials with known oxidation state. In this work the method of van Aken and Liebscher (2002) was employed to quantify the oxidation state of Fe by using the Fe $L_{2,3}$ edge fine structure. The $Fe^{3+}/\Sigma Fe$ ratio is determined by either fitting the L_3 edge with several Gaussian components or using the white line intensity ratio between the $Fe^{3+} L_3$ and $Fe^{2+} L_2$ edge (Fig. 1-6).

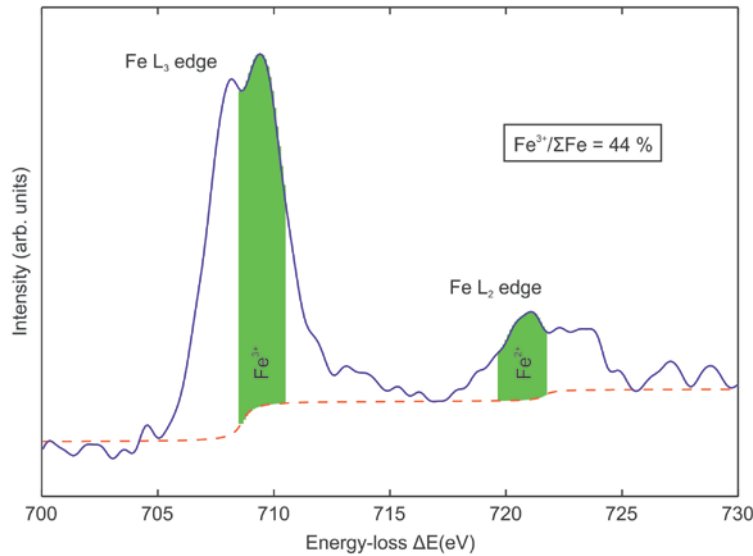


Figure 1-6 Example electron energy loss spectrum (EELS) of the Fe L_{2,3} edge in perovskite. Green areas show the integration windows for the quantification method of Fe³⁺/ΣFe after van Aken and Liebscher (2002).

In this work we employed a PHILIPS CM20 FEG (field emission gun) STEM operating at 200 kV. Compositions were measured using a ThermoNoran Vantage energy-dispersive (EDS) system equipped with a Norvar ultra-thin window and a germanium detector. EELS measurements were performed using a Gatan PEELS 666 (parallel electron energy-loss spectrometer).

1.3 Detailed summary and linkage of research studies

The overall focus of this dissertation is to understand the nature and effect of iron spin crossovers on the physical properties of materials proposed to be present in the deep Earth's interior. This includes changes in physical properties such as elasticity and electrical conductivity in the particular Fe bearing material where the spin crossover occurs and affects the partitioning behavior of Fe between coexisting iron bearing phases present in a multiphase assemblage.

In this cumulative dissertation I present the results of five research articles. The first article introduces a new program for analyzing energy domain Mössbauer spectra from conventional and synchrotron source (Chapter 2), which has been an important analytical tool for the 4 other studies. In the second article we investigate the spin state of Fe²⁺ and Fe³⁺ in Fe-containing magnesium aluminium silicate perovskite and the effect on the electrical conductivity (Chapter 3). Article three explores the possibility of Fe²⁺ and Fe³⁺ spin crossovers at high pressures in silicate glasses, which serve as analogue materials for the behavior of melts in the Earth's interior (Chapter 4). The effect of Fe spin crossovers on

Chapter 1 Introduction

its partitioning behavior and oxidation state in a model pyrolite lower mantle composition has been determined in Article four (Chapter 5) and the last article investigates the nature of electronic transitions at high pressures in Fe_3C , a candidate for a carbon bearing phase in the Earth's core (Chapter 6).

Chapter 2 (published in the *Journal of Applied Crystallography*) introduces the Mössbauer fitting program *MossA* written in the *MATLAB* programming language. The program exhibits an easy-to-use graphical user interface with several features enabling a straightforward approach to the fitting process of the sometimes very complex Mössbauer spectra. The fitting of such spectra is especially dependent on the initial guess of the model. In *MossA* e.g. it is possible to define an initial model visually and observing the fitting process in real time. *MossA* aids in the data analysis process by providing built-in routines and additional controllable graphical user interfaces for the folding and calibration of Mössbauer spectra. Furthermore, it contains special fitting and calibration routines for energy-domain Mössbauer spectra from synchrotron sources, which was recently developed at beamline ID18 at the European synchrotron radiation facility (ESRF), Grenoble (Potapkin et al., 2012).

In some cases an unconstrained fit, letting all parameters vary, leads to a physically improbable result. In *MossA* it is therefore possible to keep parameters constant, constrain parameters to fall within specific ranges, or even linearly couple several parameters. An application of the last feature is when there is information about site occupancy from crystallographical or crystal chemical considerations is available, which constrains the abundance relationships between the different sites of a phase. Detailed information of the program can be found in chapter 2.

Chapter 3 (submitted to *Nature Communications*) presents a study on the spin state of Fe in iron-containing magnesium aluminium silicate perovskite (FeAlPv). We collected energy-domain synchrotron Mössbauer spectra (Potapkin et al., 2012) of 4 different FeAlPv compositions at room temperature and pressures up to 122 GPa using diamond anvil cells, with or without laser annealing of the samples. The hyperfine parameters (center shift (CS) and quadrupole splitting (QS)) for Fe^{3+} in all samples are the same within experimental error, and there is no change in $\text{Fe}^{3+}/\Sigma\text{Fe}$ ratio for the individual samples over the entire pressure range. The hyperfine parameters of the Fe^{3+} doublet are consistent with Fe^{3+} being in high spin (HS) state (Greenwood and Gibb, 1971), and their smooth variation with pressure indicates that Fe^{3+} does not undergo any spin transition within the entire pressure range. The weighted mean QS for Fe^{2+} in all samples increases dramatically with pressure, which arises from a decreasing intensity of the low QS Fe^{2+} doublet corresponding to the HS state (McCammon et al., 2008), and an increasing intensity

Chapter 1 Introduction

of the high QS doublet which can be assigned to the intermediate spin (IS) state (Lin et al., 2008; McCammon et al., 2008).

Single-crystal X-ray refinements (Glazyrin et al., *subm.*) and crystal chemical calculations have shown that Fe^{3+} occupies only the A-site of the perovskite structure in our samples. Hence, our data demonstrates that Fe^{2+} undergoes a HS-IS crossover and Fe^{3+}_A remains in HS state. However, several publications (Catalli et al., 2010, 2011; Fujino et al., 2012) have suggested that reduced volume of the low spin (LS) Fe^{3+} in the octahedral coordinated B-site of the FeAlPv structure would lead to a redistribution of Fe^{3+} from the A- to the B-site within the lower mantle. To test this hypothesis, we laser annealed 2 samples at a number of pressures and collected SMS spectra both during and after heating. The hyperfine parameters remain unchanged after a number of heating cycles and we therefore conclude that there is no exchange of Fe^{3+} between the A- and B-site at lower mantle pressures and temperatures.

In addition to the SMS measurements we performed high-pressure high-temperature electrical conductivity measurements on a mainly Fe^{3+} bearing FeAlPv ($\text{Fe}^{3+}/\Sigma\text{Fe}=93\%$). The results show a continuous increase in electrical conductivity with pressure. Previous, measurements on electrical conductivity on single phase $\text{Mg}_{0.9}\text{Fe}_{0.1}\text{SiO}_3$ perovskite (Ohta et al., 2008; Ohta, Hirose, Shimizu, et al., 2010) and a pyrolitic mantle assemblage (Ohta, Hirose, Ichiki, et al., 2010) show a decrease in conductivity above 50 GPa, which they attribute to a HS-LS transition of Fe^{3+} . However, this explanation can be ruled out by the results in the present work. The drop in electrical conductivity has to be explained by the HS-IS crossover of Fe^{2+} . Our data shows that the $\text{Fe}^{3+}/\Sigma\text{Fe}$ ratio in FeAlPv is an important factor determining the thermal conductivity of the Earth's lower mantle at mid-mantle depths (1200-1900 km).

Chapter 4 (submitted to *Earth and Planetary Science Letters*) reports a Mössbauer spectroscopic study of a Fe^{2+} -rich aluminous silicate (NFS) glass and a Fe^{3+} -rich sodium silicate (NFS) glass measured in a diamond anvil cell up to 84 GPa. It is experimentally very challenging to stabilize melts at the temperature and pressure conditions of the Earth's mantle. Therefore, we used silicate glasses as analogue materials for the liquid state and explored the spin state of Fe^{2+} and Fe^{3+} in silicate glasses at high pressures. The variations in center shift (CS) and quadrupole splitting (QS) vary smoothly with pressure and are consistent with a gradual increase in coordination number of Fe with pressure. Both, Fe^{2+} and Fe^{3+} , remain in the high spin state and show no evidence of spin crossover over the measured pressure range.

Chapter 1 Introduction

Partitioning behavior of Fe between solid and melt would be strongly influenced by a discontinuous change in spin state in either of those phases. Indeed, a recent study reported a very sharp discontinuity in the pressure dependence of the Fe/Mg in solid/melt partitioning behavior in a San Carlos Olivine composition $[(\text{Mg}_{0.9}\text{Fe}_{0.1})_2\text{SiO}_4]$ at 76 GPa, resulting in a strong enrichment of Fe in the melt, which would produce a denser negatively buoyant melt. The sharp discontinuity was explained by an iron spin crossover seen in their XES data collected on $(\text{Mg}_{0.95}\text{Fe}_{0.05})\text{SiO}_3$ glass during room temperature compression (Nomura et al., 2011). However, Andrault et al. (2012) reported a much lower degree of iron enrichment in silicate melt based on partitioning experiments at liquidus temperatures on a (Ca,Mg,Al,Si,Fe) oxide glass with chondritic composition, resulting in a melt that would be lighter than the surrounding mantle and hence would segregate upwards.

Our measurements of the Fe^{2+} and Fe^{3+} spin state in silicate glasses do not fully cover the pressure range of the Earth's lower mantle. A spin crossover may eventually occur at the base of the lower mantle, however, a strong thermal broadening due to Boltzmann statistics of the crossover region infers that no sharp spin crossover would be expected at P,T conditions down to the base of the lower mantle. Our results therefore support the study of Andrault et al. (2012), which excludes the possibility of a negatively buoyant melts in a chondritic Earth's lower mantle solely due to strong preferential partitioning of iron into the melt phase.

Chapter 5 (for submission to *Science*) examines the partitioning behavior of major elements between the 2 dominant phases in the Earth's lower mantle, Mg-silicate perovskite (Mg-Pv) and ferropericlase (Fp). Especially the concentration of iron and its oxidation state in both phases are fundamental for understanding the structure and dynamics of the Earth's interior. Both factors may significantly influence densities, elasticity and transport properties such as electrical and thermal conductivity. Previous investigations on the behavior of Fe partitioning covering the P,T conditions of the Earth's lower mantle have reported partitioning coefficients $[K_D = (\text{Fe}/\text{Mg})_{\text{Mg-Pv}}/(\text{Fe}/\text{Mg})_{\text{Fp}}]$ between Mg-Pv and Fp for bulk iron contents in the constituting minerals, without paying special attention to iron oxidation state. However, the Fe^{3+} content is a major factor determining the elasticity (Glazyrin et al., subm.) and thermal conductivity (Goncharov et al., 2009; Goncharov, Struzhkin, et al., 2010) of Mg-Pv and Fp.

In this study we present bulk iron and decoupled Fe^{2+} , Fe^{3+} partitioning coefficients between Mg-Pv and Fp $[K_D = (\text{Fe}/\text{Mg})_{\text{Mg-Pv}}/(\text{Fe}/\text{Mg})_{\text{Fp}}]$ at P,T conditions of the Earth's lower mantle. The bulk Fe K_D first decreases linearly with pressure from 0.58 at 26 GPa to 0.45 at 79 GPa, then suddenly increases to 0.57

Chapter 1 Introduction

at 97 GPa and decreases again to 0.48 at 130 GPa. The discontinuous change of K_D at 97 GPa is accompanied with a decrease of $Fe^{3+}/\Sigma Fe$ ratio in Mg-Pv from 50(5) % at 79 GPa to 30 % at 97 GPa, whereby the bulk iron concentration stays constant. Therefore, the Fe^{2+} K_D shows an even more amplified discontinuous step at this pressure. Recently, it was shown that Fe^{2+} in Mg-Pv undergoes a intermediate spin (IS) to low spin (LS) crossover at about 110 GPa (McCammon et al., 2010). A relatively narrow IS to LS crossover would result in a preferential partitioning of Fe^{2+} into Mg-Pv due to a change in atomic radii. This then results in an increase in K_D which is exactly what can be seen in the behavior of the bulk Fe and Fe^{2+} K_D at about 97 GPa. We furthermore propose that the IS-LS crossover not only affects the partitioning behavior, it also may cause a self-reduction of Fe^{3+} to Fe^{2+} in Mg-Pv. The Fe^{3+} content of Mg-Pv is mainly controlled by its Al content due to coupled substitution of $(Mg^{2+}, Fe^{2+})-Si^{4+}$ with $Fe^{3+}-Al^{3+}$ (e.g. (Lauterbach et al., 2000; Frost and Langenhorst, 2002)). It seems that this relationship is reversed at high pressure due to the Fe^{2+} IS-LS crossover. The coupled substitution is still dominant, although that the self-reduction of Fe^{3+} to Fe^{2+} now controls the Al content in Mg-Pv, which is decreased at 97 GPa and 130 GPa.

The reduction of Fe^{3+} to Fe^{2+} needs to be balanced by oxidation of some other components. Diamond or volatile species such as CH_4 or H_2 could be oxidized to form CO_2 or H_2O . In the DAC experiments probably the diamond anvils were the reaction partner; however, the budget of those components in the Earth's lower mantle is too low (probably on the order of 2000 p.p.m. (Wood et al., 1996)) to account for the reduction alone. A more realistic scenario for the Earth would be that the amount of metallic Fe by disproportionation of Fe^{2+} (Frost et al., 2004) during crystallization of an early magma ocean is reduced at this depth.

Another important effect of the change in Fe^{3+} content of Mg-Pv is the induced change in thermal conductivity. It has been shown that the radiative contribution of the thermal conductivity in Mg-Pv mainly depends on its Fe^{3+} content due to $Fe^{2+}-Fe^{3+}$ and $Fe^{3+}-O^{2-}$ charge transfer bands (Goncharov et al., 2009; Goncharov, Struzhkin, et al., 2010). A decrease of Fe^{3+} content at 97 GPa will increase the thermal conductivity, creating a discontinuity which could act as thermal boundary layer between the mid-lower mantle and the lowermost lower mantle.

Chapter 6 (published in *Physical Review B Rapid Communications*) comprises a study on the spin state of Fe in Fe_3C at high pressure. By using diamond anvil cells we carried out ^{57}Fe Mössbauer spectroscopy of Fe_3C up to 88 GPa. The detailed analysis of the Mössbauer spectra reveals two regions of discontinuity. The first exhibits a loss of magnetic hyperfine splitting (BHF) at around 10 GPa, with an

Chapter 1 Introduction

accompanied increase and following decrease in center shift (CS), and the second is shown by a change in pressure dependence of the CS at about 22 GPa. In order to clarify whether those discontinuities are induced by electronic transitions or by structural changes we further performed single-crystal x-ray diffraction (SXR) of Fe_3C up to 47 GPa. Based on the refined unit-cell parameters and atomic positions, we found no evidence of a structural transition up to the highest pressure achieved. Distances between iron atoms and between iron and carbon atoms decrease continuously with pressure. Solely the evolution of the unit-cell volume with pressure shows a change in compressibility at ~ 24 GPa.

The increase of CS at the ferro- to paramagnetic transition is consistent with a phonon softening. CS is influenced by two effects – the chemical isomer shift (IS) (which is a measure of s-electron density at the nucleus) and the second-order Doppler shift (SOD) (which is a measure of mean-squared velocities of the Mössbauer active atoms). An increase in chemical isomer shift is contrary to the expected increase in s-electron density at the nucleus with increasing pressure (IS decreases with increasing s-electron density). Thus, the increase in CS can only be explained by a change in SOD.

By combining the Mössbauer spectroscopy and SXR results we propose a two stage loss of magnetism in Fe_3C at high pressure: a ferro- to paramagnetic transition around 8-10 GPa and a high-spin (HS) to low-spin (LS) crossover at about 22 GPa (para- to nonmagnetic). The results reconcile previous conflicting reports on magnetic transitions in Fe_3C . The ferro- to paramagnetic transition corresponds to the transition observed in nuclear forward scattering (Gao et al., 2008) and Fe K-edge x-ray magnetic circular dichroism (Duman et al., 2005), while the HS-LS crossover is consistent with the transition observed in x-ray emission spectroscopy (Lin et al., 2004).

The results are important for geophysical modeling of physical properties of Fe_3C to the P,T conditions of the Earth's core. Only the properties of the nonmagnetic phase should be used for extrapolation to these conditions. Chapter 6 provides further information and the detailed analysis of the elasticity of Fe_3C .

1.4 List of manuscripts and statement of author's contribution

[1] Prescher, C., McCammon, C., Dubrovinsky, L., 2012. MossA: a program for analyzing energy-domain Mössbauer spectra from conventional and synchrotron sources. *Journal of Applied Crystallography* (2012) 45, 329–331.

C. Prescher (CP) wrote the program. CP, C. McCammon (CM) and L. Dubrovinsky (LD) tested, improved the program and analyzed the data. CP and CM wrote the manuscript.

[2] Potapkin, V., McCammon, C., Glazyrin, K., Kantor, A., Kuppenko, I., Prescher, C., Sinmyo, R., Smirnov, G., Chumakov, A., Ruffer, R. and Dubrovinsky, L. Effect of iron oxidation state on the electrical conductivity of the Earth's lower mantle. *Submitted to Nature Communications*.

The SMS methodology was developed by VP, G. Smirnov (GV), AC and R. Ruffer (RR), and the research project was designed and directed by CM and LD. Samples were synthesized by RS and characterized by VP, RS, KG, LD, and CM. The data were collected by VP, CM, LD, KG, AK, IK, CP and AC. The analysis of SMS was performed by VP, CM, CP and AC. LD performed the electric conductivity measurements. VP and CM did final interpretation of the results and wrote the manuscript, with help from other co-authors.

[3] Prescher, C., Weigel, C., McCammon, C., Dubrovinsky, L., Narygina, O., Potapkin, V., Kuppenko, I., Sinmyo, R., Chumakov, A. Iron spin state in silicate glass at high pressure: implications for melts in the Earth's lower mantle. *Submitted to Earth and Planetary Science Letters*.

The samples were synthesized by C. Weigel (CW) and R. Sinmyo (RS). The conventional Mössbauer spectra were collected by CW, CM and O. Narygina (ON). The synchrotron Mössbauer spectra were collected by CP, CM, LD, VP, I. Kuppenko (IK) and A. Chumakov (AV). All spectra were analyzed by CP. Interpretation of results was carried out by CP, CM and LD. The manuscript was written by CP and CM with help from other co-authors.

[4] Prescher, C., Langenhorst, F., Dubrovinsky, L., Prakapenka, V.B. The effect of Fe spin crossovers on its partitioning behavior and oxidation state in a pyrolitic Earth's lower mantle system. For submission to *Science*.

The starting materials were synthesized by CP. Diamond anvil cell experiments were carried out by CP, LD and V.B. Prakapenka (VBP). CP performed the focused ion beam preparation of the samples

Chapter 1 Introduction

and the TEM analysis. Interpretation of the results and writing of the manuscript was done by CP, FL and LD.

[5] Prescher, C., Dubrovinsky, L., McCammon, C., Glazyrin, K., Nakajima, Y., Kantor, A., Merlini, M., Hanfland, M., 2012. Structurally hidden magnetic transitions in Fe₃C at high pressures. Physical Review B Rapid Communications (2012) 85, 6–9.

The samples were synthesized by CP and Y. Nakajima (YN). The Mössbauer measurements and analysis were performed by CP with the help of LD and CM. The single-crystal x-ray diffraction (SXR) measurements were carried out by CP, LD, K. Glazyrin (KG), A. Kantor (AK), M. Merlini (MM) and M. Hanfland (MH). The SXR data analysis was done by CP and LD. The interpretation of the results and writing of the manuscript was done by CP, LD and CM.

2 MossA – a program for analyzing energy-domain Mössbauer spectra from conventional and synchrotron sources

by C. Prescher^{1*}, C. McCammon¹ and L. Dubrovinsky¹

¹*Bayerisches Geoinstitut, Universität Bayreuth, Bayreuth, 95440, Germany*

*Corresponding author. Email: clemens.prescher@gmail.com

Journal of Applied Crystallography (2012) 45, 329-331

2.1 Abstract

The program MossA provides a straightforward approach to the fitting of ⁵⁷Fe conventional and synchrotron energy-domain Mössbauer spectra. Sites can be defined simply by mouse clicks and hyperfine parameters can be constrained to constant values, within specific ranges, and be coupled linearly between different subspectra. The program includes a full transmission integral fit with Lorentzian line shape (conventional source) or Lorentzian-squared line shape (synchrotron source). The fitting process is graphically displayed in real time while fitting and can be interrupted at any time. Gaussian-shaped quadrupole splitting distributions for analyzing non-magnetic amorphous materials is included. MossA is designed especially for the rapid and comprehensive analysis of complex Mössbauer spectra due to its native graphical user input.

2.2 Introduction

Mössbauer spectroscopy is a unique tool for sampling spin states, oxidation states, and coordination of specific elements. Particularly in the Earth sciences it is frequently used due to the ease of obtaining structural information and the oxidation state of iron in rocks and minerals. The Mössbauer milliprobe technique (McCammon, 1994) has enabled an evaluation of the spin and oxidation state of iron in materials relevant to the Earth's interior up to pressures of the Earth's core (e. g. McCammon et al., 2008). However, detailed analysis of compounds with different iron environments or a mixture of different phases containing iron can be challenging due to the ambiguity of possible fitting models. The outcome of the fitting procedure can depend strongly on the input of the initial parameters of the distribution of sites. Therefore complex spectra need to be evaluated visually before fitting in order to define the initial parameters, and the progress of the fit should ideally be tracked while fitting in order to allow intervention if the solution becomes physically improbable. However, most recently described Mössbauer analysis programs (e.g., Große, 1993; Brand, 1995; Azevedo et al., 1997; Kent, 1998; Lagarec

Chapter 2 MossA

and Rancourt, 1998; Žák and Jirásková, 2006; Hjøllum and Madsen, 2009) are based on a text based input of initial parameters, which makes fitting of complex spectra challenging or even impossible. Additionally the commonly used Gauss-Newton and Levenberg-Marquardt least squares methods do not search for the global minimum, but only for local minima which may be biased by the choice of initial parameters in the fitting model.

We present the Matlab based Mössbauer fitting program “MossA” which overcomes these usual difficulties in the analysis of complicated spectra. Through its clear graphical user interface (GUI) and straightforward procedures for handling data and exporting parameters and fitted spectra, it is easy to analyze complex Mössbauer spectra even for users that are new to Mössbauer spectroscopy.

2.3 Theory

The experimental Mössbauer spectrum is described by the transmission integral, which is essentially a sum of the non-resonant background and a convolution of the source emission line $N(E, \nu)$ and the absorber response $\exp(-t \sigma(E))$:

$$C(\nu) = N_0 e^{-\mu_0 t'} \left[(1 - f_s) + \int_{-\infty}^{+\infty} N(E, \nu) \exp(-t \sigma(E)) dE \right],$$

where N_0 is the number of quanta emitted by the source, μ_0 is the mass absorption coefficient, t' is the absorber thickness and t is the effective absorber thickness. The source line $N(E, \nu)$ and the resonant cross section $\sigma(E)$ are defined by a Lorentzian curve as given by the Breit-Wigner Equation:

$$I(E) = \frac{\Gamma/(2\pi)}{(E - E_0)^2 + (\Gamma/2)^2},$$

where Γ is the full width at half maximum (FWHM) and E_0 is the center of the distribution.

For thin absorbers with $t \ll 1$, the transmission integral can be expanded in a series. Using the first two terms of the expansion yields:

$$C(\nu) = N_0 e^{-\mu_0 t'} \left(1 - f_s \frac{t}{2} \frac{\Gamma^2}{\left[E_0 \left(\frac{\nu}{c} \right) - \Delta E \right]^2 + \Gamma^2} \right),$$

Chapter 2 MossA

which is a linear combination of two Lorentzian line shapes, which can be described by a Lorentzian line with the FWHM being a sum of the source and the absorber FWHM. This thin absorber approximation is frequently used in Mössbauer spectroscopic analysis because of the ease in computation.

New advances in Mössbauer synchrotron technology have made it possible to obtain Mössbauer spectra in the energy domain with the aid of nuclear Bragg reflection, the so-called synchrotron Mössbauer source (Smirnov et al., 1997). This process leads to a slightly different source line shape, however, which due to the physics of the process is a normalized squared Lorentzian (Smirnov et al., 1997):

$$I(E) = \pi\Gamma \left\{ \frac{\Gamma/(2\pi)}{(E - E_0)^2 + (\Gamma/2)^2} \right\}^2.$$

Synchrotron Mössbauer experiments in the energy domain are characterized by very high absorption (typically on the order of 50%) and by the lack of non-resonant background. The high absorption makes it absolutely necessary to use the transmission integral; however most of the current software packages for analyzing Mössbauer spectra lack the possibility for fitting these spectra. With MossA it is possible to fit data using the full transmission integral with either source line shape. A further characteristic of the synchrotron Mössbauer source is that radiation is linearly polarized. In the case of powder samples with random crystallite orientation, Mössbauer spectra are unchanged from those collected with an unpolarized source. However in the case of single crystals or powder samples with preferred orientation, the component area ratios of quadrupole doublets and of magnetic sextets will change. This effect can be accounted for by allowing component area ratios to vary, which is implemented in MossA.

2.4 Program features

MossA is based on the Matlab programming language, and uses its native GUI library and the Optimization Toolbox. MossA is capable of fitting Lorentzian, Gaussian, PseudoVoigt, and Lorentzian-squared absorber line shapes. The available subspectra are singlets, doublets, and sextets. These subspectra are defined visually by two mouse clicks for singlets and three mouse clicks for doublets and sextets. In order to more precisely define specific parameters, values can be edited after adding the subspectrum. The parameters (center shift, FWHM, quadrupole splitting, magnetic hyperfine splitting) can be kept constant or can be constrained to fall within specific ranges in their search space during fitting. This can be useful when fitting overlapping subspectra, for example, to constrain a subspectrum to have a specific center shift range. Spectra of samples with preferential orientation or single crystals

Chapter 2 MossA

can be treated empirically by fitting the component area ratios of doublets or sextets. Furthermore, it is possible to linearly couple two parameters (including component area ratios) from the same or different subspectra. One application of this feature is when information about site occupancy from crystallography or crystal chemistry is available, which constrains the abundance relationships between the different sites of a phase. If the Lamb-Mössbauer factor can be assumed to be the same for all of the sites, the fit can be constrained to fix the area ratios between different subspectra according to a specific factor inferred from crystallography.

The analysis of Mössbauer spectra measured from amorphous samples can be challenging, even in the absence of magnetic hyperfine splitting. Due to the different environments of the Mössbauer active isotope, there is a significant line broadening and there can be a coupling of center shift and quadrupole splitting. One mathematical model for this coupling was introduced by Rancourt & Ping (1991) as a quadrupole splitting distribution (QSD). An interface for fitting such distributions is included in the program MossA. Sites with QSD can be combined with normal sites in a fit and also used in combination with the full transmission integral.

The trust-region reflective method of the Matlab optimization toolbox is used as minimization algorithm. This method is more stable than the commonly used finite difference least squares procedure

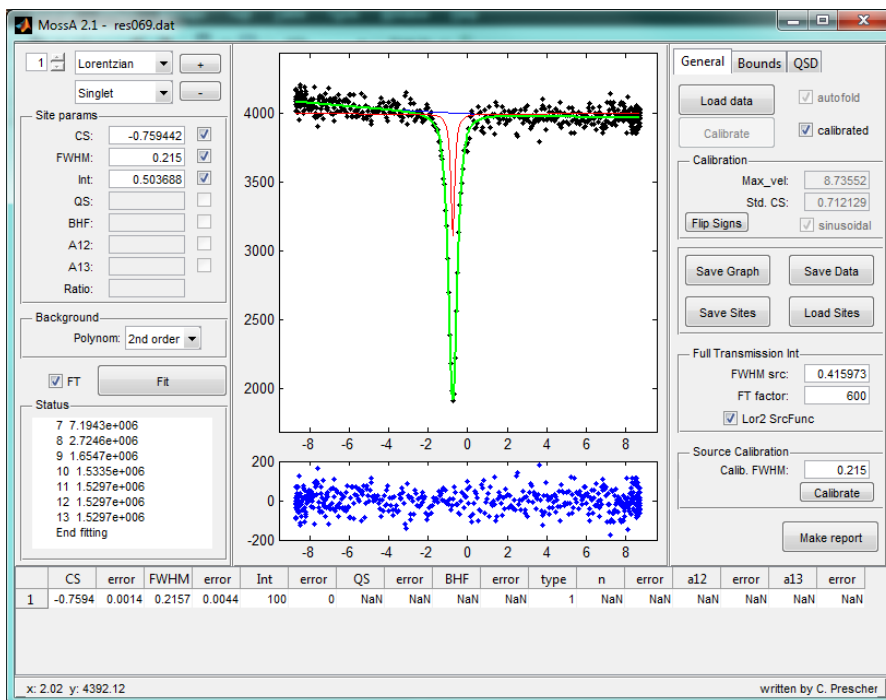


Figure 2-1 Calibration of the FWHM of a Lorentzian-squared source line. A second-order polynomial is automatically calculated to account for curvature in the baseline.

Chapter 2 MossA

since it is more likely to detect global minima. The progress and direction of the fitting can be seen in the graphics window during the fitting process. If the fitting approaches a local minimum which is physically improbable, the user has the possibility to stop the fitting process at any time.

The program is especially suited for analyzing synchrotron Mössbauer source data. The program features include a sinusoidal baseline, a squared Lorentzian source function for the full transmission integral and one mouse click calibration of the FWHM of the source function.

The fitted parameters can be either copied directly to a spreadsheet or saved as plain text file. Graphical output formats include *.fig (Matlab editable plot file) or any other common picture format. For distributing and discussing with colleagues, the report option is most suitable as it presents the graphical data and fitted parameters in a PDF file.

2.5 Example workflow

The first step for sample analysis is to calibrate the velocity scale of the transducer by analyzing an α -Fe calibration spectrum. MossA has a tool to obtain the best fit values for the relative shift and the maximum of the velocity scale. After calibration, the values are saved in program memory. The next step

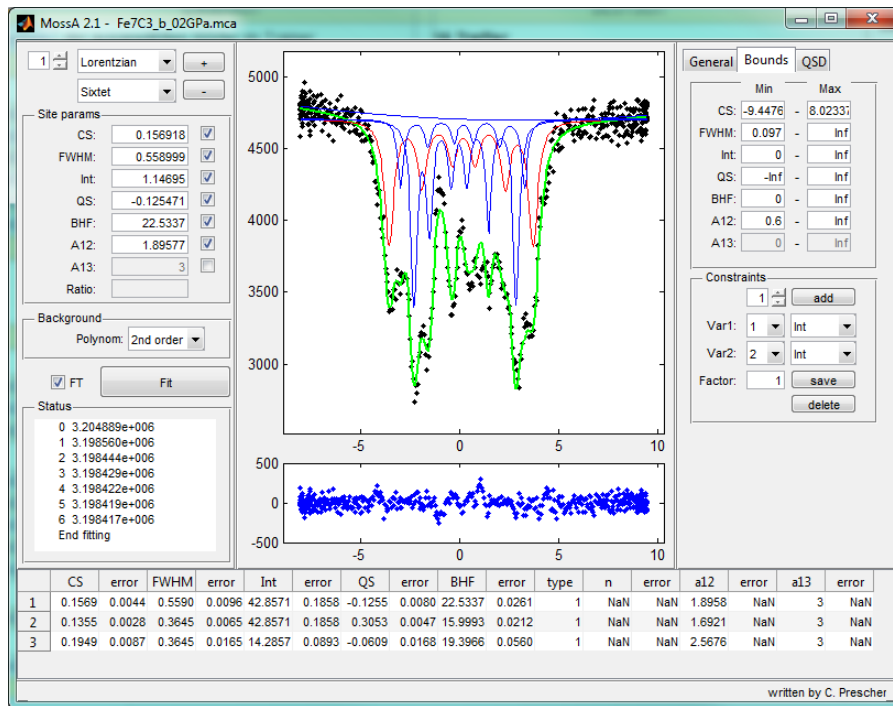


Figure 2-2 User interface during the fitting process. The example spectrum shown is for a full transmission integral fit to Fe_7C_3 with three sextets, each with the component area ratio A_{13} fixed to 3 and the intensities of the first and second sextets constrained to be equal as required by crystallographic constraints.

Chapter 2 MossA

is to estimate the FWHM of the source function by calibrating a single line absorber (Fig. 2-1). Next the data file is loaded and the possible sites are defined by clicking the mouse at appropriate places in the graphics window (Fig. 2-2). If the initial estimates are satisfactory, the fitting process can be started. The progress of the fit is shown in the graphics window, where the chi-squared value is displayed as a measure of the goodness of fit. Depending on the outcome of the fitting, additional sites can be added, the background model can be changed, and parameters can be constrained or coupled. When the fitting process is completed satisfactorily, all parameters can be copied and pasted into a spreadsheet and the fit can be saved as numerical values for plotting with the user's preferred plot software or directly output in one of the common picture formats from the MossA program.

2.6 Distribution

The program MossA and its documentation can be obtained at <http://www.clemensprescher.com/> under Programs -> MossA after a registration. For running the program it is not necessary to have a Matlab license; only the Matlab runtime component is needed, which will be delivered with the program executable. MossA runs under Windows, MacOS X and Linux.

2.7 Acknowledgements

The authors thank V. Potapkin, A. Kantor, I. Kantor and I. Sergueev for testing the program, reporting bugs and giving useful hints for further improvement.

3 Effect of iron oxidation state on the electrical conductivity of the Earth's lower mantle

by V. Potapkin^{1,2}, C. McCammon^{2*}, K. Glazyrin², A. Kantor^{1,2}, I. Kuppenko², C. Prescher², R. Sinmyo², G.V. Smirnov³, A.I. Chumakov^{1,3}, R. Rüffer¹ and L. Dubrovinsky²

¹European Synchrotron Radiation Facility, BP 220, F-38043 Grenoble, France

²Bayerisches Geoinstitut, Universität Bayreuth, D-95440 Bayreuth, Germany

³National Research Center "Kurchatov Institute", 123182 Moscow, Russia

*Corresponding author. E-mail: catherine.mccammon@uni-bayreuth.de

Submitted to Nature Communications

3.1 Abstract

Iron has the ability to adopt different electronic configurations, namely spin states, in the dominant lower mantle phase, magnesium silicate perovskite, where the spin states of iron atoms can significantly influence mantle properties and dynamics. Previous studies have indicated that ferric iron (which constitutes at least half of the iron in lower mantle silicate perovskite (McCammon, 1997; Frost et al., 2004; Mccammon, 2005)) undergoes a high-spin to low-spin transition (Zhang and Oganov, 2006; Stackhouse et al., 2007; Catalli et al., 2010, 2011; Hsu et al., 2011), which has been suggested to cause seismic velocity anomalies (Catalli et al., 2011; Hsu et al., 2011) and a drop in laboratory-measured electrical conductivity (Ohta et al., 2008; Ohta, Hirose, Ichiki, et al., 2010; Ohta, Hirose, Shimizu, et al., 2010). Here we apply a new synchrotron-based method of Mössbauer spectroscopy to four different compositions of lower mantle silicate perovskite at high pressure and high temperature and demonstrate unambiguously that Fe³⁺ remains in the high-spin state at conditions throughout the lower mantle. New high-pressure high-temperature electrical conductivity measurements show no conductivity drop for magnesium silicate perovskite with high Fe³⁺, strongly advocating that the conductivity drop observed for magnesium silicate perovskite with high Fe²⁺ (Ohta et al., 2008; Ohta, Hirose, Ichiki, et al., 2010; Ohta, Hirose, Shimizu, et al., 2010) is due to a transition of Fe²⁺ to the intermediate spin state. Correlation of transport and elastic properties of silicate perovskite with electromagnetic and seismic data provide a new probe of heterogeneity in the lower mantle.

3.2 Manuscript

The structure of iron-containing magnesium aluminium silicate perovskite (hereafter referred to as FeAlPv) contains two sites, a large 8-12 coordinated site ("A") which is primarily occupied by Mg²⁺ and

Chapter 3 Effect of iron spin state on the electrical conductivity of the Earth's lower mantle

Fe^{2+} , and a smaller octahedral site ("B") which is dominantly occupied by Si^{4+} . Most studies observe a transition involving Fe^{2+} that starts above ~ 30 GPa, although there is disagreement as to whether it involves a high-spin (HS) (four unpaired d electrons) to intermediate-spin (IS) (two unpaired d electrons) transition (Badro et al., 2004; Lin et al., 2008; McCammon et al., 2008) or simply a structural modification of the local atomic environment (Hsu et al., 2010). With respect to Fe^{3+} , broadly a high-spin (five unpaired d electrons) to low-spin (LS) (one unpaired d electron) transition is predicted when Fe^{3+} occupies the B-site, while Fe^{3+}_A (i.e., Fe^{3+} in the A-site) is predicted to remain in the high-spin state at all pressures throughout the lower mantle (Zhang and Oganov, 2006; Stackhouse et al., 2007; Catalli et al., 2010, 2011; Hsu et al., 2011; Fujino et al., 2012). Even though Fe^{3+} is predicted to occupy exclusively the A-site in lower mantle compositions of FeAlPv (Vanpeteghem et al., 2006), a HS-LS transition of Fe^{3+} was reported to occur in FeAlPv at high pressure, potentially due to exchange of Fe^{3+} from the A- to the B-site (Catalli et al., 2010, 2011; Fujino et al., 2012). Up to now, however, only methods which do not provide an unambiguous interpretation of the data have been used, so we have developed a new method which enables individual spin and valence states to be identified, which provides a clear answer to the question of whether Fe^{3+} undergoes a HS-LS transition in FeAlPv.

Detecting spin transitions of Fe^{3+} in FeAlPv presents a significant challenge. X-ray emission spectroscopy provides information on the bulk spin number, but cannot separate individual contributions. In contrast energy domain ^{57}Fe Mössbauer spectroscopy generally enables an unambiguous resolution of all hyperfine parameters which can be used to infer spin states; however high pressure measurements using conventional radioactive point sources require extremely long counting times (generally more than one week per spectrum). Third generation synchrotron sources offer a solution in the form of time-domain Mössbauer spectroscopy (i.e., nuclear forward scattering); however this method is not well suited to materials with a large number of components (such as FeAlPv) due to the resulting complex spectra. To solve this problem we have developed an energy-domain synchrotron Mössbauer source (SMS) that offers a number of advantages over conventional Mössbauer spectroscopy: high brilliance and a nearly fully resonant emitted beam that can be focused to a spot of only a few microns diameter, and in contrast to time domain spectroscopy, spectra that deliver direct and unambiguous information. Therefore SMS allows for rapid measurement of energy-domain Mössbauer spectra under extreme conditions with a quality generally sufficient to unambiguously deconvolute even highly complex spectra (further details of the method are given in the Supplementary Information).

Chapter 3 Effect of iron spin state on the electrical conductivity of the Earth's lower mantle

In order to investigate the spin state of iron in lower mantle silicate perovskite, we studied four different silicate perovskite samples: $\text{Mg}_{0.6}\text{Fe}_{0.4}\text{Si}_{0.63}\text{Al}_{0.37}\text{O}_3$ sample #1 ($\sim 80\% \text{Fe}^{3+}/\Sigma\text{Fe}$); $\text{Mg}_{0.6}\text{Fe}_{0.4}\text{Si}_{0.63}\text{Al}_{0.37}\text{O}_3$ sample #2 ($\sim 70\% \text{Fe}^{3+}/\Sigma\text{Fe}$); $\text{Mg}_{0.78}\text{Fe}_{0.2}\text{Al}_{0.05}\text{Si}_{0.97}\text{O}_3$ ($\sim 50\% \text{Fe}^{3+}/\Sigma\text{Fe}$) (sample #3); $\text{Mg}_{0.94}\text{Fe}_{0.06}\text{SiO}_3$ ($\sim 20\% \text{Fe}^{3+}/\Sigma\text{Fe}$) (sample #4). We collected SMS spectra at room temperature and pressures up to 122 GPa using diamond anvil cells, with or without laser annealing of the samples. Details of sample synthesis and experiment methodology are given in the Supplementary Information.

SMS spectra of $\text{Mg}_{0.6}\text{Fe}_{0.4}\text{Si}_{0.63}\text{Al}_{0.37}\text{O}_3$ perovskite (sample #1), which contains iron dominantly as Fe^{3+} , are extremely well resolved (Fig. 3-1). We fit the data to three quadrupole doublets, one assigned to Fe^{3+} and two assigned to Fe^{2+} based on their centre shifts. Visually there appears to be no change to

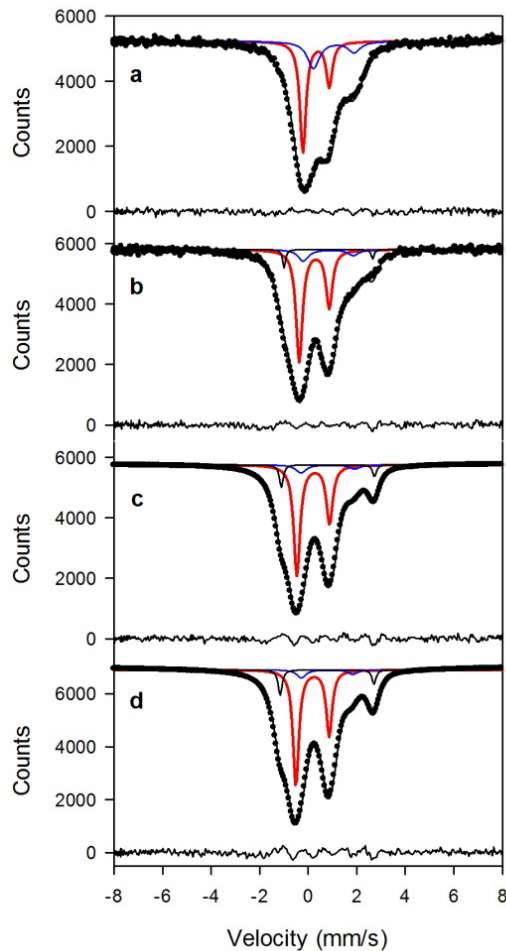


Figure 3-1 SMS spectra of $\text{Mg}_{0.6}\text{Fe}_{0.4}\text{Si}_{0.63}\text{Al}_{0.37}\text{O}_3$ perovskite sample #1 at room temperature showing their evolution with pressure (a) 2.5 GPa; (b) 37.9 GPa; (c) 67 GPa; (d) 93 GPa. The data were fit to one Fe^{3+} doublet (red) and two Fe^{2+} doublets (blue and black), and the fit residual is shown below each spectrum. Area asymmetry is due to preferred orientation of the sample, and the velocity scale is given relative to α -iron.

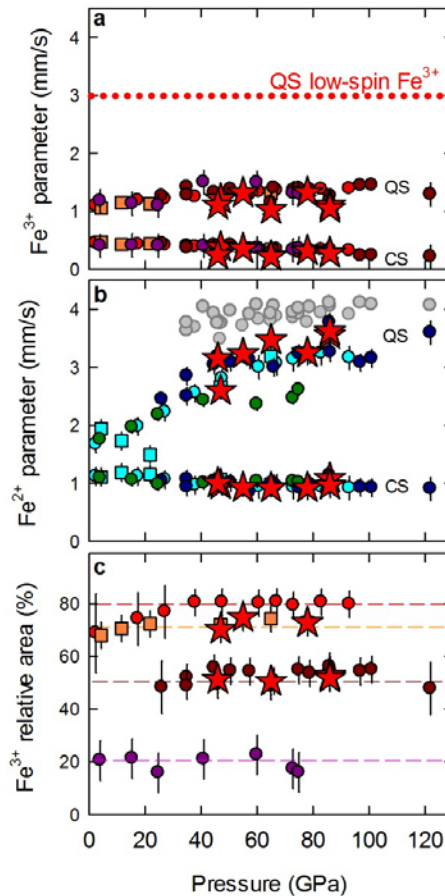


Figure 3-2 Pressure variation of FeAlPv hyperfine parameters (centre shift [CS] and quadrupole splitting [QS]) (a) high-spin Fe^{3+} ; (b) Fe^{2+} . Sample data are indicated as follows: $\text{Mg}_{0.6}\text{Fe}_{0.4}\text{Si}_{0.63}\text{Al}_{0.37}\text{O}_3$ perovskite sample #1 (red and blue circles); $\text{Mg}_{0.6}\text{Fe}_{0.4}\text{Si}_{0.63}\text{Al}_{0.37}\text{O}_3$ perovskite sample #2 (orange and blue squares); $\text{Mg}_{0.78}\text{Fe}_{0.2}\text{Al}_{0.05}\text{Si}_{0.97}\text{O}_3$ perovskite sample #3 (brown and dark blue circles); $\text{Mg}_{0.94}\text{Fe}_{0.06}\text{SiO}_3$ perovskite sample #4 (purple and green circles). The expected quadrupole splitting for low-spin Fe^{3+} is shown as a horizontal red dotted line. Hyperfine parameters for Fe^{2+} are shown as weighted averages of the two doublets (colours as above) and quadrupole splitting for the high QS Fe^{2+} doublet (grey circles) (c) Pressure variation of $\text{Fe}^{3+}/\Sigma\text{Fe}$ as determined from the relative areas in silicate perovskite Mössbauer spectra: sample #1 (red circles); sample #2 (orange squares); sample #3 (brown circles); sample #4 (purple circles). Horizontal lines are guides for the eye. Values obtained after laser heating of samples #2 and #3 are indicated by red stars. Error bars represent 2σ uncertainty based on fitting statistics. In all cases, parameters remained unchanged from those before heating within experimental error, demonstrating that there is no high-spin to low-spin transition in Fe^{3+} at the pressure-temperature conditions of the lower mantle.

the Fe^{3+} doublet over the entire pressure range (Fig. 3-1 and Supplementary Fig. 3-S4).

The hyperfine parameters (centre shift [CS] and quadrupole splitting [QS]) for Fe^{3+} in all samples are the same within experimental error, and there is no change in $\text{Fe}^{3+}/\Sigma\text{Fe}$ for individual samples over

Chapter 3 Effect of iron spin state on the electrical conductivity of the Earth's lower mantle

the entire pressure range of the experiment (Fig. 3-2). The hyperfine parameters of the Fe^{3+} doublet are consistent with the high-spin state (Greenwood and Gibb, 1971), and their smooth variation with pressure indicates that Fe^{3+} does not undergo any spin transitions within the entire pressure range. Notably the QS value proposed for low-spin Fe^{3+} from both experimental (Catalli et al., 2010, 2011) and theoretical (Hsu et al., 2011) studies (red dashed line, Fig. 3-2a) is more than twice our observed values.

The weighted mean quadrupole splitting for Fe^{2+} in all samples increases dramatically with pressure (Fig. 3-2b), which arises from a decreasing intensity of the low QS Fe^{2+} doublet (blue doublet in Fig. 3-1) corresponding to the HS state (McCammon et al., 2008), and an increasing intensity of the high QS doublet (black doublet in Fig. 3-1) which we assign to the IS state (Lin et al., 2008; McCammon et al., 2008).

Single-crystal X-ray refinements (Glazyrin et al., *subm.*) and crystal chemical calculations (see Supplementary Information) have shown that Fe^{3+} occupies only the A-site of the perovskite structure in our samples; hence our data demonstrate that Fe^{3+}_A does not undergo a high-spin to low-spin transition up to at least 122 GPa. This conclusion is in agreement with results from experimental (Catalli et al., 2010, 2011) and theoretical (Zhang and Oganov, 2006; Stackhouse et al., 2007; Hsu et al., 2011) studies. However several publications (Catalli et al., 2010, 2011; Fujino et al., 2012) have suggested that the reduced volume of LS Fe^{3+}_B could lead to a redistribution of Fe^{3+} from the A- to the B-site in the perovskite structure within the lower mantle. To test this hypothesis, we laser annealed samples #2 and #3 at a number of pressures and collected SMS spectra both during and after heating. The total duration of heating reached several hours after multiple cycles. Visually SMS spectra collected after laser annealing showed no change to those taken before heating (Supplementary Fig. 3-S5) and hyperfine parameters remain unchanged (star symbols; Fig. 3-2). We therefore conclude that there is no exchange of Fe^{3+} between the A- and the B-site at lower mantle pressures and temperatures, in agreement with the results of a complementary study using high-pressure single-crystal X-ray diffraction with laser heating undertaken on the same composition as two of our samples (Glazyrin et al., *subm.*).

Electromagnetic induction data offer an important complement to seismic data with respect to lower mantle modeling, since the former are more sensitive to temperature and iron content, while the latter better constrain the mineralogy (Verhoeven et al., 2009). Laboratory electrical conductivity data of the relevant minerals are an important component of the approach, since they provide critical data on how the chemical and thermal state of the material influences the conductivity. Laboratory measurements of single-phase $\text{Mg}_{0.9}\text{Fe}_{0.1}\text{SiO}_3$ perovskite (Ohta et al., 2008; Ohta, Hirose, Shimizu, et al.,

Chapter 3 Effect of iron spin state on the electrical conductivity of the Earth's lower mantle

2010) and a pyrolite mantle assemblage (Ohta, Hirose, Ichiki, et al., 2010) ($\text{Fe}^{3+}/\Sigma\text{Fe}$ of the perovskite phase estimated to be 12% and 30%, respectively (McCammon et al., 2004)) show a decrease in conductivity above 50 GPa, comparable to the electrical conductivity decrease caused by HS-LS spin crossover of Fe^{2+} in (Mg,Fe)O (Lin, Weir, et al., 2007; Ohta et al., 2007; Yoshino et al., 2011). The drop in silicate perovskite conductivity has been attributed to a HS-LS transition of Fe^{3+} (Ohta et al., 2008; Ohta, Hirose, Ichiki, et al., 2010; Ohta, Hirose, Shimizu, et al., 2010); however this explanation is ruled out by the results in the present work. To investigate the relative contributions of Fe^{2+} and Fe^{3+} , we measured the electrical conductivity of $\text{Mg}_{0.6}\text{Fe}_{0.4}\text{Si}_{0.63}\text{Al}_{0.37}\text{O}_3$ perovskite (93% $\text{Fe}^{3+}/\Sigma\text{Fe}$) (Glazyrin et al., *subm.*) at high pressure and high temperature (details are given in Supplementary Information). In contrast to the large drop seen in samples dominated by Fe^{2+} , there is a continuous increase in electrical conductivity with pressure (Fig. 3-3). Such behaviour strongly suggests that the conductivity drop in samples dominated by Fe^{2+} is due to the HS to IS transition in Fe^{2+} , where electron mobility is reduced due to the spin transition, analogous to the behaviour of (Mg,Fe)O (Lin, Weir, et al., 2007; Ohta et al., 2007; Yoshino et al., 2011). The greater drop at high temperature (brown circles in Fig. 3-3) is consistent with the increasing stability of the IS state with temperature (Lin et al., 2008; McCammon et al., 2008). Previously temperature and total iron content have been considered to have the greatest influence on lower

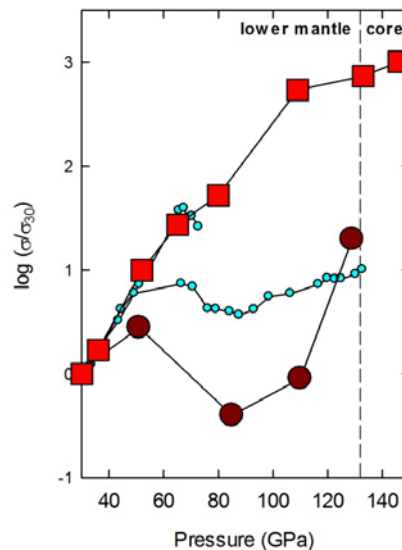


Figure 3-3 Relative change of electrical conductivity of FeAlPv as a function of pressure. Red squares indicate new data for $\text{Mg}_{0.6}\text{Fe}_{0.4}\text{Si}_{0.63}\text{Al}_{0.37}\text{O}_3$ perovskite ($\text{Fe}^{3+}/\Sigma\text{Fe} \sim 93\%$) collected at 1800 K. Also shown are two sets of literature data for $\text{Mg}_{0.9}\text{Fe}_{0.1}\text{SiO}_3$ perovskite ($\text{Fe}^{3+}/\Sigma\text{Fe} \sim 12\%$) at room temperature (blue circles) (Ohta, Hirose, Shimizu, et al., 2010) and a pyrolite assemblage ($\text{Fe}_{\text{pv}}^{3+}/\Sigma\text{Fe}_{\text{pv}} \sim 30\%$) (McCammon et al., 2004) at 1800 K (brown circles) (Ohta, Hirose, Ichiki, et al., 2010). Data are plotted relative to the values at 30 GPa (σ_{30}).

Chapter 3 Effect of iron spin state on the electrical conductivity of the Earth's lower mantle

mantle electrical conductivity profiles (Verhoeven et al., 2009), but our data show that $\text{Fe}^{3+}/\Sigma\text{Fe}$ will also affect conductivity significantly at mid-mantle depths (1200-1900 km). A companion work has shown that $\text{Fe}^{3+}/\Sigma\text{Fe}$ will also affect bulk sound velocity in the lower mantle (Glazyrin et al., *subm.*); hence joint inversion of electromagnetic and seismic data based on these new data will likely yield different results. For example the superadiabatic temperature gradient inferred for the lower mantle from such a joint inversion (Verhoeven et al., 2009) may not be required due to the reduced electrical conductivity of silicate perovskite resulting from the HS-IS transition. Three-dimensional inversions of electromagnetic data are now possible, and show variations of more than one order of magnitude, many of which are correlated with fast and slow regions of seismic tomography models (Tarits and Mandéa, 2010). Our new data indicate that for silicate perovskite with lower mantle composition, a lower $\text{Fe}^{3+}/\Sigma\text{Fe}$ ratio will cause lower conductivity (reduction of conductivity due to the Fe^{2+} HS-IS transition) and a higher bulk sound velocity (Glazyrin et al., *subm.*). Indeed many regions were found to show such a correlation (Tarits and Mandéa, 2010), which could be indicative of bulk mantle properties away from areas associated with subduction.

In conclusion, based on novel SMS data we have clarified the hotly debated electronic behaviour of iron in silicate perovskite, in particular its effect on electrical conductivity. Our results provide improved constraints for forward modelling of electromagnetic data as well as for joint inversion of electromagnetic and seismic data, providing a new probe of heterogeneity in the lower mantle.

3.3 Methods

^{57}Fe Synchrotron Mössbauer source (SMS) spectra were collected on the Nuclear Resonance beamline ID18 at the European Synchrotron Radiation Facility (ESRF) during operation in multibunch mode (7/8+1 filling) with the beam focused to roughly $10\times 10\ \mu\text{m}^2$ using Kirkpatrick–Baez multilayer optics. Further details of the SMS method are given in the literature (Potapkin et al., 2012) and in the Supplementary Information. The velocity scale was calibrated relative to α -Fe foil, and spectra were collected over 10-60 min each. Spectra were fitted using the program MossA (Prescher et al., 2012), which takes into account the Lorentzian-squared source instrumental function (Smirnov et al., 2011). The dimensionless effective Mössbauer thicknesses were approximately 40 and 20 for the $\text{Mg}_{0.6}\text{Fe}_{0.4}\text{Si}_{0.63}\text{Al}_{0.37}\text{O}_3$ perovskite samples #1 and #2, and 8 and 3 for the $\text{Mg}_{0.78}\text{Fe}_{0.2}\text{Al}_{0.05}\text{Si}_{0.97}\text{O}_3$ and $\text{Mg}_{0.94}\text{Fe}_{0.06}\text{SiO}_3$ perovskite samples, respectively. Electrical conductivity measurements were carried out at high pressure and high temperature according to a previously described method (Kuznetsov, 2007).

Chapter 3 Effect of iron spin state on the electrical conductivity of the Earth's lower mantle

Further details of sample synthesis and experimental methodology are given in the Supplementary Information.

3.4 Supplementary information

3.4.1 Synchrotron Mössbauer source

Energy-domain Mössbauer spectroscopy provides direct access to hyperfine parameters from which iron valence and spin state can be determined. It has a large advantage compared to nuclear forward scattering (NFS) and X-ray emission spectroscopy (XES) in that the contribution from each iron subsystem occupies a nearly unique energy range which generally enables an unambiguous resolution of all hyperfine components. This advantage of Mössbauer spectroscopy makes it an ideal tool to study systems where iron exists in different spin and valence states, and different crystallographic positions.

Conventional energy-domain Mössbauer spectroscopy uses radioactive sources whose brilliance is very low; hence high-pressure studies using diamond anvil cells (DACs) require long measuring times since beam focusing is not possible. This reduces the quality of the results due to pressure gradients, increased background, and restricts the maximum pressure at which measurements are possible. These problems can be solved by combining the advantages of high-brilliance third generation synchrotrons (high flux, extreme focusing of the beam) with the resolution of energy-domain Mössbauer spectroscopy to produce a synchrotron source of Mössbauer radiation.

A synchrotron Mössbauer source (SMS) provides a high-brilliance beam of synchrotron radiation with an energy bandwidth of ~ 20 neV. In addition, SMS has several further properties that a radioactive source does not possess. The SMS beam is polarized up to 99%, and it consists 100% of recoilless radiation with zero background. These properties enable rapid and precise measurements of Mössbauer spectra of samples under extreme conditions.

The possibility to develop such a source was first demonstrated at the Nuclear Resonance beamline ID18 (Rüffer and Chumakov, 1996) at the European Synchrotron Radiation Facility (ESRF) in 1997 (Smirnov et al., 1997). Technical details of the configuration used in the present work are given in Potapkin et al. (2012).

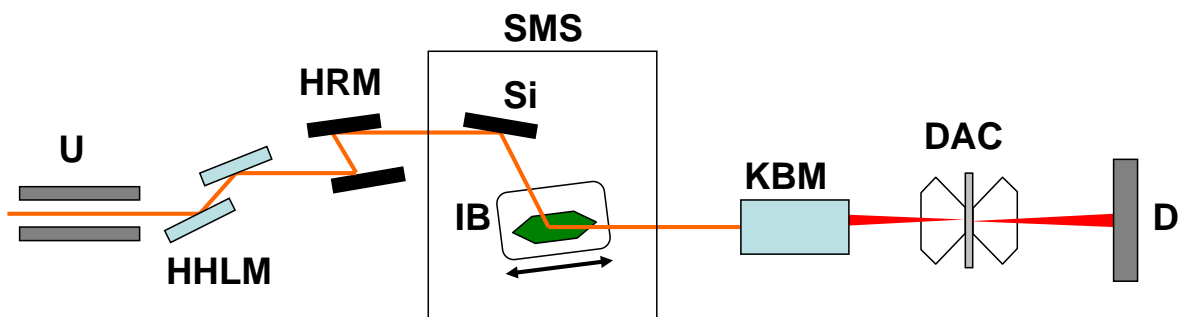


Figure 3-S1 Optical scheme for SMS experiment for high-pressure studies. U - undulator; HHLM – high-heat load monochromator; HRM – high resolution monochromator; SMS: Si – Si (311) crystal; IB – enclosed furnace (mounted on a velocity transducer) with the iron borate crystal inside; KBM - Kirkpatrick-Baez mirrors; DAC – diamond anvil cell; D – avalanche photo diode detector.

Fig. 3-S1 shows the experimental setup. The synchrotron beam passes through the undulator (U), a high-heat load monochromator (HHLM) with energy bandwidth of ~ 2 eV, and a high resolution monochromator (HRM) with energy bandwidth of ~ 15 meV. This cascade of monochromators is required to decrease the heat load on the iron borate crystal in order to prevent a temperature gradient. The SMS itself is a monochromator composed of two crystals. The key element of the source is a highly perfect iron borate crystal (FeBO_3) enriched in the ^{57}Fe isotope. The crystal is used in (333) pure nuclear reflection. For such reflection, electronic diffraction is forbidden, while nuclear diffraction is allowed. The crystal is placed in an external magnetic field of ~ 110 Oe and heated close to its Néel temperature of 348.75 K. Under these conditions the hyperfine magnetic structure collapses to a single line. The crystal therefore reflects synchrotron radiation within an energy bandwidth of ~ 20 neV. Further details of the physics of the process are given in (Smirnov et al., 2011). The furnace is enclosed and special arrangements of the magnets are used in order to ensure homogenous heating and magnetic field for stable operation. The furnace with the crystal inside is mounted on a velocity transducer in order to modulate the energy. The purpose of the Si (311) crystal is to direct the beam emitted by the SMS in a direction parallel to the incoming synchrotron beam, which allows for a more convenient installation of different types of sample environment such as DAC, cryostat, furnace, etc. The SMS is followed by a focusing mirror (KBM), which allows focusing of the synchrotron beam to a roughly $10 \times 10 \mu\text{m}^2$ spot size on the sample located in the DAC. The transmitted γ -quanta are monitored by an avalanche photo diode detector.

During the SMS experiment the linewidth of the source is controlled before and after each sample measurement using $\text{K}_2\text{Mg}^{57}\text{Fe}(\text{CN})_6$, whose Mössbauer spectrum consists of a single line (Fig.3-S2). The velocity scale is calibrated using 25 μm thick natural α -iron foil (Fig. 3-S3).

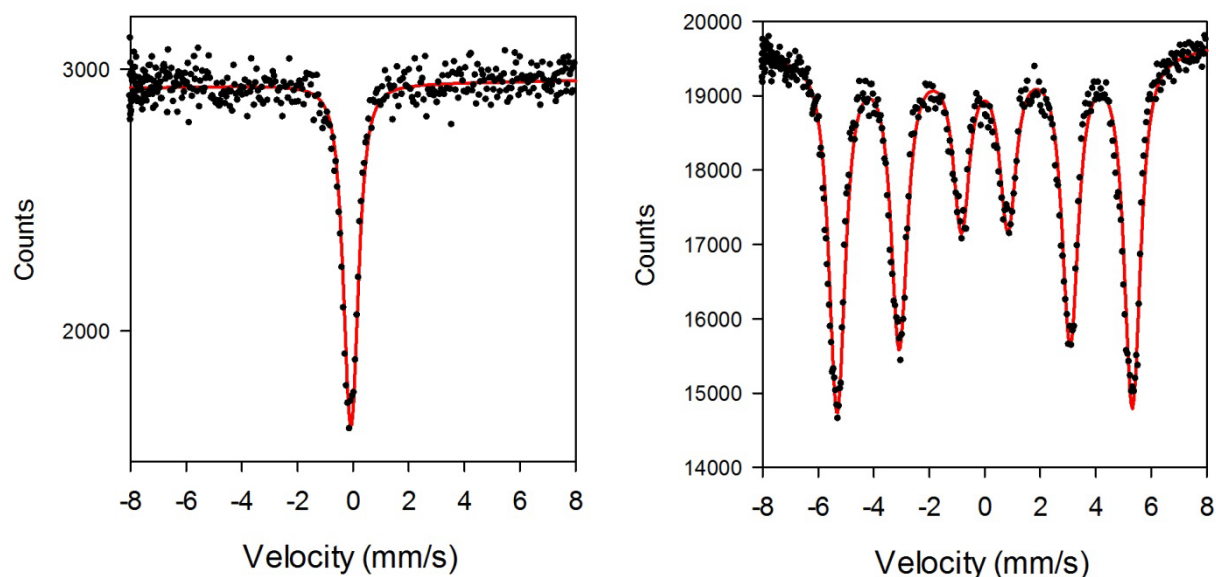


Figure 3-S3 (left) SMS spectrum of $K_2Mg^{57}Fe(CN)_6$ used to monitor the source linewidth.

Figure 3-S2 (right) SMS spectrum of 25 μm thick natural α -iron foil used for energy calibration.

3.4.2 Sample synthesis

All silicate perovskite samples were synthesized using a multianvil press. The experiments were performed using Cr_2O_3 -doped MgO octahedra fitted with a $LaCrO_3$ heater in combination with tungsten carbide cubes following the methodology described in (Keppler and Frost, 2005). Chemical compositions were measured using an electron microprobe (S4850) or a field emission scanning electron microscope (S4949 and S5083). Details of each experiment are given in Table 3-S1.

3.4.3 DAC experiments

Samples for DAC experiments were carefully selected from the run products to be homogeneous under an optical microscope. Small plate-like pieces of the material (typical dimensions $\sim 30 \times 30 \times 15 \mu m^3$) were loaded together with ruby chips (pressure marker) into the sample chambers of DACs available at Bayerisches Geoinstitut. Diamonds with culets of diameter 120, 250, and 300 μm were used in different experiments depending on the pressure range. The sample chamber was prepared by drilling a hole in a pre-indented rhenium gasket, and the hole was filled with the sample material and the quasi-hydrostatic pressure medium, Ne.

Chapter 3 Effect of iron spin state on the electrical conductivity of the Earth's lower mantle

Table 3-S1 Experimental details and sample compositions

Run number	S4850	S4949	S5083
Sample designation	#1, #2	#3	#4
Starting material	Mg(OH) ₂ , SiO ₂ , Al ₂ O ₃ , Fe ₂ O ₃	MgO, SiO ₂ , Al ₂ O ₃ , Fe ₂ O ₃	MgO, SiO ₂ , Fe ₂ O ₃
Pressure (GPa)	25	26	26
Temperature (°C)	1300	1800	1800
Run duration (min)	30	30	50
Capsule	Pt	Re	Re
Run product	Pv, Al-rich hydrous phase, quenched melt	Pv	Pv
Cation proportions (for 3 O)			
Mg	0.60(1)	0.78(2)	0.94(3)
Fe	0.40(1)	0.20(2)	0.06(1)
Al	0.37(1)	0.05(1)	-
Si	0.63(1)	0.98(2)	1.00(2)
Fe ³⁺ /ΣFe	0.80(5) (sample #1) 0.70(5) (sample #2)	0.50(5)	0.20(8)

3.4.4 Laser heating

We used a modified and enhanced version of the portable laser heating setup described previously (Dubrovinsky et al., 2009, 2010b). The setup was installed on beamline ID18 and consists of a SPI laser system (SPI100, wavelength 1064 nm, 100 W) coupled by an optical fibre to a UniHead system, which allows simultaneous visual observation of the sample, laser heating and evaluation of temperature. In order to ensure homogeneous heating of the samples, a laser spot with a diameter of about 50 μm was used. In order to guarantee homogeneous heating we flattened the power profile of the laser beam using a special optical device (π-shaper) mounted on the UniHead.

Samples #2 and #3 were heated for a total of several hours in multiple cycles during continuous laser operation mode. Thermal radiation from the heated sample was collected by an Ocean Optics QE65000 spectrometer, and the resulting spectra were fitted to the Planck radiation function (Bassett and Weathers, 1986), which gave temperatures between 2000 and 2400 K.

3.4.5 SMS spectrum fitting

SMS spectra can be fitted using the same approach for conventional energy domain Mössbauer spectra provided the following criteria are met: (a) the source lineshape is implemented as a normalised squared Lorentzian (instead of a normalised Lorentzian) (Smirnov et al., 2011):

$$I(E) = \pi\Gamma \left\{ \frac{\Gamma/(2\pi)}{(E-E_0)^2 + (\Gamma/2)^2} \right\}^2; \quad (\text{S.1})$$

(b) the full transmission integral is used to fit the data due to the high absorption and the lack of non-resonant background; and (c) component areas of doublets and sextets are not fixed to ideal values (i.e., 1:1 for quadrupole doublets and 3:2:1:1:2:3 for magnetic sextets) due to the polarised nature of the synchrotron source combined with the tendency for preferred orientation in the DAC.

We fit all of the SMS spectra to three quadrupole doublets, one with small centre shift (average value ~ 0.35 mm/s) corresponding to Fe^{3+} , and two with larger centre shift (average value ~ 1 mm/s) corresponding to Fe^{2+} . We applied the conventional constraint of equal widths but allowed the area ratios of component doublets to vary, with all area ratios of doublets within a single spectrum constrained to be the same based on the reasonable assumption that the principal directions of the electric field gradient for both the A and the B sites are the same based on the crystallography of the perovskite structure.

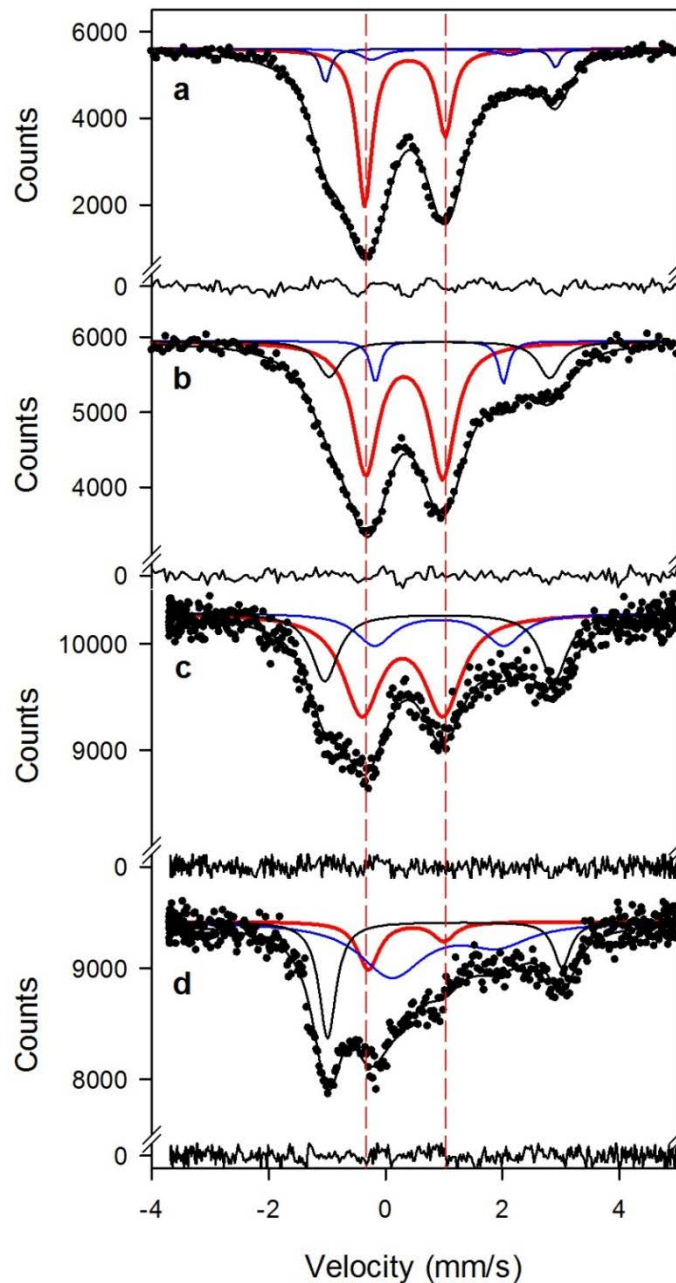


Figure 3-S4 Room temperature Mössbauer spectra of FeAlPv samples at high pressure: (a) $(\text{Mg}_{0.6}\text{Fe}_{0.4})(\text{Si}_{0.63}\text{Al}_{0.37})\text{O}_3$ perovskite (sample #1) at 83 GPa; (b) $(\text{Mg}_{0.6}\text{Fe}_{0.4})(\text{Si}_{0.63}\text{Al}_{0.37})\text{O}_3$ perovskite (sample #2) at 78 GPa; (c) $\text{Mg}_{0.78}\text{Fe}_{0.2}\text{Al}_{0.05}\text{Si}_{0.97}\text{O}_3$ perovskite (sample #3) at 75 GPa; (d) $\text{Mg}_{0.94}\text{Fe}_{0.06}\text{SiO}_3$ perovskite (sample #4) at 75 GPa. The spectra were fit to the same model shown in Fig. 3-1 (one Fe^{3+} doublet and two Fe^{2+} doublets) with the same colour scheme. Vertical red lines show that the positions of the Fe^{3+} doublets do not change with composition, demonstrating that Fe^{3+} remains in the high-spin state in FeAlPv over a wide composition range.

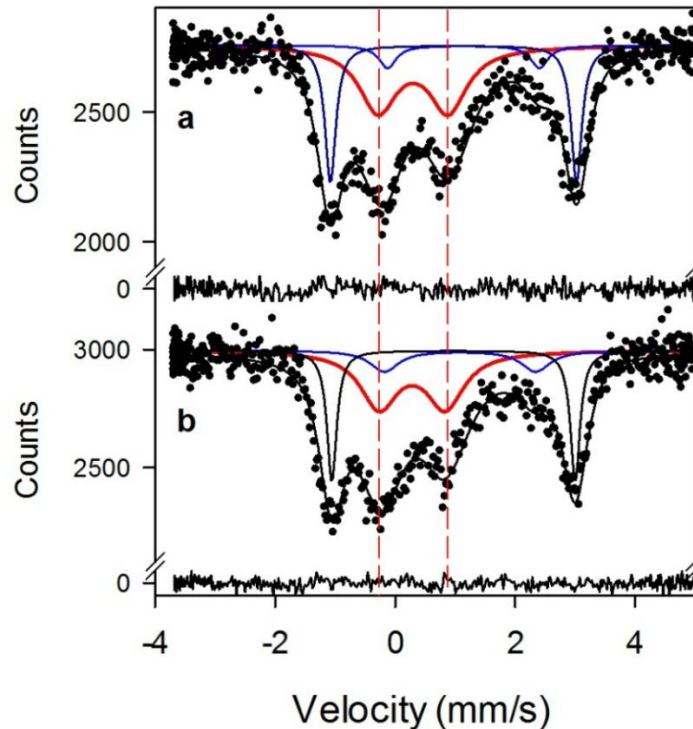
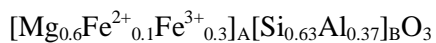


Figure 3-55 Room temperature Mössbauer spectra of $\text{Mg}_{0.78}\text{Fe}_{0.2}\text{Al}_{0.05}\text{Si}_{0.97}\text{O}_3$ perovskite (sample #3) at 86 GPa taken (a) before; and (b) after laser heating. Vertical red lines show that the positions of the Fe^{3+} doublets do not change, demonstrating that there is no shift of Fe^{3+} from the A to the B site as a consequence of laser heating, and that Fe^{3+} remains in the high-spin state.

3.4.6 Cation site distribution in the perovskite structure

Run S4850 - $(\text{Mg}_{0.6}\text{Fe}_{0.4})(\text{Si}_{0.63}\text{Al}_{0.37})\text{O}_3$ perovskite

We conducted full structural refinements of a single crystal of silicate perovskite synthesised using identical starting materials and experimental procedure (with the exception that iron was not ^{57}Fe enriched) using *in situ* X-ray diffraction data collected in a DAC at pressures up to 80 GPa and temperatures over 1700 K (Glazyrin et al., *subm.*). All refinements showed that both Fe^{2+} and Fe^{3+} occupied the A-site exclusively at all conditions studied, indicating the following site distribution:



Run S5083 - $(\text{Mg}_{0.94}\text{Fe}_{0.06})\text{SiO}_3$ perovskite

We selected a single crystal of silicate perovskite from the same high-pressure synthesis run and conducted a full structural refinement using SHELXL97 software on X-ray diffraction data collected at

Chapter 3 Effect of iron spin state on the electrical conductivity of the Earth's lower mantle

ambient conditions using an Oxford Diffraction Xcalibur diffractometer. Details of the structural refinement will be published elsewhere. The refinement showed that all iron occupied the A-site exclusively, indicating the following site distribution based on the chemical composition derived from SEM analysis:



Run S4949 - (Mg_{0.78}Fe_{0.2}Al_{0.05})Si_{0.97}O₃ perovskite

From the chemical composition and the Fe³⁺/ΣFe ratio, we determined the following site distribution:



All iron occupies only the A-site.

3.4.7 Electrical conductivity measurements

Resistance measurements were conducted at high pressure and high temperature on a sample of Mg_{0.60}Fe_{0.40}Si_{0.63}Al_{0.37}O₃ perovskite (Fe³⁺/ΣFe = 0.93±0.3) that was synthesized in the same multianvil run described in (Glazyrin et al., *subm.*). We used a BX90-type DAC [Kantor et al., *in preparation*] where a standard brilliant cut diamond with 400 μm culet was used as the first anvil, and a conventional beveled diamond with 120 μm culet was used as the second anvil. To prepare the gasket, a 50 μm diameter hole was drilled in a 25 μm thick piece of rhenium foil, after which the drilled piece of rhenium was cut into two halves using a near infrared laser with the cutting plane passing through the middle of the hole. The two rhenium foil halves were coated with a gold layer roughly 2 μm thick using a simple sputter coater and then glued onto a synthetic single crystal diamond, thus providing a split-gasket hole configuration for the sample chamber. A platinum wire with 20 μm diameter was used in a linear four-point probe scheme (see Kuznetsov (2007) for technical details). Current was supplied through two platinum leads glued onto different halves of the split-gasket and voltage was measured using the other two leads. The particular construction of the DAC used enabled the platinum leads from the gasket to emerge freely from the DAC to then be connected to measuring devices, while thin ceramic tubes prevented potential contact of the platinum wires with the metallic body of the DAC. Small pieces of sample roughly 10-12 μm in diameter and 5-7 μm thick were loaded into the middle of the split-gasket hole. Synthetic diamond powder (grain size less than 1 μm) placed in the slits between the halves of the split-gasket provided reliable insulation of the two halves of the gasket, while the sample in the split-gasket hole closed the

Chapter 3 Effect of iron spin state on the electrical conductivity of the Earth's lower mantle

circuit. The current and voltage measurements were read out using multimeters. The sample was heated using a portable laser heating system as previously described (Dubrovinsky et al., 2009).

Resistance data were collected at pressures up to 146 GPa at three different temperatures (Fig. 3-S6). The quantity σ/σ_{30} (i.e., the electrical conductivity relative to the value at 30 GPa) was calculated based on the change in height of the sample as a function of pressure that was measured in a separate experiment.

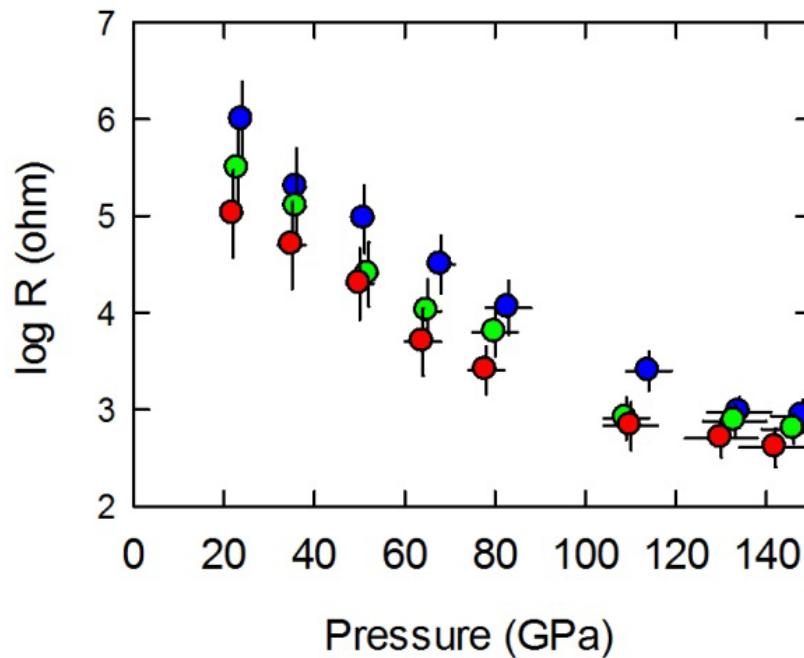


Figure 3-S6 Influence of pressure on the resistance of $\text{Mg}_{0.60}\text{Fe}_{0.40}\text{Si}_{0.63}\text{Al}_{0.37}\text{O}_3$ perovskite ($\text{Fe}^{3+}/\Sigma\text{Fe} = 0.93 \pm 0.3$) measured using a laser-heated DAC at different temperatures: blue – 1250 ± 50 K; green – 1800 ± 50 K; red – 2300 ± 100 K.

4 Iron spin state in silicate glass at high pressure: implications for melts in the Earth's lower mantle

by C. Prescher^{1*}, C. Weigel², C. McCammon¹, O. Narygina³, V. Potapkin^{1,4}, I. Kупenko^{1,4}, R. Sinmyo¹, A. I. Chumakov⁴, L. Dubrovinsky¹

¹*Bayerisches Geoinstitut, Universität Bayreuth, D-95440 Bayreuth, Germany*

²*CNRS, Laboratoire Charles Coulomb UMR 5221, F-34095, Montpellier, France*

³*PANalytical B.V., Lelyweg 1 (7602 EA), PO Box 13, 7600 AA Almelo, Netherlands*

⁴*European Synchrotron Radiation Facility, BP 220, F-38043 Grenoble, France*

*Corresponding author. Email: clemens.prescher@gmail.com

Submitted to Earth and Planetary Science Letters

4.1 Abstract

We report a Mössbauer spectroscopic study of a Fe²⁺-rich aluminous silicate glass and a Fe³⁺-rich sodium silicate glass measured in a diamond anvil cell up to 84 GPa. The hyperfine parameters vary smoothly with pressure and are consistent with a gradual increase in coordination number with pressure. Fe²⁺ and Fe³⁺ remain in the high spin state and show no evidence of spin crossover over the measured pressure range. A spin crossover may eventually occur at higher pressures; however the strong thermal broadening of the crossover region due to Boltzmann statistics implies that no sharp spin crossover would be expected at P,T conditions down to the base of the lower mantle. Our results in combination with recent solid/melt partitioning data in a chondritic system exclude the possibility of negatively buoyant melts in the Earth's lower mantle solely due to strong preferential partitioning of iron into the melt phase.

4.2 Introduction

The physical properties of melts in the Earth's mantle have a fundamental influence on the chemical and thermal evolution of the Earth. Especially the density contrast between solid and melt is a major factor affecting chemical stratification during an early magma ocean after the moon-forming impact (Tonks and Melosh, 1993; Agnor et al., 1999). At low pressure melt densities are usually smaller than the density of the corresponding solids, resulting in a buoyant melt ascending to the Earth's surface. However, experiments have shown that ultramafic melts become denser than the surrounding solids in the upper mantle, while in the transition zone this density relationship is reversed (Rigden et al., 1984; Agee and Walker, 1988; Miller et al., 1991). For the lower mantle, extrapolation of low pressure

Chapter 4 Iron spin state in silicate glasses

experiments suggests that density crossovers between solids and melts will also occur near the core mantle boundary (CMB) (Ohtani and Maeda, 2001). In support of this suggestion there exists seismological evidence of stable partial melts at the CMB (Williams and Garnero, 1996).

In principle there are two mechanisms for melts becoming denser than solids. The first mechanism is by faster densification of the melt network with pressure, e.g., coordination changes occurring in a melt at lower pressure than in the solid, while the second mechanism is by preferential partitioning of heavier elements into the melt. Recently Nomura et al. (2011) proposed the second mechanism to occur in the mid part of the lower mantle based on experiments in an olivine composition $(\text{Mg}_{0.89}\text{Fe}_{0.11})_2\text{SiO}_4$. They observed a sharp discontinuity in the pressure dependence of the Fe/Mg solid/melt partition coefficient at 76 GPa, resulting in a strong enrichment of Fe in the melt, which would produce a denser negatively buoyant melt. The sharp discontinuity was explained by an iron spin crossover seen in their XES data collected on $(\text{Mg}_{0.95}\text{Fe}_{0.05})\text{SiO}_3$ glass during room temperature compression. However, Andrault et al. (2012) reported a much lower degree of iron enrichment in silicate melt based on partitioning experiments at liquidus temperatures on a (Ca,Mg,Al,Si,Fe) oxide glass with chondritic composition, resulting in a melt that would be lighter than the surrounding mantle and hence would segregate upwards.

In order to reconcile the difference between the results of Nomura et al. (2011) and Andrault et al. (2012), it is important to understand the electronic behavior of iron in both glass and melt as a function of composition. Partitioning experiments can only provide an indirect indication of the iron spin state, while a more direct determination comes from a method such as Mössbauer spectroscopy, which is a sensitive probe for detecting structural and spin changes in Fe-bearing materials.

In this paper we present a Mössbauer spectroscopic study of a Fe^{2+} -rich and a Fe^{3+} -rich silicate glass measured *in situ* in a diamond anvil cell at pressures up to 84 GPa. We investigate the effect of pressure on the hyperfine parameters of these silicate glasses and determine whether spin crossover occurs, and then apply our results to the behavior of silicate melts at lower mantle conditions.

4.3 Experimental details

The $\text{NaFeSi}_2\text{O}_6$ (NFS) and $(\text{Mg}_{0.823}\text{Fe}_{0.135}\text{Al}_{0.057})(\text{Si}_{0.982})\text{O}_3$ (F2B) glasses were prepared from stoichiometric mixtures of dried, reagent grade Na_2CO_3 , MgCO_3 , Al_2O_3 , SiO_2 , and $^{57}\text{Fe}_2\text{O}_3$ (95.86% ^{57}Fe). The powdered mixtures were decarbonated at 750 °C for 12 h in platinum crucibles. Starting material of NFS glass was melted at 1100 °C in an electric furnace in air for 2 h. The temperature was then brought

Chapter 4 Iron spin state in silicate glasses

to 1300 °C for 2 h and finally to 1450 °C for 30 min. The melts were quenched by rapid immersion of the bottom of the crucible in water, ground to a powder and re-melted with the same cycle. This grinding–melting process was repeated three times to ensure good chemical homogeneity. Starting material of F2B glass was melted at 1600 °C in a Fe-saturated platinum crucible for 4 h and quenched by rapid immersion in a crucible of water. The ground F2B glass was then reduced in a gas-mixing furnace in a H₂-CO₂ atmosphere at 700 °C and log fO₂=-21 for 1 hour.

Diamond anvil cells with diamond culet sizes of 250 μm and a rhenium gasket with a 120 μm diameter hole were employed. The fluorescence of ruby chips (Mao et al., 1986) was used to estimate pressure before and after each measurement, whereby the error in pressure was calculated from the difference of both values.

We ran three experimental series: (1) F2B glass with neon as pressure transmitting medium measured on compression up to 83 GPa, (2) NFS glass without pressure transmitting medium measured on compression and decompression up to 56 GPa, and (3) NFS glass with neon as pressure transmitting medium measured on compression up to 84 GPa. For neon gas loading the method of Kurnosov et al. (2008) was employed.

Mössbauer spectra of F2B glass were collected using the recently developed Synchrotron Mössbauer source (SMS) (Potapkin et al., 2012) at the Nuclear Resonance beamline (ID18) (Rüffer and Chumakov, 1996) at the European Synchrotron Radiation Facility (Grenoble, France). SMS spectroscopy enables the collection of energy domain Mössbauer spectra of small samples with relatively low iron concentrations in a timescale of only minutes, compared to days of collection time using a conventional Mössbauer source. Mössbauer spectra of NFS glass were recorded at room temperature in transmission mode on a constant acceleration Mössbauer spectrometer with a nominal 370 MBq ⁵⁷Co high specific activity source in a 12-μm-thick Rh matrix. The velocity scales for all series were calibrated relative to a 25-μm-thick natural α-Fe foil and center shift values are given relative to α-Fe. F2B glass spectra were fitted using a full transmission integral with a normalized Lorentzian-squared source lineshape (Potapkin et al., 2012) and NFS glass spectra were fitted in the thin absorber approximation. The SMS linewidth was controlled before and after each sample measurement using K₂Mg⁵⁷Fe(CN)₆. The spectra were fitted using the extended Voigt based fitting method (xVBF) (Lagarec and Rancourt, 1997) as implemented in the MossA software package (Prescher et al., 2012).

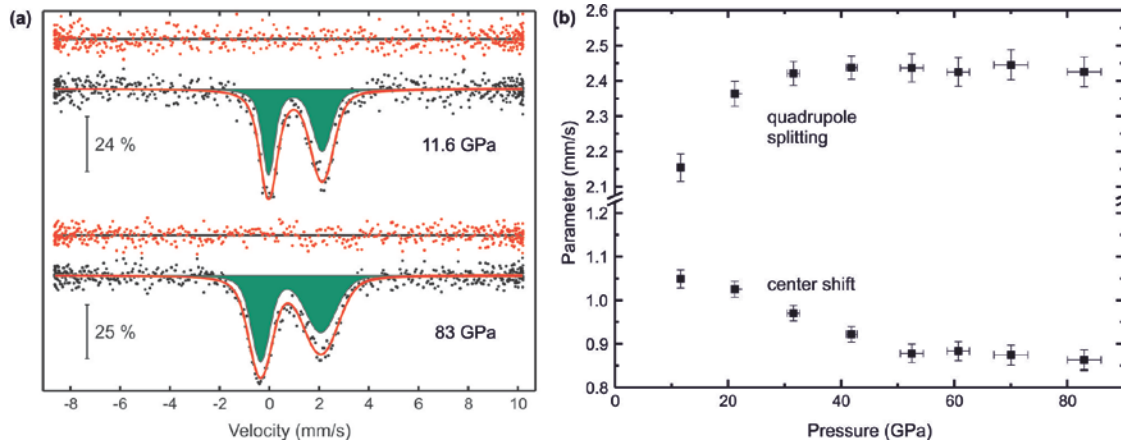


Figure 4-1 (a) Selected Mössbauer spectra of the F2B glass. (b) Variation in center shift (CS) and quadrupole splitting (QS) of Fe^{2+} with pressure up to 83 GPa. Error bars are given as 2σ of the fitted parameters.

4.4 Results

Figure 4-1a shows selected Mössbauer spectra and Fig. 4-1b shows the variation in center shift (CS) and quadrupole splitting (QS) with pressure of experimental series (1). The asymmetry in the height and width of the two peaks can be explained by a correlation between the CS and the QS. This correlation can be successfully fitted using the xVBF method (Lagarec and Rancourt, 1997), which was especially developed for disordered systems such as glasses. In the xVBF approach Gaussian distributions of CS and QS are utilized, whereby a linear correlation is allowed between the two parameters. The spectra were fitted with a Fe^{2+} doublet having a xVBF CS-QS coupling between -0.5 and -0.6; see Lagarec & Rancourt (1997) for further details. The plotted values of CS and QS are the means of the Gaussian distributions of the respective parameters. The CS decreases almost linearly up to 50 GPa and stays constant up to 83 GPa; whereas the QS increases up to 30 GPa and stays constant at higher pressures up to 83 GPa.

Figure 4-2 shows selected spectra of the NFS glass measurements. The spectra are composed of an intense Fe^{3+} doublet and a weak Fe^{2+} doublet. The widths of the doublets in experimental series (2) are highly broadened compared to those in experimental series (3). This is likely an effect due to the absence of a pressure transmitting medium, which results in higher pressure gradients and stresses throughout the sample chamber. To account for this broadening in experimental series (2) the Fe^{3+} site was modeled with two Gaussian QS components, whereas in experimental series (3) Fe^{3+} was modeled with only one QS component. The correlation between CS and QS of Fe^{3+} is almost zero for both sites in both experiments. Figure 4-3 shows the variation in hyperfine parameters with pressure. The CS and QS

Chapter 4 Iron spin state in silicate glasses

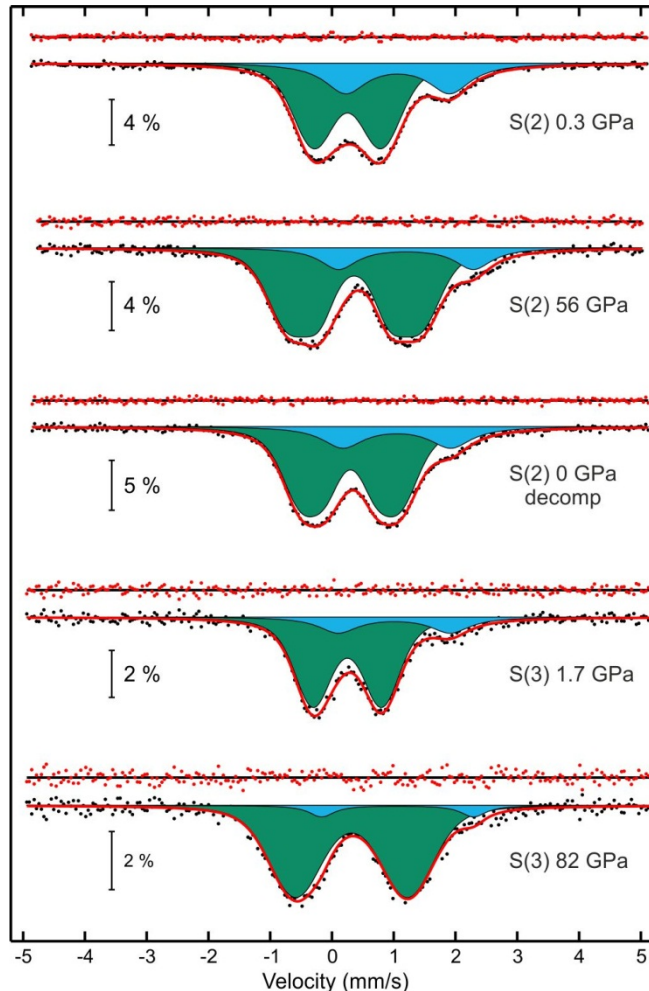


Figure 4-2 Selected Mössbauer spectra of the NFS glass. The upper three spectra are from the experimental series (2) and show from top to bottom the initial spectrum, the highest achieved pressure, and the spectrum after decompression. The lower two spectra are from experimental series (3) and show a spectrum at low and high pressure.

values of experimental series (2) were calculated as the weighted average of the two Gaussian QS distributions. The QS for both Fe^{2+} and Fe^{3+} increases up to 15 GPa, it is nearly constant between 15 and 60 GPa and it increases moderately above 60 GPa. The CS of Fe^{2+} and Fe^{3+} increases up to 15 GPa and then remains constant within experimental uncertainty up to 84 GPa. The relative area of the Fe^{3+} absorption to the Fe^{2+} absorption in series (2) increases from 70 % at 0.3 GPa to 83 % at 56 GPa and decreases on compression back to 77 %; whereas it increases in series (3) from 80 % at 1.7 GPa to 93 % at 84 GPa with pressure (Fig. 4-2).

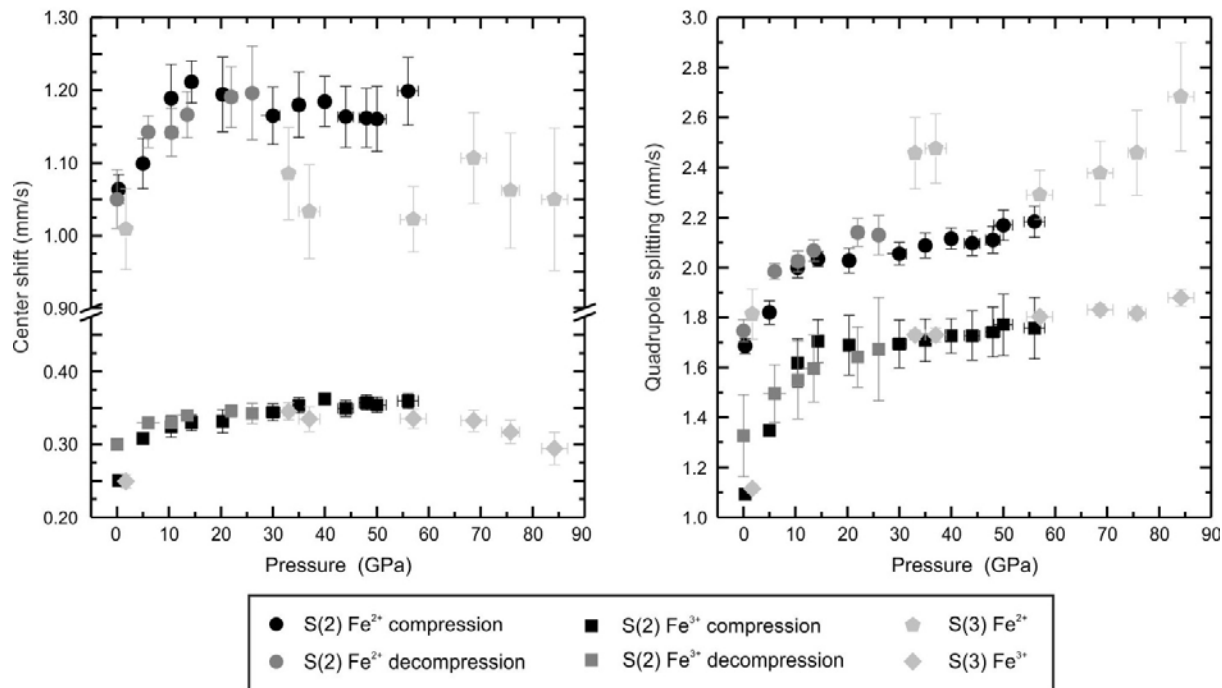


Figure 4-3 Variation of center shift and quadrupole splitting for Fe²⁺ and Fe³⁺ with pressure in NFS glass up to 84 GPa. The symbols for the experimental series (2) and (3) are indicated in the legend and parameters for the two series are plotted together. Error bars are given as 2σ of the fitted parameters.

4.5 Discussion

At sufficiently high pressures, glasses typically adapt their atomic structure to compression by changing the coordination of the atoms and decreasing their polyhedral volumes. This behavior has two opposing effects on the CS of the corresponding Mössbauer doublet. CS is a measure of the difference in s-electron density at the nucleus between the source and the absorber, whereby the sign of the change in CS for a given change in s-electron density is determined by the sign of the relative change in the nuclear radius during the transition induced by the Mössbauer γ -ray. The excited state of ⁵⁷Fe is smaller than the ground state which means that CS decreases when the electron density at the nucleus increases. Pure compression of a coordination polyhedron will decrease CS with pressure, whereas a change to a higher coordination number typically increases CS, since the distance to the surrounding oxygen ions increases and consequently the electron density at the nucleus decreases.

The CS of Fe²⁺ in the F2B glass and Fe²⁺ and Fe³⁺ in the NFS glass behave differently with compression. In the NFS glass the CS of the Fe³⁺ and the Fe²⁺ sites increases up to around 15 GPa and remains essentially constant up to the highest pressures achieved, which is consistent with a gradual increase in coordination number up to 15 GPa. On the other hand in the F2B glass the CS of Fe²⁺

Chapter 4 Iron spin state in silicate glasses

decreases up to 50 GPa and remains constant thereafter, which is consistent with a decreased interatomic distance up to 50 GPa. A similar trend has been observed for Fe^{2+} in amorphous $(\text{Mg}_{0.9}\text{Fe}_{0.1})_2\text{SiO}_4$ (Rouquette et al., 2008). However, according to the general predicted behavior of transition metals in silicate glasses under pressure, the Fe coordination number should increase with pressure (e. g. Keppler and Rubie, 1993). This suggests that while the average coordination number of Fe^{2+} in the F2B glass increases with pressure, the compression of the polyhedron due to increased pressure has a stronger influence on the s-electron density, resulting in a net CS decrease with pressure. The constant value of CS above 50 GPa suggests that there may be a change in compression mechanism at this pressure, for example a change in the coordination number of Si from 4- to 6-fold. Results for SiO_2 glass in the literature give two different transition pressures that have been estimated from experimental data obtained from different methods. Brillouin spectroscopy (Zha et al., 1994; Murakami and Bass, 2010), X-ray emission spectroscopy (XES) (Lin, Fukui, et al., 2007) and X-ray Raman scattering (Lee et al., 2008) give an estimate of 25 GPa, while X-ray diffraction measurements suggest that the density of SiO_2 glass approaches that of coesite around 40-50 GPa (Sato and Funamori, 2008; Funamori and Sato, 2010). The former methods likely indicate the onset of a gradual Si coordination change, while the latter method likely indicates the pressure at which most of the Si atoms are in 6-fold coordination in order to achieve a density similar to coesite. In addition molecular dynamic simulations of MgSiO_3 liquid show the absence of 4-fold-coordinated Si around 55 GPa (Stixrude and Karki, 2005). It is therefore reasonable to suggest that the change in slope of the CS with pressure around 50 GPa of Fe^{2+} in the F2B glass is related to a change in Si coordination number from 4- to 6-fold.

Quadrupole splitting (QS) is a measure of the electric field gradient (EFG) acting on the nucleus. In the crystal field model the EFG can be expressed as the sum of a lattice term and a valence term (Ingalls, 1964). The lattice term arises from a deviation from cubic symmetry of the surrounding atoms in the crystalline lattice, while the valence term arises from an asymmetry in the charge distribution of the valence electrons. The QS is therefore affected by the valence state and the coordination environment as well as the distortion of the crystallographic site. The pressure dependence of the QS can be negative or positive, depending on the relative magnitude of the valence and lattice terms (e. g. McCammon, 2000). The QS of Fe^{2+} and Fe^{3+} in both glasses increases in the first 15-30 GPa and remains roughly constant up to the highest pressures achieved (similar to the behavior of Fe^{2+} in amorphous $(\text{Mg}_{0.9}\text{Fe}_{0.1})_2\text{SiO}_4$; Rouquette et al. 2008). The increase can be understood as an increased distortion of the coordination polyhedron, and the slope of the QS increase with pressure is similar to that seen in the QS pressure

Chapter 4 Iron spin state in silicate glasses

dependence of high-spin Fe^{2+} and Fe^{3+} in silicate perovskite (e. g. McCammon et al., 2008) and high-spin Fe^{2+} in ferropericlasite (e.g. Lin et al., 2006).

The change in relative area of the Fe^{3+} site over the Fe^{2+} site with pressure in the NFS glass might be attributed to one or more of several effects. The first is a change of the recoil-free fractions of Fe^{2+} and Fe^{3+} relative to one another with increasing pressure. The recoil-free fraction, which is related to the mean-square displacement of the nucleus, could change differently with pressure for Fe^{3+} and Fe^{2+} due to differences in the change of the coordination environments. A second possibility is a pressure-induced oxidation of Fe^{2+} , either by reacting with residual oxygen adhering to the sample powder or by the disproportionation reaction $3\text{Fe}^{2+} \rightarrow 2\text{Fe}^{3+} + \text{Fe}^0$, forming small amounts of nanoparticle metallic iron that would not be easily detectable in the Mössbauer spectra. Without further information from other methods, it is not possible to further clarify the origin of the change in relative areas. Whatever the cause, however, the CS and QS hyperfine parameters of the Fe^{2+} and Fe^{3+} sites would not be affected, and therefore the conclusions drawn in this study remain the same.

The hyperfine parameters associated with the low-spin states of Fe^{2+} and Fe^{3+} in iron-bearing compounds generally differ significantly to their high-spin counterparts, providing a probe of spin crossover. CS and QS show a large decrease during HS-LS crossover of Fe^{2+} due to drastic changes in the shielding of the nucleus by d -electrons and the more symmetrical distribution of d -electrons in the LS state. During Fe^{3+} HS-LS crossover CS also decreases; however QS shows a large increase due to the loss of symmetry of the d -electron distribution. By comparing expected changes for HS to LS crossover of Fe^{2+} and Fe^{3+} with the measured hyperfine parameters in this study (Fig. 4-4), it is apparent that there is no evidence for spin crossover in either of the studied glasses.

Nomura et al., (2011) found evidence using X-ray emission spectroscopy for complete Fe^{2+} spin crossover in $\text{Mg}_{0.95}\text{Fe}_{0.05}\text{SiO}_3$ glass in a narrow pressure range from 59 to 77 GPa, while partial spin crossover of Fe^{2+} was found over a much larger pressure range in a pressure-induced amorphised sample of $(\text{Mg}_{0.9}\text{Fe}_{0.1})_2\text{SiO}_4$ (Rouquette et al., 2008). The higher iron concentration in the latter sample leads to enhanced iron-iron electronic exchange which stabilises the high-spin state relative to the low-spin state (e. g. Kantor et al., 2009). We observed no Fe^{2+} spin transition in the F2B glass up to 83 GPa, which can be understood through stronger iron-iron electronic exchange compared to amorphised $(\text{Mg}_{0.9}\text{Fe}_{0.1})_2\text{SiO}_4$ due to its higher iron concentration ($\text{Fe}\# = 0.14$), and also larger interatomic distances due to substitution of the larger Al^{3+} for the smaller Si^{4+} . A similar argument can be applied to explain why no Fe^{2+} spin crossover is observed up to 84 GPa in the NFS glass. Although spin crossover might eventually occur at

Chapter 4 Iron spin state in silicate glasses

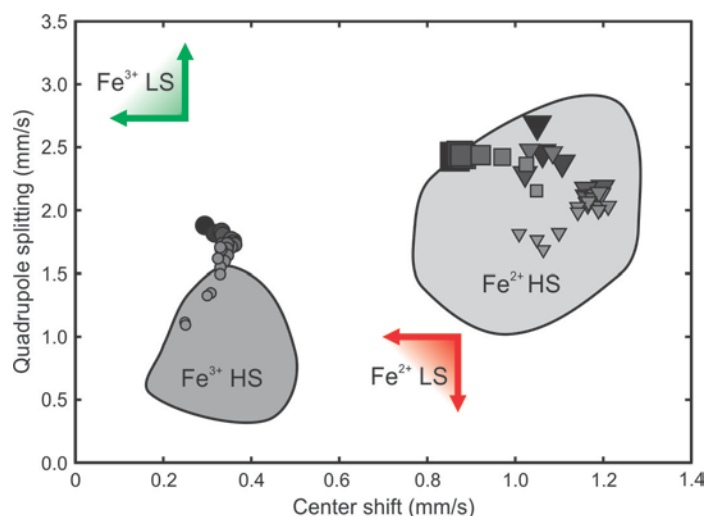


Figure 4-4 Variation of center shift (CS) and quadrupole splitting (QS) for Fe^{2+} and Fe^{3+} in glasses. Symbols indicate results from this study, where symbol size increases with increasing pressure. The shaded regions indicate values derived from Mössbauer spectra at ambient conditions of HS Fe^{2+} and HS Fe^{3+} in inorganic glasses (Dyar, 1985). Values of ΔCS and ΔQS during HS to LS transitions were taken from the literature for Fe^{2+} (amorphous olivine – Rouquette et al. (2008)) and Fe^{3+} (rare earth orthoferrites and FeBO_3 – Hearne et al. (1995); Xu et al. (2001); Sarkisyan et al. (2002)) in order to estimate the corners of the regions where LS hyperfine parameters would be predicted to fall for the glasses in the current study (indicated in red and green for LS Fe^{2+} and LS Fe^{3+} , respectively).

higher pressures, the strong thermal effect which increases the width of the crossover region according to Boltzmann statistics (e. g. Kantor et al., 2009) means that no sharp spin crossover would be expected at P,T conditions down to the base of the lower mantle.

We observe no evidence for Fe^{3+} spin crossover in the NFS glass up to 84 GPa, in contrast to reports in the literature for several other Fe^{3+} -rich oxides and silicates (Hearne et al., 1995; Xu et al., 2001; Pasternak et al., 2002; Sarkisyan et al., 2002; Catalli et al., 2010, 2011; Hsu et al., 2011). In those studies Fe^{3+} occupies a relatively undistorted octahedral site, for example Fe^{3+} in ASiO_3 perovskite undergoes a HS-LS crossover at ~ 50 GPa only when it occupies the octahedral B-site (Catalli et al., 2010, 2011; Hsu et al., 2011); whereas it remains in the HS state up to at least ~ 120 GPa when it occupies the 8-12-coordinated A-site (Catalli et al., 2010; Hsu et al., 2011). The coordination of Fe^{3+} in the NFS glass at ambient pressure is 4- to 5-fold (Weigel et al., 2008). The increasing CS from 0 to 15 GPa suggests a gradual change to higher coordination number, although it is not possible to determine the exact coordination population of Fe^{3+} from Mössbauer spectroscopy. The absence of a HS-LS spin crossover of Fe^{3+} in the NFS glass, however, suggests that Fe^{3+} coordination at high pressure differs from the highly symmetrical octahedral environment of the B-site in the perovskite structure. The crystal field splitting, a major driving factor for HS-LS crossover, is largest in an octahedral environment (e.g. Burns, 1993);

Chapter 4 Iron spin state in silicate glasses

hence a different coordination would increase the pressure of HS-LS crossover. To more accurately determine the coordination of Fe^{3+} in NFS glass at high pressure requires further investigation with measurement methods such as EXAFS that are more diagnostic for coordination number.

Nomura et al. (2011) reported a discontinuity around 76 GPa in the variation of the Fe-Mg solid/liquid partition coefficient of laser-heated olivine with pressure that they attributed to spin crossover in the melt. The sharpness of the discontinuity (width < 3 GPa) and the relative invariance of partition coefficients with pressure extending on either side of the discontinuity would require complete spin crossover over a narrow pressure range. Such behaviour would imply not only negligible iron-iron interactions in the melt and minimal variation of coordination environments between different iron atoms, but also virtually no thermal broadening of the width of the transition region (e.g. Kantor et al., 2009). Shock-wave data from a recent study of liquid Fe_2SiO_4 up to 161 GPa could be fit to a single Hugoniot (Thomas et al., 2012), suggesting either the absence of spin crossover or its occurrence over a wide pressure range. Andrault et al. (2012) performed partitioning experiments similar to those of Nomura et al. (2011), but used a chondritic-type material instead, and observed no discontinuity in the variation of solid/melt partition coefficient with pressure. Although their partition coefficients (K_D) were significantly higher (meaning that the chondritic melt is less iron-rich relative to the solid phases than the $(\text{Mg,Fe})_2\text{SiO}_4$ melt at all pressures), the chondritic K_D values do show a linear decrease from 0.60(5) at 42 GPa to 0.47(5) at 120 GPa. This decrease means that the chondritic melt does become more Fe-rich with increasing pressure, possibly due to a coordination change in the melt that stabilizes a higher concentration of iron (e.g. Murakami and Bass, 2011). However, the data of Andrault et al. (2012) lack a discontinuity, indicating that no sharp spin crossover occurs in chondritic melts at depths of the Earth's lower mantle. The results of our Mössbauer spectroscopy investigation of the electronic behavior of Fe in glasses suggests that Fe^{2+} and Fe^{3+} will remain in the HS state in more complex Al- and Na-bearing melts. Hence the magnitude of Fe enrichment is not sufficient for a chondritic silicate melt to become negatively buoyant in the Earth's lower mantle (Andrault et al, 2012). Nevertheless, such Fe enrichment coupled with the structural changes in the Si polyhedron proposed by Murakami and Bass (2011) might be sufficient to generate negatively buoyant melts near the CMB, which could explain the anomalies at the CMB seen by seismology (Williams and Garnero, 1996).

4.6 Acknowledgements

We acknowledge the European Synchrotron Radiation Facility for provision of synchrotron radiation (ID18) and we would like to thank Jean-Philippe Celse for additional technical assistance. The

Chapter 4 Iron spin state in silicate glasses

project was partly supported by funds from the German Science Foundation (DFG) through both the Priority Programme SPP1236 and a normal research grant, from the PROCOPE exchange programme, and from the German Federal Ministry for Education and Research (BMBF).

5 The effect of Fe spin crossovers on its partitioning behavior and oxidation state in a pyrolitic Earth's lower mantle system

by C. Prescher^{1*}, F. Langenhorst², L. Dubrovinsky¹ and V. Prakapenka³

¹*Bayerisches Geoinstitut, Universität Bayreuth, D-95440 Bayreuth, Germany*

²*Institut für Geowissenschaften, Friedrich-Schiller-Universität Jena, Carl-Zeiss-Promenade 10, D-07745 Jena, Germany*

³*Consortium for Advanced Radiation Sources (CARS), University of Chicago, Chicago, IL 60637, USA*

*Corresponding author. Email: clemens.prescher@gmail.com

For submission to Science

5.1 Abstract

Geophysical interpretations of the Earth's interior and its dynamics are significantly influenced by phase transitions of the constituting minerals and their chemical compositions. Pressure induced Fe spin crossovers in the main mineral phases of the Earth's lower mantle, Mg-Fe silicate perovskite and ferropericlase, have been suggested to influence Fe partitioning resulting in separate layers with distinct physical properties. However, previous results remain ambiguous regarding the exact effect of Fe spin crossovers and the actual transition pressures. We observe here a continuous decrease of the Fe²⁺-Mg partition coefficient K_D between silicate perovskite and ferropericlase from 25 GPa to 79 GPa in a pyrolitic Earth's lower mantle system. At about 97 GPa the K_D significantly increases with an accompanied decrease of the Fe³⁺/ΣFe ratio in perovskite, which therefore leads to an amplified change in the Fe²⁺ K_D . We conclude that the Fe²⁺ high-spin to low-spin crossover in ferropericlase and the Fe²⁺ high-spin to intermediate spin crossover in perovskite at mid-lower mantle pressures (30-80 GPa) exert no control on K_D , but the Fe²⁺ intermediate-spin to low-spin crossover in silicate perovskite at about 100 GPa preferentially partitions Fe into silicate perovskite and reduces its Fe³⁺ content. The change in oxidation state and partitioning behavior of Fe will increase thermal conductivity and probably could induce a thermal boundary layer at this depth.

5.2 Manuscript

The concentration of iron and its oxidation state in minerals of the Earth's lower mantle are fundamental for understanding the structure and dynamics of the Earth's interior. Both factors significantly influence densities, elasticity, and transport properties such as electrical and thermal conductivities of the major minerals constituting the lower mantle. In comparison to the complex structure of the Earth's upper mantle, the lower mantle is considered to be relatively homogeneous.

Chapter 5 Partitioning behavior and oxidation state of Fe in the Earth's lower mantle

However, recent seismological studies have demonstrated that discontinuities exist in the upper and lower sections of the lower mantle (Hitoshi and Fenglin, 1994; Williams and Garnero, 1996; Kaneshima, 1999; van der Hilst, 1999). These discontinuities have been attributed either to the presence of remnant subducted slabs (Hitoshi and Fenglin, 1994; Kaneshima, 1999), melts (3), or electron spin crossovers in Fe-bearing materials (Badro et al., 2003b). To assign these discontinuities to a specific origin, precise investigation of phase relations and partitioning behavior between the minerals constituting the Earth's lower mantle is needed.

In a pyrolitic mantle system, major phases constituting the Earth's lower mantle are Mg-silicate perovskite (Mg-Pv), ferropericlase (Fp) and Ca-silicate perovskite (Ca-Pv). In addition, majorite garnet (Fujino et al., 2012) and post-perovskite (Murakami et al., 2004) are present in the uppermost and lowermost parts of the lower mantle, respectively. Experimental investigations in simplified MgO-FeO-SiO₂ systems have shown that Fe preferentially partitions into Fp relative to Mg-Pv (Ito and Takahashi, 1989; Sinmyo et al., 2008; Sakai et al., 2009; Narygina et al., 2011; Nakajima et al., 2012). However, in more complex systems, particularly in the presence of Al, the Fe-Mg partitioning coefficient between Mg-Pv and Fp [$K_D = (\text{Fe}/\text{Mg})_{\text{Mg-Pv}}/(\text{Fe}/\text{Mg})_{\text{Mw}}$] increases considerably due to the coupled incorporation of Fe³⁺ and Al³⁺ for Mg²⁺ and Si⁴⁺ in Mg-Pv (Frost and Langenhorst, 2002; Kesson et al., 2002; Murakami et al., 2005; Irifune et al., 2010). Laser heated diamond anvil cell (LHDAC) studies report a K_D of ~0.4-0.5 in the pressure and temperature conditions throughout the entire lower mantle (Kesson et al., 2002; Murakami et al., 2005). However, multi-anvil studies have shown a K_D increasing to almost unity in the top of the lower mantle (30 GPa) with a subsequent drop in K_D at 40 GPa to the values obtained by LHDAC experiments (Irifune et al., 2010). All of the previous investigations on the Fe partitioning behavior in the Earth's lower mantle have reported K_D values for bulk iron content in the constituting minerals, neglecting the oxidation state of iron. It is however well known that Fe³⁺ is structurally stabilized in Mg-Pv (Frost et al., 2004) and thus the oxygen fugacity may exert an important control on the partitioning of iron in the Lower mantle. Furthermore, the Fe³⁺ content is a major factor determining the physical properties of Mg-Pv and Fp, such as their elasticities (Glazyrin et al., *subm.*) and thermal conductivities (Goncharov et al., 2009; Goncharov, Prakapenka, et al., 2010). Besides the Fe³⁺ content, electron spin crossovers of Fe in Fp and Mg-Pv have been proposed to significantly alter the K_D in favor of the phase with stable Fe (Badro et al., 2003a).

To estimate the effect of spin crossovers on the partitioning behavior and oxidation state of Fe, we have separately determined the Fe²⁺ and Fe³⁺ partitioning coefficients between Mg-Pv and Fp in a pyrolitic lower mantle system. LHDAC experiments were conducted in the pressure range from 26 to 130

Chapter 5 Partitioning behavior and oxidation state of Fe in the Earth's lower mantle

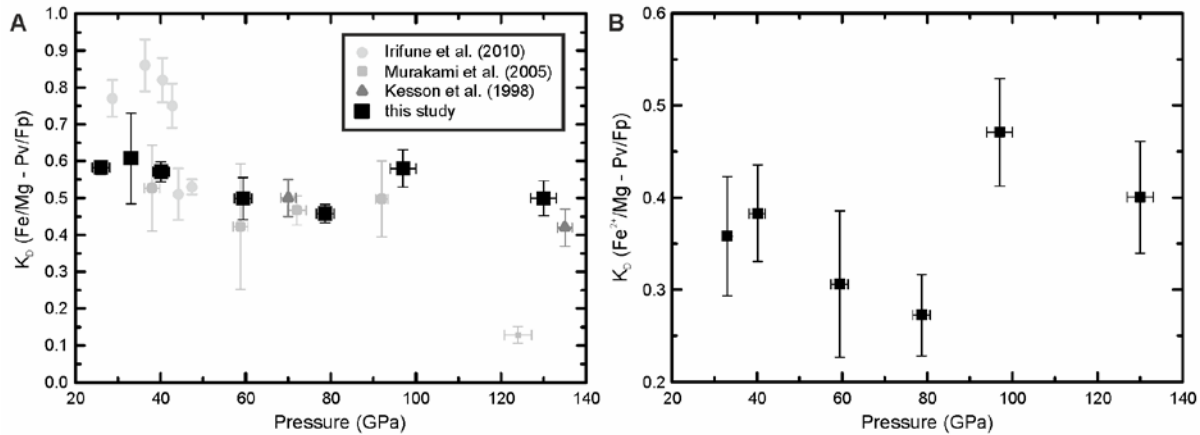


Figure 5-1 (a) Variations of the Fe-Mg K_D between Mg-Pv and Fp in pyrolite as a function of pressure. Data is compared with previous studies on a pyrolitic lower mantle assemblage. (b) Calculated Fe^{2+} -Mg K_D between Mg-Pv and Fp in pyrolite on the basis of the bulk Fe K_D and $\text{Fe}^{3+}/\Sigma\text{Fe}$ ratios estimated. The Fp $\text{Fe}^{3+}/\Sigma\text{Fe}$ ratio at 97 GPa has been estimated by linear interpolation between the adjacent points. The pressure evolution shows a discontinuity at about 97 GPa probably produced by the IS-LS crossover of Fe^{2+} in Mg-Pv.

GPa and at temperatures along a typical adiabatic geotherm (Supplementary materials). The chemical compositions of the coexisting minerals in the recovered samples were quantified by energy dispersive x-ray spectroscopy in the transmission electron microscope. Fe valence states were determined by Mössbauer spectroscopy for the starting material and by electron energy loss spectroscopy (EELS) for the recovered diamond anvil cell samples.

The concentrations of major elements in Mg-Pv stay almost constant over the entire pressure range investigated (Table S2), whereas the Fe content in Fp increases from 26 GPa to 79 GPa, drops at 97 GPa and increases again at 130 GPa. The resulting bulk Fe K_D is thus largely controlled by the variation of Mg and Fe contents in Fp. The K_D linearly decreases from 0.58 at 26 GPa to 0.45 at 79 GPa, then abruptly increases to 0.57 at 97 GPa and decreases again to 0.48 at 130 GPa (Fig. 1(a)). The $\text{Fe}^{3+}/\Sigma\text{Fe}$ ratio in Mg-Pv is 42(5) % in the starting material (Fig S1) and stays almost constant up to 79 GPa; at 97 GPa it drops to ~30 % (Fig. 2(a),(d)). On the contrary, the $\text{Fe}^{3+}/\Sigma\text{Fe}$ ratio of Fp increases from under 5 % in the starting material to about 16 % at 59 GPa and stays constant up to 130 GPa (Fig. 2(b),(d)). By combining bulk Fe K_D and the $\text{Fe}^{3+}/\Sigma\text{Fe}$ ratios we can estimate the partitioning coefficient of Fe^{2+} and Fe^{3+} separately (Fig. 1(b), S1). The Fe^{3+} partitioning coefficient decreases in the investigated pressure range and reaches almost unity at 130 GPa (Fig. S2), whereas the Fe^{2+} partitioning coefficient first decreases linearly up to 79 GPa from 0.4 to 0.22, jumps to 0.57 at 97 GPa and decreases again at 130 GPa (Fig. 1(b)).

Chapter 5 Partitioning behavior and oxidation state of Fe in the Earth's lower mantle

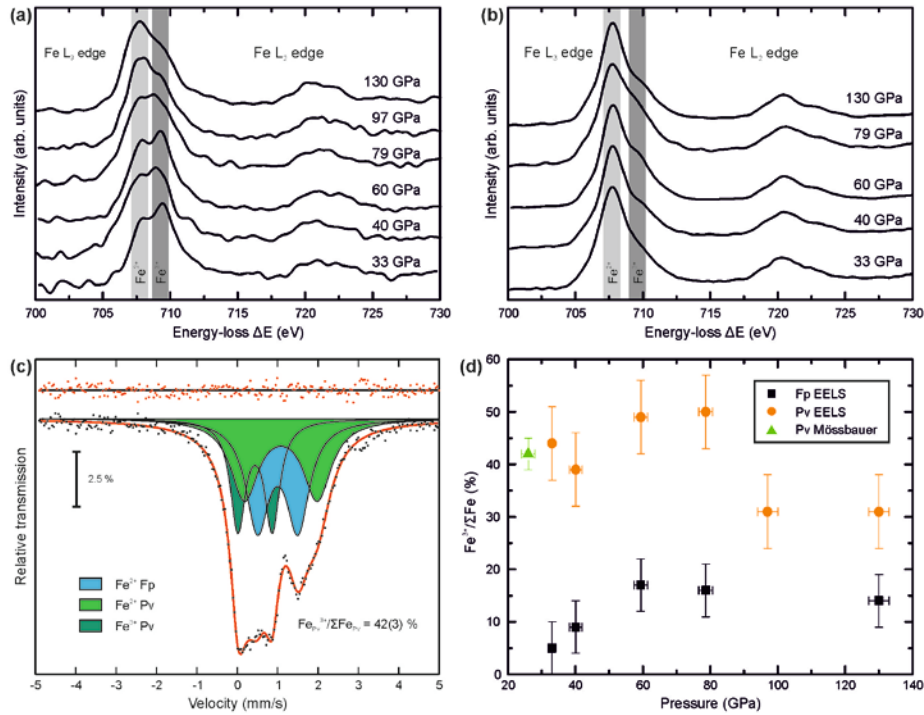


Figure 5-2 Respective Fe $L_{2,3}$ electron energy loss spectra (EELS) of **(a)** Mg-Pv and **(b)** Fp at each pressure point. **(c)** Mössbauer spectrum of the pyrolitic starting material synthesized in a multianvil apparatus. **(d)** Variation in $Fe^{3+}/\Sigma Fe$ ratio of Mg-Pv and Fp in pyrolitic lower mantle system with pressure and the respective geotherm temperatures.

In the last decade, it has been demonstrated by experimental and theoretical studies that an electronic high-spin (HS) to low-spin (LS) crossover of Fe^{2+} occurs in Fp over a large pressure range from ~ 35 GPa to 80 GPa (Badro et al., 2003b; Lin et al., 2005; Lin, Vankó, et al., 2007). The effective ionic radius of Fe^{2+} in LS state is smaller than that of Mg^{2+} , which should significantly alter the partitioning behavior. Recently, this spin crossover has been proposed to induce a discontinuity in K_D in a pyrolitic composition at ~ 40 GPa (Irifune et al., 2010). However, our results and previous estimates (Murakami et al., 2005) lack abrupt changes at this pressure and show a rather smooth decrease of K_D , which is a reasonable behavior considering the broad pressure range of the spin crossover. Two other studies using San Carlos olivine with a composition of $(Mg_{0.9}Fe_{0.1})SiO_4$ as starting material proposed a gradual decrease in K_D above pressures of ~ 70 GPa (16, 17). On the contrary, a careful examination of chemical heterogeneity using the same starting material and LHDAC technique actually shows an increase of K_D in this pressure range (Sinmyo et al., 2008). Thus, it is unclear whether the Fe^{2+} spin crossover in Fp really affects the K_D in an olivine system or whether variations can be explained by experimental uncertainties. In case of pyrolitic composition reported so far data suggest that the spin crossover in Fp does not have a pronounced effect on K_D (Fig. 1 and (Murakami et al., 2005)).

Chapter 5 Partitioning behavior and oxidation state of Fe in the Earth's lower mantle

Electronic spin crossovers of Fe have also been reported for Mg-Pv but data on the spin crossover pressures do not give a uniform picture. Some authors propose an onset of a Fe²⁺ HS to intermediate-spin (IS) crossover at about 35 GPa (McCammon et al., 2008), whereas others suggest that Fe²⁺ and Fe³⁺ occupying the bicapped trigonal prism ("A") crystallographic site stay in HS state, and only Fe³⁺ occupying the octahedral ("B") site undergoes HS to LS crossover at 40-60 GPa (Catalli et al., 2010). Additionally, it has been shown that Fe²⁺ becomes LS in Mg-Pv at about 110 GPa at high temperature (McCammon et al., 2010). The ionic radii of HS and IS Fe²⁺ are similar, whereby there is a decrease in electronic entropy which may lower the K_D at the HS-IS crossover. However, the IS-LS crossover occurs over a large pressure range (McCammon et al., 2008) and overlaps with the HS-LS crossover in Mw which makes it difficult to assign the smooth decrease of K_D to either spin crossovers. Nevertheless, a relatively narrow Fe²⁺ IS to LS crossover would result in a preferential partitioning of Fe²⁺ into Mg-Pv due to a change in atomic radii being shown by an increase in K_D . This is exactly what can be seen in the behavior of the bulk and Fe²⁺ K_D (Fig. 1) at ~100 GPa. An effect of the HS-LS crossover in Fe³⁺ occupying the B-site of the Mg-Pv structure on the K_D in a pyrolitic composition is improbable. From calculated cation occupation (table S2) of the A and B sites of Mg-Pv and single crystal XRD (Glazyrin et al., *subm.*) it has been shown that Fe³⁺ only occupies the A site.

The discontinuous change in K_D is mainly caused by a decrease in Fe content in Fp and is accompanied by a relative decrease of the Fe³⁺ content in Mg-Pv, whereby the bulk Fe concentration in Mg-Pv remains the same, resulting in an amplified increase in the Fe²⁺ K_D (Fig 1). On the basis of the change in K_D and the change in Fe³⁺ in Pv at 97 GPa we propose that the electronic IS-LS crossover of Fe²⁺ not only affects the partitioning behavior of Fe²⁺, it also may cause a self-reduction of Fe³⁺ to Fe²⁺ in Mg-Pv. Experimental investigations of the Fe³⁺/ΣFe ratio in Al-bearing Mg-Pv at low pressures have shown that the Fe³⁺ content is mainly controlled by the Al content due to the coupled substitution of (Mg²⁺,Fe²⁺) - Si⁴⁺ with Fe³⁺- Al³⁺ (Lauterbach et al., 2000; Frost and Langenhorst, 2002). Due to the Fe²⁺ IS-LS crossover this relationship is eventually reversed at high pressures. The coupled substitution mechanism is still dominant, but the self-reduction of Fe³⁺ to Fe²⁺ results in a decreasing Al content (Fig. S2). The Al content of Ca-Pv and Mw stays constant at this pressure; therefore it is unclear where the excessive Al remains. A possibility would be the formation of a small amount of an Al-rich phase, although we did not see any direct evidence for the presence of the additional phase either in-situ by x-ray diffraction or in the TEM.

The reduction of Fe³⁺ to Fe²⁺ needs to be balanced by oxidation of some other components. Diamond or volatile species such as CH₄ or H₂ could be oxidized to form CO₂ or H₂O. In the DAC experiments probably the diamond anvils were the reaction partner; however, the budget of those

Chapter 5 Partitioning behavior and oxidation state of Fe in the Earth's lower mantle

components in the Earth's lower mantle is too low (probably on the order of 2000 p.p.m. (Wood et al., 1996)) to account for the reduction alone. A more realistic scenario for the Earth would be that the amount of metallic Fe by disproportionation of Fe^{2+} (Frost et al., 2004) during crystallization of an early magma ocean is reduced at this depth.

Another important effect of the change in Fe^{3+} content of Mg-Pv is the induced change in thermal conductivity. It has been shown that the radiative contribution of the thermal conductivity in Mg-Pv mainly depends on its Fe^{3+} content due to Fe^{2+} - Fe^{3+} and Fe^{3+} - O^{2-} charge transfer bands (Goncharov et al., 2009; Goncharov, Struzhkin, et al., 2010). A decrease of Fe^{3+} content at 97 GPa will increase the thermal conductivity, creating a discontinuity which could act as thermal boundary layer between the mid-lower mantle and the lowermost lower mantle.

5.3 Materials and methods

A pyrolitic starting powder was prepared from reagent grade oxides with Fe added as hematite. The oxides were ground together, cold pressed into pellets and then fired in a CO-CO₂ gas mixing furnace at 1000 °C for 1 day at an oxygen fugacity 2 log units below the fayalite magnetite quartz buffer. Quenched samples were re-ground thoroughly. The pyrolitic lower mantle assemblage was synthesized employing a multianvil press with 7/3 octahedral pressure assemblies. A LaCrO₃ furnace and a Re capsule were used. The experiment was run for 8 hours at 25 GPa and 1650 °C. The recovered sample was crushed and subsequently used as starting material for the diamond anvil cell experiments. A Mössbauer spectrum of the starting material was recorded at room temperature in transmission mode on a constant acceleration Mössbauer spectrometer with a nominal 370 MBq ⁵⁷Co high specific activity source in a 12- μm-thick Rh matrix. The velocity scale was calibrated relative to a 25-μm-thick natural α-Fe foil. The spectrum was analyzed with the MossA software package (Prescher et al., 2012).

Six separate laser heated diamond anvil experiments between 33 to 130 GPa were conducted. Ne was used as pressure medium and pressure calibrant (Kurnosov et al., 2008). A double-sided YLF laser system with a Pi-shaper was used for heating the samples to temperatures corresponding to respective geotherm temperatures at each pressure. Each sample was heated for at least 30 minutes to ensure equilibrium. Detailed experimental conditions are given in table S1. X-ray diffraction maps of every experiment were measured before and after heating using a monochromatic X-ray beam (0.3344 Å) at 13ID-D of the Advanced Photon Source (APS), Argonne National Laboratory (ANL).

Chapter 5 Partitioning behavior and oxidation state of Fe in the Earth's lower mantle

Thin slices of 30-60 nm thickness were prepared from the central laser heated part of the recovered samples and the starting material using the FEI Quanta3D field-emission FIB-SEM. These slices were observed in a PHILIPS CM20 FEG (field emission gun) STEM operating at 200 kV. To reduce electron irradiation damage during operation, TEM thin foils were cooled to nearly liquid nitrogen temperature (ca. 100 K) in a Gatan cooling holder. Compositions were measured with a ThermoNoran Vantage energy-dispersive (EDX) system equipped with a Norvar ultra-thin window and a germanium detector. The method of van Cappellen and Doukhan (Cappellen and Doukhan, 1994) for quantification of EDX microanalysis was used. EDX maps were measured for every recovered sample in order to detect possible diffusion gradients. The $\text{Fe}^{3+}/\Sigma\text{Fe}$ ratios were analyzed using a Gatan PEELS 666 (parallel electron energy-loss spectrometer). The determination of the $\text{Fe}^{3+}/\Sigma\text{Fe}$ ratio was based on the quantification method of (van Aken and Liebscher, 2002). This method is based on the white line intensities at the Fe L_{23} edge. Fe L_{23} ELNES spectra were measured in diffraction mode with convergence and collection semi-angles of $\alpha=8$ mrad and $\beta=2.7$ mrad and an energy dispersion of 0.01 eV per channel. An energy resolution, measured as width of the zero-loss peak at half maximum, of 0.8-0.9 was obtained. Special care was taken to only measure fresh crystalline grains of magnesium silicate perovskite, since Mg-Pv easily amorphizes under the high electron flux needed for EELS measurements. To check for possible beam induced changes in valence state, six spectra were measured in a time series with integration times of 20 s each. Spectra were then corrected for dark current and channel-to-channel gain variation. The pure single-scattering core-loss signal was extracted by subtracting an inverse power-law background and removing the multiple scattering contribution by the Fourier-ratio technique (Egerton, 1996). The $\text{Fe}^{3+}/\Sigma\text{Fe}$ ratio of Fp at 97 GPa is missing due to a sample loss during the investigation in the TEM. However, there is no anomaly expected at this pressure for the $\text{Fe}^{3+}/\Sigma\text{Fe}$ ratio in Fp, since both adjacent ratios are almost the same. Error evaluation for the $\text{Fe}^{3+}/\Sigma\text{Fe}$ ratios is difficult. Van Aken and Liebscher (2002) reported that the errors using their white line integration method would be on the order of 0.015. However, we have chosen the errors to be larger to be confident that the variation of $\text{Fe}^{3+}/\Sigma\text{Fe}$ ratios are really significant. For Fp a value of 0.05 and for Pv a value of 0.07 have been used. The error of the $\text{Fe}^{3+}/\Sigma\text{Fe}$ in Pv was chosen to be larger to resemble the error introduced by the strongly overlapping peaks at the L_3 edge.

5.4 Acknowledgements

The authors thank N. Miyajima for assistance in the TEM laboratory and C. McCammon for providing help in the Mössbauer laboratory.

Chapter 5 Partitioning behavior and oxidation state of Fe in the Earth's lower mantle

Table 5-S1 Experimental conditions of the laser heated diamond anvil cell experiments. Errors in pressure were calculated by estimating the pressure from the Ne equation of state before and after the heating procedure. Temperatures are calculated as mean values from measured temperatures every minute of the 30 minute laser heating time. Errors in temperatures are calculated as standard mean deviation.

Sample	Pressure (GPa)	T (K)	D _c (μm)	D _s (μm)
PyAPS-C6	33(1)	1980(80)	250	120
PyAPS-C4	40(2)	2120(150)	250	120
PyAPS-C5	59(2)	2190(90)	250	120
PyAPS-C2	79(2)	2300(140)	120 _B	60 _L
PyAPS-C1	97(3)	2450(140)	120 _B	60 _L
PyAPS-C7	130(3)	2500(150)	60 _B	30 _L

D_c – diamond anvil culet diameter, B – beveled diamond anvil; D_s – sample hole diameter, L – was drilled by Laser

Table 5-S2 Element composition of Fp calculated per 1 oxygen and element composition of Mg-Pv calculated per 3 oxygens.

Pressure (GPa)	Fp					Mg-Pv						
	Mg	Fe	Cr	Al	Na	Mg	Fe	Ca	Cr	Al	Si	Ti
26(2)	0.800(5)	0.158(4)	0.0065(6)	0.0015(9)	0.027(2)	0.85(1)	0.098(2)	0.019(5)	0.0036(6)	0.05(1)	0.957(6)	0.0087(8)
33(1)	0.82(3)	0.16(2)	0.004(3)	0.004(4)	0.027(8)	0.85(2)	0.101(6)	0.019(2)	n.d.	0.066(27)	0.95(2)	0.0102(14)
40(2)	0.83(2)	0.15(1)	n.d.	0.005(2)	0.023(7)	0.89(3)	0.091(3)	0.011(9)	n.d.	0.054(4)	0.955(6)	n.d.
59(2)	0.80(3)	0.17(3)	n.d.	n.d.	0.02(1)	0.88(2)	0.095(10)	0.016(3)	n.d.	0.058(5)	0.95(1)	n.d.
79(2)	0.77(1)	0.19(1)	n.d.	0.01(5)	n.d.	0.87(1)	0.097(3)	0.017(3)	n.d.	0.058(3)	0.95(1)	n.d.
97(3)	0.79(1)	0.155(3)	0.006(1)	0.001(1)	0.027(2)	0.86(1)	0.096(3)	0.019(4)	0.0033(7)	0.043(3)	0.96(1)	0.008(1)
130(3)	0.78(1)	0.167(4)	0.008(1)	0.004(4)	0.018(8)	0.87(1)	0.090(9)	0.017(2)	0.0038(6)	0.045(5)	0.96(1)	0.009(1)

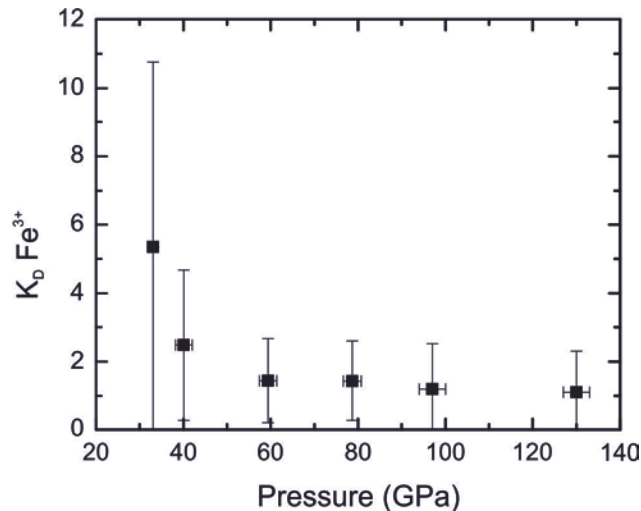


Figure 5-S1 Calculated Fe^{3+} -Mg K_D between Mg-Pv and Fp in pyrolite on the basis of the bulk K_D and $\text{Fe}^{3+}/\Sigma\text{Fe}$ ratios estimated. The Mw $\text{Fe}^{3+}/\Sigma\text{Fe}$ ratio at 97 GPa has been estimated by linear interpolation between the adjacent points.

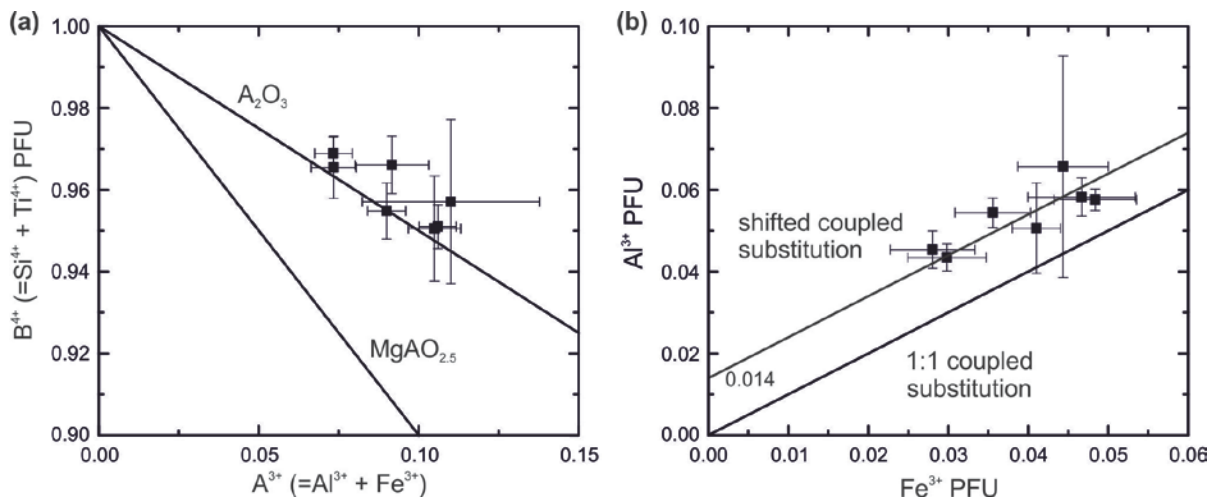


Figure 5-S2 (a) Plot of the 4-valent cations (Si^{4+} and Ti^{4+}) against the 3-valent cations (Al^{3+} and Fe^{3+}) per formula unit (PFU) in Mg-Pv. The lines indicate two possible substitution mechanisms, the A_2O_3 substitution indicates that the incorporation of A^{3+} cations takes place onto both six-fold and eight-fold sites (coupled substitution), while the $\text{MgAO}_{2.5}$ substitution indicates that A^{3+} cations are only incorporated on the six-fold site and the charge is balanced by oxygen vacancies. **(b)** Plot of Al^{3+} against Fe^{3+} content per formula unit (PFU) in Mg-Pv showing that all Fe^{3+} is charge balanced by Al through a $\text{Fe}^{3+}\text{AlO}_3$ component. The shift of the 1:1 lines indicates that an Al_2O_3 component is also present with an abundance determined by the y-axis intersection (0.014).

6 Structurally hidden magnetic transitions in Fe₃C at high pressures

by C. Prescher^{1*}, L. Dubrovinsky¹, C. McCammon¹, K. Glazyrin¹, Y. Nakajima¹, A. Kantor^{1,2}, M. Merlini^{2,3}, M. Hanfland²

¹*Bayerisches Geoinstitut, Universität Bayreuth, D-95440 Bayreuth, Germany*

²*European Synchrotron Radiation Facility, BP 220, F-38043 Grenoble, France*

³*Dipartimento di Scienze della Terra, Università degli Studi di Milano, Via Botticelli 23, I-20133 Milano, Italy*

*Corresponding author. Email: clemens.prescher@gmail.com

Physical Review B Rapid Communications (2012) 85(14), 6-9

6.1 Abstract

We report a Mössbauer spectroscopic study of cementite (Fe₃C) in a diamond anvil cell up to 88 GPa. The hyperfine parameters reveal a two-stage loss of magnetism in Fe₃C: a ferro- to paramagnetic transition around 8 to 10 GPa and a spin transition at about 22 GPa. Full structural refinement based on single-crystal X-ray diffraction data collected at pressures up to ~50 GPa reveals that there are no structural changes associated with the electronic transitions in Fe₃C. Our study resolves the long standing controversy regarding the nature of phase transitions of Fe₃C at high pressure.

6.2 Introduction

Carbon is one of the candidate light elements for the Earth's core (Wood, 1993). The importance of carbon for the Earth's interior has motivated many high pressure experimental and computational investigations of iron carbide Fe₃C (mineral name cohenite), both for its potential as an accessory mineral of the Earth's lower mantle and also as one of the probable components of the Earth's inner core. Moreover Fe₃C is a common component of steels and has interesting physical properties – it is a metallic ferromagnet with a Curie temperature of 483 K and exhibits the Invar effect in the ferromagnetic state below T_C (Tsuzuki et al., 1984; Acet et al., 2001; Wood et al., 2004).

At ambient conditions the cementite structure has orthorhombic symmetry (space group Pnma) with two independent iron positions (one iron surrounded by 12 other iron atoms, while the other has 11 iron neighbors). Carbon is surrounded by 6 iron atoms forming a trigonal prism (Fig. 6-S1).

Despite the large number of investigations the transition pressure from the ferromagnetic state to the paramagnetic or nonmagnetic state is still highly debated. Investigations probing directly the atomic or electronic structure of iron revealed transition pressures of ~6 GPa by synchrotron Mössbauer

Chapter 6 Structurally hidden magnetic transitions in Fe₃C

spectroscopy (nuclear forward scattering) (Gao et al., 2008), 10 GPa by X-ray magnetic circular dichroism (XMCD) (Duman et al., 2005) and 25 GPa by X-ray emission spectroscopy (XES) (Lin et al., 2004); whereas by means of indirect methods several different effects at higher pressures were observed which the investigators attributed to a change in the electronic state of iron: a softening of phonon frequencies observed by IXS around 68 GPa (Fiquet et al., 2009) and a change in behavior of lattice parameters above 55 GPa observed by X-ray diffraction (Ono and Mibe, 2010). Furthermore *ab initio* calculations suggest that the non-magnetic state becomes stable only above 60 GPa (Vocadlo et al., 2002).

The span of the transition pressure range is too large to be attributed to different pressure calibrations or experimental uncertainties. If we assume that different studies employed the same well-characterized iron carbide starting material, the only plausible explanation for the discrepancies is that different investigations probed different transitions in Fe₃C that led to different observable effects which only can be detected by specific methods.

In order to clarify these phase transition(s) we performed a Mössbauer spectroscopic study of Fe₃C up to 88 GPa and a single-crystal X-ray diffraction study up to 47 GPa, both measured in a diamond anvil cell. Mössbauer spectroscopy is one of the traditional methods addressing magnetic properties of iron-bearing materials; it provides direct information on the magnetic and electronic properties of iron atoms. Furthermore, single crystal X-ray diffraction provides precise and unambiguous information on the effect of magnetic or electronic transition(s) on crystal structure.

6.3 Experimental details

The Fe₃C sample powder for the Mössbauer spectroscopic study was synthesized from a mixture of 80 wt. % carbon and 20 wt. % iron (~95 % enriched in ⁵⁷Fe) treated at 5 GPa and 1200 °C for 3 h in a MgO capsule using a multianvil press at the Bayerisches Geoinstitut. We employed a LaCrO₃ heater assembly and controlled temperature based on a W₇₅Re₂₅/W₉₇Re₃ thermocouple. X-ray diffraction and Mössbauer spectroscopy confirmed that the synthesized material consisted mainly of Fe₃C, but with an excess of carbon. Fe₃C was cleaned from the carbon by magnetic separation. The single crystals were synthesized from pure iron in a carbon capsule at 5 GPa and 1300 °C in a multianvil press.

Diamond anvil cells with diamond culet sizes of 250 μm and a rhenium gasket with a 120 μm diameter hole were employed. Neon gas was used as a pressure transmitting medium to improve hydrostaticity (Kurnosov et al., 2008) and the fluorescence of ruby chips was used to measure pressure

Chapter 6 Structurally hidden magnetic transitions in Fe₃C

(Mao et al., 1986) before and after each measurement, whereby the error was calculated from the difference of both values.

⁵⁷Fe Mössbauer spectra were recorded at room temperature in transmission mode on a constant acceleration Mössbauer spectrometer with a nominal 370 MBq ⁵⁷Co high specific activity source in a 12 μm thick Rh matrix. The velocity scale was calibrated relative to 25 μm thick α-Fe foil using the positions certified for (former) National Bureau of Standards reference material no. 1541; line widths of 0.36 mm/s for the outer lines of α-Fe were obtained at room temperature. Spectra took 1 to 6 days each to collect, and Mössbauer spectra were fitted to Lorentzian line shapes using the software package MossA (Prescher et al., 2012).

Single-crystal high pressure DAC experiments were conducted at ID09a at the European Synchrotron Radiation Facility (ESRF). Diffraction data were collected at 293K using the MAR555 Flatpanel detector, radiation with a wavelength of 0.4148 Å, beam size of 10×10 μm² and a crystal-to-detector distance of about 310 mm. 120 frames in the ω-scanning range of -30° to +30° were collected (0.5° scanning step size) with an exposure time of 1 s. The data were processed using the CrysAlis[®] software (Oxford Diffraction (2006) CrysAlis RED, Version 1.171.31.8. Oxford Diffraction Ltd, Abingdon, Oxfordshire, UK). Crystal structure refinements of integrated intensities were carried out using the SHELXL-97 WinGX version [3].

6.4 Results and Discussion

The refined unit-cell parameters and atomic positions are listed in table 6-S1. We found no evidence of structural transitions up to 47 GPa (highest pressure achieved in our single crystal X-ray diffraction experiments) and we could refine structures at all pressures based on about 100 observed unique independent reflections with R1-factors better than 8 % (table S1). Distances between iron atoms and between iron and carbon decrease continuously with pressure (Fig. 6-1). To a first approximation the compressional behavior of Fe₃C can be described by a single isothermal third-order Birch-Murnaghan equation of state, giving for the entire studied pressure range a bulk modulus $K = 161(2)$ GPa and its first pressure derivative $K' = 5.9(2)$ (Fig. 6-1). However, the Birch normalized pressure (F_e) against Eulerian strain (f) plot (a more sensitive representation of the same data) shows a change in slope around 24 GPa, indicating a change in compressional behavior which may reflect specific changes in the electronic or magnetic state of Fe₃C. One of the best and most direct methods to elucidate the nature of the changes is Mössbauer spectroscopy.

Chapter 6 Structurally hidden magnetic transitions in Fe₃C

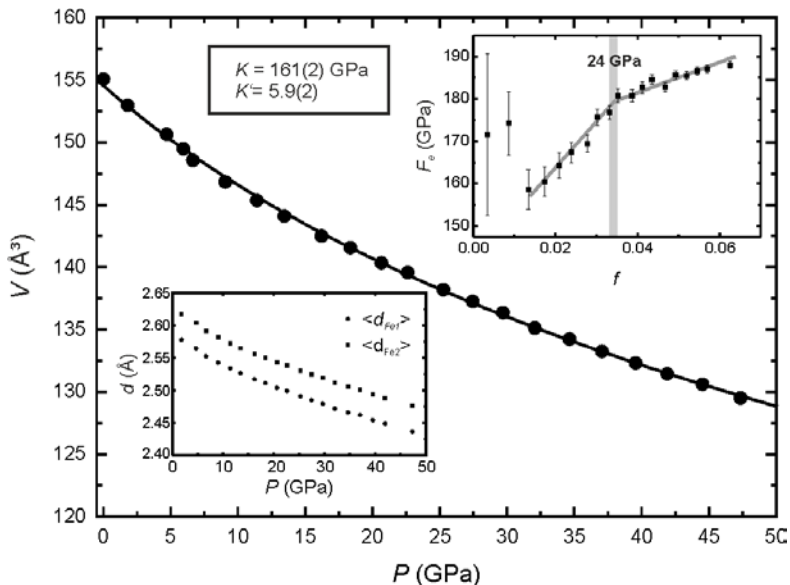


Figure 6-1 Volume-pressure data for Fe₃C with fitted 3rd order Birch Murnaghan equation of state. Upper insets shows a plot of the Eulerian strain (f) against Birch-normalized pressure (F_e). A change in compressional behavior is visible around 24 GPa. Lower inset shows the mean Fe-Fe of the separate iron sites distances to their coordinating iron atoms. Individual distances can be seen in Fig. 6-S4 and Fig. 6-S5.

Fe₃C has two non-equivalent Fe sites which results into two sextets with nearly equal magnetic hyperfine field (BHF) and central shift (CS) at room temperature (Le Caer et al., 1976) in the Mössbauer spectrum. However, the statistics of our data measured in a diamond anvil cell with a high non-resonant background level were only sufficient to fit the data with a single sextet. This is an acceptable approximation since the parameters of the two different sites are nearly equal (Le Caer et al., 1976). Selected spectra from the entire pressure range are shown in Fig. 6-2. The variation of BHF and CS with increasing pressure is shown in Fig. 6-3. BHF is generally proportional to the average Fe magnetic moment and it approaches zero at around 8 GPa, indicating that the net magnetic moment of the material is lost. Consequently the data were fitted to a doublet above this pressure. The FWHM of the doublet drops exponentially from pressures starting at 8 GPa to around 20 GPa and then the value stays constant up to 88 GPa (Fig. 6-S2).

The CS variation with pressure can be divided into 3 parts (Fig. 6-3). First, up to 8 GPa CS decreases linearly with increasing pressure. Second, from 8 to 22 GPa, CS shows a sharp increase followed by a more gradual decrease, where the maximum is situated around 10 GPa. Third, from 22 to 88 GPa CS decreases linearly but with a slope different to previous values. The anomalous behavior in the CS variation is also observed if the data at pressures above 8 GPa are fit to a sextet instead of a doublet. Therefore the jump is independent of the fitting model.

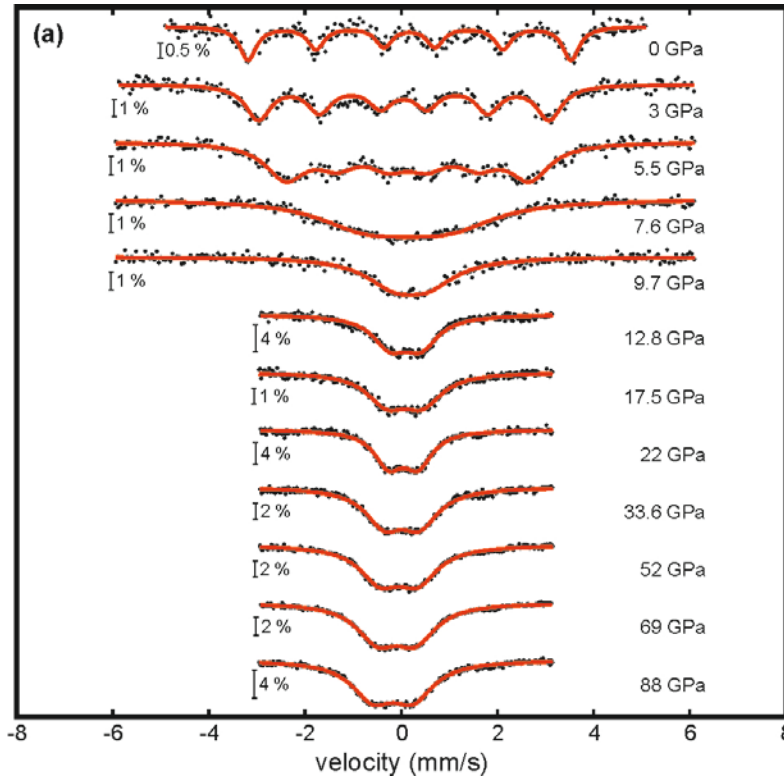


Figure 6-2 Selected ambient temperature Mössbauer spectra of Fe₃C over the whole pressure range studied.

The data show essentially two regions of discontinuity in the variation of hyperfine parameters with pressure: the first from 8 to 11 GPa and the second from 20 to 23 GPa. In the region from 8 to 11 GPa the loss of ferromagnetism in Fe₃C is observed as a decrease in BHF. Furthermore, the loss of BHF near 8 GPa is accompanied by an increase in CS. This parameter is influenced by two effects - the chemical isomer shift (which is a measure of *s*-electron density at the nucleus), and the second order Doppler shift (SOD, which is a measure of mean squared velocities of the Mössbauer active atoms). An increase in chemical isomer shift is contrary to the expected increase of *s*-electron density at the nucleus with increasing pressure, since the excited state of the ⁵⁷Fe nucleus is smaller than the ground state. Consequently the increase in CS can only be explained by a change in the SOD.

To estimate the contribution of the SOD to the CS, δ_{SOD} , we approximated the chemical isomer shift by fitting a straight line through the 3 lowermost pressure points (at 0, 1.95, and 4.5 GPa), and assumed that the remaining contribution to CS could be used to calculate the change in mean squared velocity $\langle v^2 \rangle$ due to the SOD. The variation in mean squared velocity can be calculated by $\Delta \langle v^2 \rangle = 2c \delta_{\text{SOD}}$ (Josephson, 1960), where *c* is the speed of light in vacuum. The result of this calculation suggests phonon softening in the region of the ferro- to paramagnetic transition (Fig. 6-S3). The maximum of this

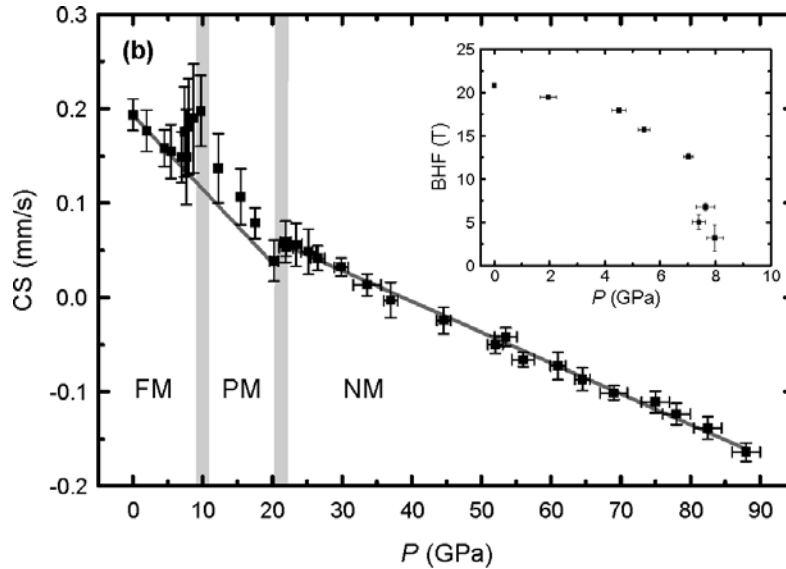


Figure 6-3 Variation of central shift (CS) (relative to α -Fe) of Fe₃C showing two transitions - ferromagnetic (FM) to paramagnetic (PM), and paramagnetic to non-magnetic (NM). Error bars of CS are shown as 2σ . Inset shows the variation of magnetic hyperfine field (BHF) of Fe₃C as a function of pressure at ambient temperature. Error bars of BHF are shown as 2σ .

curve is at 10 GPa, which is slightly higher than the pressure indicated by the rapidly decreasing BHF at around 8 GPa. The decrease of BHF before phonon softening occurs can be understood as the loss of long range order (which BHF is sensitive to) before the transition is complete at the local scale.

The interpretation of the transition in Fe₃C at around 10 GPa observed by Mössbauer spectroscopy as a transformation from the ferro- to paramagnetic state agrees with our structural results, i.e., the absence of any discontinuous changes in structure or compressional behavior. Indeed such ferro- to paramagnetic transitions in many metals (pure iron, for example) and compounds occur structurally unnoticed.

The second transition region around 22 GPa shows a small jump and a change in slope of CS variation as a function of pressure. The change in slope suggests a reconfiguration of the shielding electrons on iron atoms which affects the variation in CS with respect to pressure. According to our single crystal X-ray diffraction data and previously reported X-ray diffraction studies (Scott et al., 2001; Li et al., 2002; Ono and Mibe, 2010; Sata et al., 2010), there are no structural phase transitions up to at least 55 GPa. The jump can only be attributed to a spin transition of the iron atoms with a loss of magnetic moment (paramagnetic to non-magnetic transition). This conclusion is supported by XES studies which also suggest high-spin to low-spin crossover at 25 GPa (Lin et al., 2004).

Chapter 6 Structurally hidden magnetic transitions in Fe₃C

In ionic or covalent materials spin transitions are usually accompanied by a change of interatomic distance due to a decrease in the size of the atom. This results in a volume decrease, e.g., for CaFe₂O₄ and FeCO₃ there is a volume drop of 8.4 % (Merlini et al., 2009) and 10 % (Lavina et al., 2010), respectively. In metals the physical process is less clear; however spin transitions in metals are usually accompanied by structural phase transitions; e.g., in Fe a bcc-hcp transition (Cort et al., 1982; Ekman et al., 1998; Rueff et al., 1999; Klotz and Braden, 2000) and in Co a hcp-fcc transition (Yoo et al., 2000; Iota et al., 2007; Ishimatsu et al., 2011; Torchio et al., 2011). In Fe₃C we did not observe any structural changes at 22 GPa, but softening of the material on compression above this pressure is clearly visible on a f - F_e plot (Fig. 6-1). Thus, Fe₃C demonstrates that pressure-induced spin crossover is not always associated with first order structural transformations.

Theoretical *ab initio* calculations predict (Vocadlo et al., 2002) magnetic collapse at 60 GPa (at higher pressures than we observed) and a significant increase of bulk modulus in the non-magnetic phase (to $K_0 = 316$ GPa and $K' = 4.3$). In fact fitting our experimental data using a third-order Birch-Murnaghan equation of state for pressures below the spin transition (i.e., below 22 GPa) gives $K_0 = 145(3)$ GPa and $K' = 8.5(7)$, while the interval 22-47 GPa gives $K_0 = 172(1)$ GPa and $K' = 5.1(1)$. Thus our experimental observations reproduce at least qualitatively the increase in K_0 . However, the strong decrease of K' in our study results in an actual lattice softening at the pressure of the magnetic to non-magnetic transition in Fe₃C contrary to the theoretically predicted lattice stiffening.

6.5 Conclusion

Our combined single-crystal structural and Mössbauer spectroscopy studies of Fe₃C provide a reconciliation of previous conflicting reports. The ferro- to paramagnetic transition observed between 8 and 10 GPa corresponds to the transition observed in nuclear forward scattering (Gao et al., 2008) and XMCD (Duman et al., 2005) experiments, while observed changes in XES spectra (Lin et al., 2004) are consistent with the high-to-low spin transformation that we found at around 22 GPa. To our knowledge, this is the first study where pressure-induced phonon softening through a second order ferro- to paramagnetic phase transition is large enough to be resolved by a variation in CS with pressure.

6.6 Acknowledgements

The authors thank T. Boffa-Ballaran for providing help with the single-crystal diffraction analysis.

6.7 Supplementary information

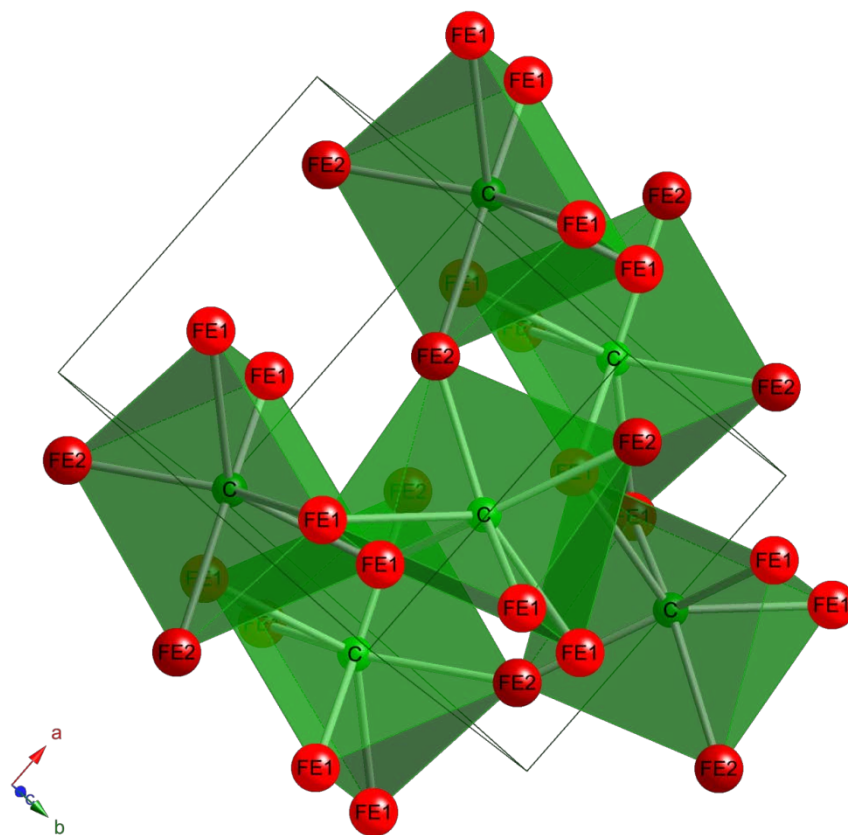


Figure 6-S1 Crystal structure of Fe₃C showing the trigonal prisms of Fe surrounding the carbon atoms. The two crystallographic positions of Fe are indicated.

Chapter 6 Structurally hidden magnetic transitions in Fe₃C

Table 6-S1 Results of single crystal X-ray diffraction refinement of Fe₃C at different pressures.

P (GPa)	R1 (%)	Lattice parameters				Atomic parameters (xyzU)
		a (Å)	b (Å)	c (Å)	V (Å ³)	
1.8(1)	6.3	4.501(1)	5.0726(8)	6.699(4)	152.98(7)	C 0.441(2) 0.876(2) 0.25 0.017(2) Fe1 0.3354(2) 0.1796(2) 0.0668(3) 0.0092(4) Fe2 0.8398(3) 0.0373(3) 0.25 0.0095(5)
4.7(1)	6.8	4.4785(5)	5.0468(8)	6.666(3)	150.65(8)	C 0.439(4) 0.871(3) 0.25 0.017(4) Fe1 0.3363(3) 0.1808(3) 0.0663(4) 0.0097(7) Fe2 0.8414(5) 0.0369(5) 0.25 0.0100(7)
6.7(2)	6.7	4.4568(4)	5.0210(8)	6.639(3)	148.56(6)	C 0.438(4) 0.871(3) 0.25 0.016(3) Fe1 0.3375(3) 0.1821(3) 0.0664(4) 0.0093(6) Fe2 0.8426(5) 0.0367(4) 0.25 0.0100(6)
9.1(1)	6.2	4.4377(4)	5.0034(7)	6.614(3)	146.85(7)	C 0.440(3) 0.873(3) 0.25 0.017(3) Fe1 0.3380(3) 0.1827(3) 0.0663(4) 0.0090(6) Fe2 0.8441(4) 0.0361(4) 0.25 0.0094(6)
11.4(1)	6.2	4.4209(4)	4.9875(8)	6.593(3)	145.36(8)	C 0.441(4) 0.872(4) 0.25 0.022(4) Fe1 0.3385(3) 0.1832(3) 0.0659(4) 0.0092(7) Fe2 0.8443(4) 0.0362(4) 0.25 0.0096(8)
13.4(2)	6.3	4.4073(4)	4.9738(8)	6.574(3)	144.10(8)	C 0.441(5) 0.870(4) 0.25 0.020(4) Fe1 0.3386(4) 0.1840(4) 0.0653(5) 0.0111(9) Fe2 0.8453(5) 0.0354(6) 0.25 0.012(1)
16.2(1)	6.4	4.3889(4)	4.9578(8)	6.549(3)	142.50(7)	C 0.442(4) 0.866(4) 0.25 0.021(4) Fe1 0.3391(3) 0.1837(3) 0.0655(4) 0.0084(7) Fe2 0.8460(4) 0.0356(4) 0.25 0.0090(8)
18.4(2)	6.4	4.3787(5)	4.9482(9)	6.534(4)	141.56(9)	C 0.439(5) 0.867(5) 0.25 0.025(5) Fe1 0.3396(3) 0.1842(4) 0.0653(5) 0.0100(8) Fe2 0.8463(5) 0.0352(5) 0.25 0.0105(9)
20.7(2)	6.4	4.3652(6)	4.935(1)	6.514(4)	140.34(9)	C 0.438(4) 0.867(4) 0.25 0.021(4) Fe1 0.3399(3) 0.1843(3) 0.0651(4) 0.0089(8) Fe2 0.8471(5) 0.0354(5) 0.25 0.0099(8)
22.6(1)	6.5	4.3558(6)	4.928(1)	6.502(5)	139.58(11)	C 0.438(5) 0.866(5) 0.25 0.029(6) Fe1 0.3404(4) 0.1841(4) 0.0649(5) 0.010(1) Fe2 0.8476(5) 0.0352(6) 0.25 0.010(1)
25.3(1)	8.2	4.3408(6)	4.912(1)	6.481(5)	138.20(8)	C 0.439(4) 0.872(4) 0.25 0.018(4) Fe1 0.3409(4) 0.1844(3) 0.0647(4) 0.0096(7) Fe2 0.8484(5) 0.0346(5) 0.25 0.0102(8)

Chapter 6 Structurally hidden magnetic transitions in Fe₃C

<i>P</i> (GPa)	<i>R</i> 1 (%)	<i>a</i> (Å)	<i>B</i> (Å)	<i>c</i> (Å)	<i>V</i> (Å ³)	Atomic parameters (<i>xyzU</i>)
27.5(2)	8.0	4.3305(7)	4.902(1)	6.465(5)	137.26(9)	C 0.443(4) 0.866(4) 0.25 0.023(4) Fe1 0.3413(4) 0.1846(4) 0.0649(4) 0.011(1) Fe2 0.8487(5) 0.0345(6) 0.25 0.012(1)
29.7(1)	8.0	4.3201(7)	4.892(1)	6.452(5)	136.37(9)	C 0.444(4) 0.870(4) 0.25 0.020(4) Fe1 0.3411(4) 0.1848(4) 0.0643(4) 0.0106(9) Fe2 0.8492(5) 0.0340(5) 0.25 0.012(1)
32.1(2)	5.8	4.3002(7)	4.877(1)	6.444(4)	135.14(4)	C 0.438(4) 0.869(4) 0.25 0.030(4) Fe1 0.3416(4) 0.1846(3) 0.0639(4) 0.0081(7) Fe2 0.8481(4) 0.0344(5) 0.25 0.0101(8)
34.7(2)	6.0	4.2890(8)	4.865(1)	6.433(4)	134.24(6)	C 0.428(6) 0.880(7) 0.25 0.034(6) Fe1 0.3426(4) 0.1847(4) 0.0637(5) 0.0099(7) Fe2 0.8489(6) 0.0345(5) 0.25 0.0107(7)
37.0(1)	6.4	4.2783(7)	4.855(1)	6.415(4)	133.25(7)	C 0.430(7) 0.870(8) 0.25 0.041(7) Fe1 0.3427(5) 0.1851(4) 0.0637(6) 0.0107(9) Fe2 0.8496(6) 0.0345(7) 0.25 0.011(1)
39.6(2)	6.6	4.2632(8)	4.849(2)	6.400(4)	132.31(5)	C 0.438(6) 0.873(6) 0.25 0.032(6) Fe1 0.3420(4) 0.1850(4) 0.0635(5) 0.0086(7) Fe2 0.8498(6) 0.0336(5) 0.25 0.0095(7)
41.9(1)	6.1	4.2528(9)	4.838(2)	6.388(4)	131.45(5)	C 0.434(6) 0.873(6) 0.25 0.031(6) Fe1 0.3426(4) 0.1849(4) 0.0632(5) 0.0090(7) Fe2 0.8507(6) 0.0333(5) 0.25 0.0097(7)
47.4(2)	7.5	4.226(1)	4.820(2)	6.357(6)	129.50(5)	C 0.435(8) 0.871(8) 0.25 0.042(8) Fe1 0.3428(5) 0.1857(5) 0.0629(6) 0.0107(9) Fe2 0.8509(7) 0.0328(7) 0.25 0.011(1)

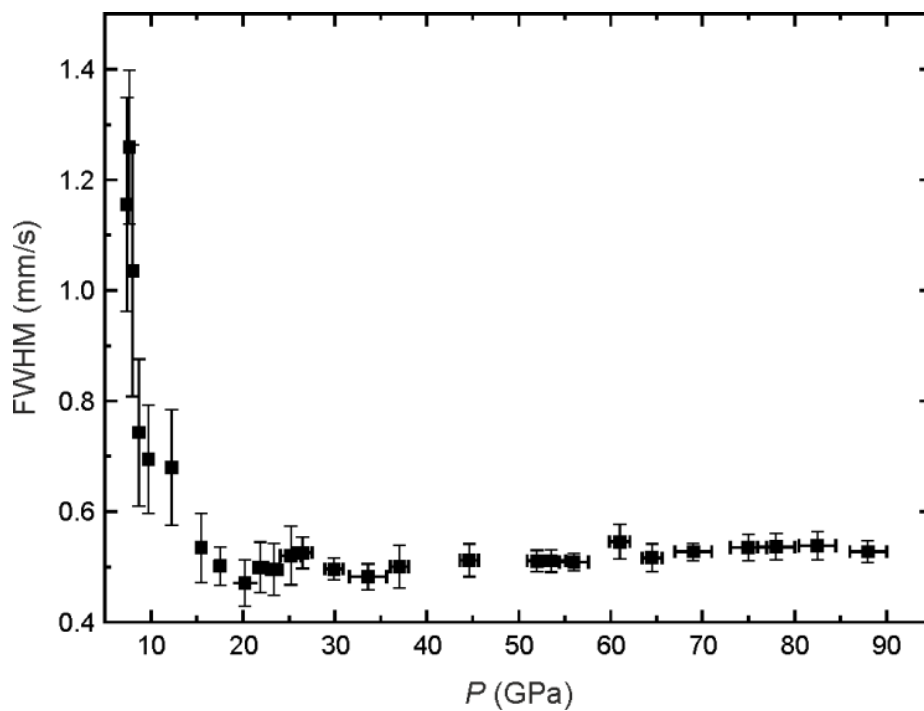


Figure 6-S2 Variation of the full width at half maximum of the Fe₃C doublet above the ferromagnetic to paramagnetic transition.

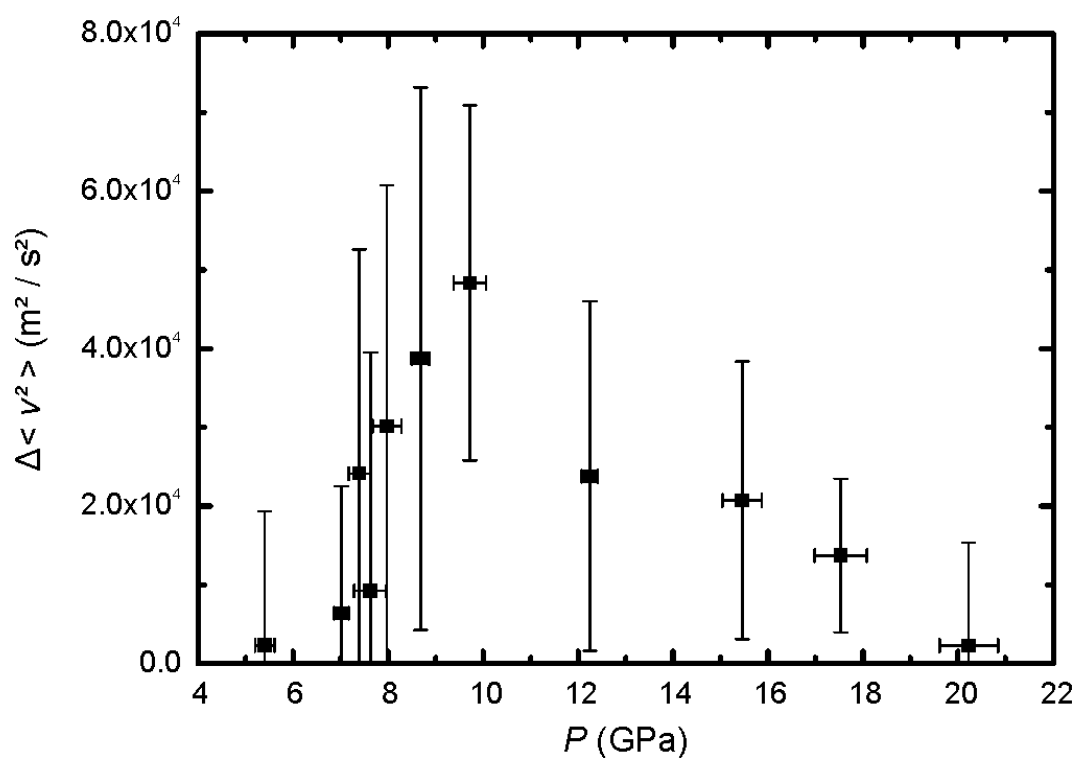


Figure 6-S3 Calculated changes in mean squared velocity of Fe₃C due to the ferromagnetic to paramagnetic transition.

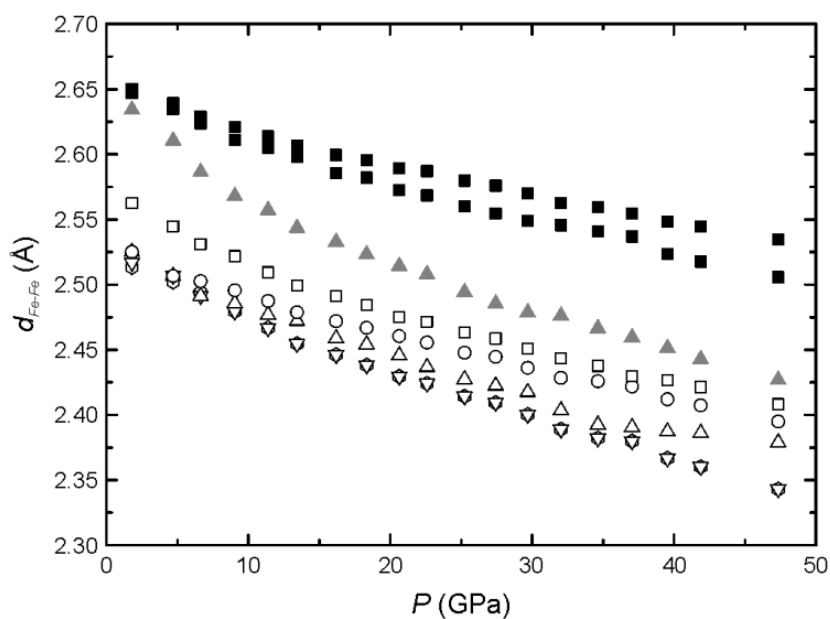


Figure 6-S4 Evolution of Fe-Fe distances in Fe₃C with pressure. Distances are divided into 3 groups according to their occurrence with respect to the structure-forming trigonal prisms around the carbon atom. (1) open symbols indicate distances in the basal planes of the trigonal prism, (2) solid black symbols indicate the height of the trigonal prism and (3) solid gray symbols indicate the distance between two non-connected trigonal prisms.

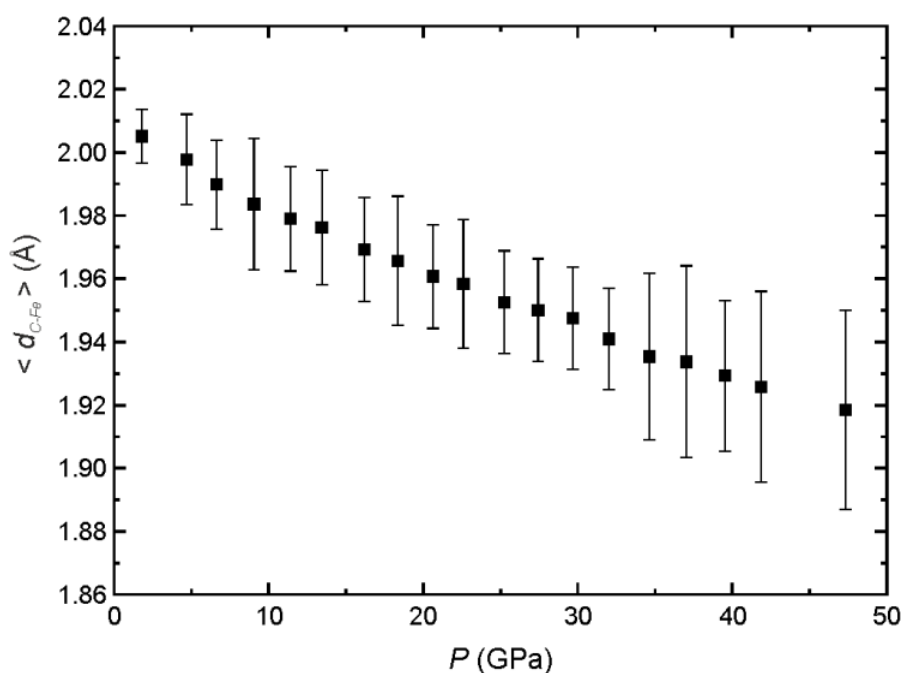


Figure 6-S5 Variation of mean carbon-iron distance with pressure. The mean is calculated from the distances to the individual iron atoms surrounding carbon in the trigonal prism.

7 References

- Acet, M., Gehrmann, B., Wassermann, E.F., Bach, H., Pepperhoff, W., 2001. Relevance of magnetic instabilities to the properties of interstitial solid solutions and compounds of Fe. *J. Magn. Magn. Mater.* 232, 221–230.
- Agee, C.B., Walker, D., 1988. Static Compression and Olivine Flotation in Ultrabasic Silicate Liquid. *J. Geophys. Res.* 93, 3437–3449.
- Agnor, C.B., Canup, R.M., Levison, H.F., 1999. On the Character and Consequences of Large Impacts in the Late Stage of Terrestrial Planet Formation. *Icarus* 142, 219–237.
- van Aken, P. a., Liebscher, B., 2002. Quantification of ferrous/ferric ratios in minerals: new evaluation schemes of Fe L_{23} electron energy-loss near-edge spectra. *Phys. Chem. Miner.* 29, 188–200.
- Allègre, C.J., Poirier, J.-P., Humler, E., Hofmann, A.W., 1995. The chemical composition of the Earth. *Earth Planet. Sci. Lett.* 134, 515–526.
- Anderson, O.L., Isaak, D.G., 2002. Another look at the core density deficit of Earth's outer core. *Phys. Earth Planet. In.* 131, 19–27.
- Andraut, D., Petitgirard, S., N, Nigro, G.L., Devidal, J.-L., Veronesi, G., Garbarino, G., Mezouar, M., 2012. Solid–liquid iron partitioning in Earth's deep mantle. *Nature* 487, 354–357.
- Auzende, A.-L., Badro, J., Ryerson, F.J., Weber, P.K., Fallon, S.J., Addad, A., Siebert, J., Fiquet, G., 2008. Element partitioning between magnesium silicate perovskite and ferropericlase: New insights into bulk lower-mantle geochemistry. *Earth Planet. Sci. Lett.* 269, 164–174.
- Azevedo, M.M.P. de, Rogalski, M.S., Sousa, J.B., 1997. A user-friendly PC program for evaluation of Mössbauer spectra. *Meas. Sci. Technol.* 8, 941–946.
- Badro, J., Fiquet, G., Guyot, F., Rueff, J.-P., Struzhkin, V.V., Vankó, G., Monaco, G., 2003a. Iron partitioning in Earth's mantle: toward a deep lower mantle discontinuity. *Science* 300, 789–91.
- Badro, J., Fiquet, G., Guyot, F., Rueff, J.-P., Struzhkin, V.V., Vankó, G., Monaco, G., 2003b. Iron partitioning in Earth's mantle: toward a deep lower mantle discontinuity. *Science* 300, 789–91.
- Badro, J., Rueff, J.-P., Vankó, G., Monaco, G., Fiquet, G., Guyot, F., 2004. Electronic transitions in perovskite: possible nonconvecting layers in the lower mantle. *Science* 305, 383–6.
- Bassett, W.A., Weathers, M., 1986. Temperature measurement in laser heated diamond anvil cells. *Physica B+C* 139-140, 900–902.
- Brand, R.A., 1995. Normos-90 Mössbauer fitting program package. *Angewandte Physik*, Univ. Duisburg, Germany.
- Burns, R.G., 1993. *Mineralogical applications of crystal field theory*. Cambridge University Press, Cambridge, UK.

Chapter 7 References

- Le Caer, G., Dubois, J.M.M., Senateur, J.P., 1976. Etude par spectrométrie Mössbauer des carbures de fer Fe_3C et Fe_5C_2 . *J. Solid State Chem.* 19, 19–28.
- Cappellen, E.V., Doukhan, J.C., 1994. Quantitative transmission X-ray microanalysis of ionic compounds. *Ultramicroscopy* 53, 343–349.
- Catalli, K., Shim, S.-H., Dera, P., Prakapenka, V.B., Zhao, J., Sturhahn, W., Chow, P., Xiao, Y., Cynn, H., Evans, W.J., 2011. Effects of the Fe^{3+} spin transition on the properties of aluminous perovskite—New insights for lower-mantle seismic heterogeneities. *Earth Planet. Sci. Lett.* 310, 293–302.
- Catalli, K., Shim, S.-H., Prakapenka, V.B., Zhao, J., Sturhahn, W., Chow, P., Xiao, Y., Liu, H., Cynn, H., Evans, W.J., 2010. Spin state of ferric iron in MgSiO_3 perovskite and its effect on elastic properties. *Earth Planet. Sci. Lett.* 289, 68–75.
- Chandra Shekar, N.V., Sahu, P.C., Govinda Rajan, K., 2003. Laser-heated diamond-anvil cell (LHDAC) in Materials Science Research. *J. Mater. Sci. Technol.* 6, 518–525.
- Cort, G., Taylor, R.D., Willis, J.O., 1982. Search for magnetism in hcp ϵ -Fe. *J. Appl. Phys.* 53, 2064.
- Dubrovinskaia, N., Dubrovinsky, L., 2003. Whole-cell heater for the diamond anvil cell. *Rev. Sci. Instrum.* 74, 3433.
- Dubrovinsky, L., Boffa-Ballaran, T., Glazyrin, K., Kurnosov, A., Frost, D., Merlini, M., Hanfland, M., Prakapenka, V.B., Schouwink, P., Pippinger, T., Dubrovinskaia, N., 2010a. Single-crystal X-ray diffraction at megabar pressures and temperatures of thousands of degrees. *High Pressure Res.* 30, 620–633.
- Dubrovinsky, L., Boffa-Ballaran, T., Glazyrin, K., Kurnosov, A., Frost, D., Merlini, M., Hanfland, M., Prakapenka, V.B., Schouwink, P., Pippinger, T., Dubrovinskaia, N., 2010b. Single-crystal X-ray diffraction at megabar pressures and temperatures of thousands of degrees. *High Pressure Res.* 30, 620–633.
- Dubrovinsky, L., Glazyrin, K., McCammon, C., Narygina, O., Greenberg, E., Ubelhack, S., Chumakov, a I., Pascarelli, S., Prakapenka, V., Bock, J., Dubrovinskaia, N., 2009. Portable laser-heating system for diamond anvil cells. *J. Synchrotron Radiat.* 16, 737–41.
- Dubrovinsky, L., Saxena, S., Tutti, F., Rekhi, S., LeBehan, T., 2000. In situ X-Ray study of thermal expansion and phase transition of iron at multimegabar pressure. *Phys. Rev. Lett.* 84, 1720–3.
- Duman, E., Acet, M., Wassermann, E., Itié, J., Baudalet, F., Mathon, O., Pascarelli, S., 2005. Magnetic Instabilities in Fe_3C Cementite Particles Observed with Fe K-Edge X-Ray Circular Dichroism under Pressure. *Phys. Rev. Lett.* 94, 3–6.
- Dyar, M.D., 1985. A review of Mössbauer data on inorganic glasses: the effects of composition on iron valency and coordination. *Am. Mineral.* 70, 304–316.
- Dziewonski, A.M., Anderson, D.L., 1981. Preliminary reference Earth model. *Phys. Earth Planet. In.* 25, 297–356.
- Egerton, R.F., 1996. *Electron Energy Loss Spectroscopy in the Electron Microscope*, 2nd edn. ed. New York.

Chapter 7 References

- Ekman, M., Sadigh, B., Einarsdotter, K., Blaha, P., 1998. Ab initio study of the martensitic bcc-hcp transformation in iron. *Phys. Rev. B* 58, 5296–5304.
- Fei, Y., Ricolleau, A., Frank, M., Mibe, K., Shen, G., Prakapenka, V., 2007. Toward an internally consistent pressure scale. *Proc. Natl. Acad. Sci. U. S. A.* 104, 9182–6.
- Fiquet, G., Badro, J., Gregoryanz, E., Fei, Y., Occelli, F., 2009. Sound velocity in iron carbide (Fe_3C) at high pressure: Implications for the carbon content of the Earth's inner core. *Phys. Earth Planet. In.* 172, 125–129.
- Frost, D.J., 2008. The upper mantle and transition zone. *Elements* 4, 171–176.
- Frost, D.J., Langenhorst, F., 2002. The effect of Al_2O_3 on Fe-Mg partitioning between magnesiowüstite and magnesium silicate perovskite. *Earth Planet. Sci. Lett.* 199.
- Frost, D.J., Liebske, C., Langenhorst, F., McCammon, C.A., Tronnes, R.G., Rubie, D.C., 2004. Experimental evidence for the existence of iron-rich metal in the Earth's lower mantle. *Nature* 409–412.
- Fujino, K., Nishio-Hamane, D., Seto, Y., Sata, N., Nagai, T., Shinmei, T., Irifune, T., Ishii, H., Hiraoka, N., Cai, Y.Q., Tsuei, K.-D., 2012. Spin transition of ferric iron in Al-bearing Mg-perovskite up to 200 GPa and its implication for the lower mantle. *Earth Planet. Sci. Lett.* 317–318, 407–412.
- Funamori, N., Sato, T., 2010. Density contrast between silicate melts and crystals in the deep mantle: An integrated view based on static-compression data. *Earth Planet. Sci. Lett.* 295, 435–440.
- Gao, L., Chen, B., Wang, J., Alp, E.E., Zhao, J., Lerche, M., Sturhahn, W., Scott, H.P., Huang, F., Ding, Y., Sinogeikin, S.V., Lundstrom, C.C., Bass, J.D., Li, J., 2008. Pressure-induced magnetic transition and sound velocities of Fe_3C : Implications for carbon in the Earth's inner core. *Geophys. Res. Lett.* 35, 1–5.
- Glazyrin, K., Boffa-Ballaran, T., Frost, D.J., McCammon, C.A., Kantor, A., Merlini, M., Hanfland, M., Dubrovinsky, L., n.d. Effect of iron oxidation state on the bulk sound velocity of the Earth's lower mantle. *Nat. Geosci.* submitted.
- Goncharov, A.F., Beck, P., Struzhkin, V.V., Haugen, B.D., Jacobsen, S.D., 2009. Thermal conductivity of lower-mantle minerals. *Phys. Earth Planet. In.* 174, 24–32.
- Goncharov, A.F., Prakapenka, V.B., Struzhkin, V.V., Kantor, I., Rivers, M.L., Dalton, D.A., 2010. X-ray diffraction in the pulsed laser heated diamond anvil cell. *Rev. Sci. Instrum.* 81, 113902.
- Goncharov, A.F., Struzhkin, V.V., Montoya, J. a., Kharlamova, S., Kundargi, R., Siebert, J., Badro, J., Antonangeli, D., Ryerson, F.J., Mao, W., 2010. Effect of composition, structure, and spin state on the thermal conductivity of the Earth's lower mantle. *Phys. Earth Planet. In.* 180, 148–153.
- Greenwood, N.N., Gibb, T.C., 1971. Mössbauer spectroscopy. Chapman and Hall Ltd., London.
- Große, G., 1993. PC-Mos II v1.0, Fast Comtec. Oberhaching, Germany.
- Hammersley, A.P., 1997. FIT2D: An introduction and overview. ESRF Internal Report unpubl.

Chapter 7 References

- Hearne, G., Pasternak, M., Taylor, R., Lacorre, P., 1995. Electronic structure and magnetic properties of LaFeO₃ at high pressure. *Phys. Rev. B* 51, 11495–11500.
- van der Hilst, R.D., 1999. Compositional Heterogeneity in the bottom 1000 kilometers of Earth's mantle: Toward a hybrid convection model. *Science* 283, 1885–1888.
- Hitoshi, K., Fenglin, N., 1994. Seismic evidence for a 920-km discontinuity in the mantle. *Nature* 371, 301–305.
- Hjølsum, J. í, Madsen, M.B., 2009. Fit;o) - A Mössbauer spectrum fitting program. arXiv:0912.0449v1 [physics.comp-ph] 23.
- Hsu, H., Blaha, P., Cococcioni, M., Wentzcovitch, R.M., 2011. Spin-State Crossover and Hyperfine Interactions of Ferric Iron in MgSiO₃ Perovskite. *Phys. Rev. Lett.* 106, 1–4.
- Hsu, H., Umemoto, K., Blaha, P., Wentzcovitch, R.M., 2010. Spin states and hyperfine interactions of iron in (Mg,Fe)SiO₃ perovskite under pressure. *Earth Planet. Sci. Lett.* 294, 19–26.
- Ingalls, R., 1964. Electric-Field Gradient Tensor in Ferrous Compounds. *Phys. Rev.* 133, A787–A793.
- Iota, V., Klepeis, J.-H.P., Yoo, C.-S., Lang, J., Haskel, D., Srajer, G., 2007. Electronic structure and magnetism in compressed 3d transition metals. *Appl. Phys. Lett.* 90, 042505.
- Irifune, T., Shinmei, T., McCammon, C. a, Miyajima, N., Rubie, D.C., Frost, D.J., 2010. Iron partitioning and density changes of pyrolite in Earth's lower mantle. *Science* 327, 193–5.
- Ishimatsu, N., Kawamura, N., Maruyama, H., Mizumaki, M., Matsuoka, T., Yumoto, H., Ohashi, H., Suzuki, M., 2011. Paramagnetism with anomalously large magnetic susceptibility in β (fcc)-cobalt probed by x-ray magnetic circular dichroism up to 170 GPa. *Phys. Rev. B* 83, 1–4.
- Ito, E., Takahashi, E., 1989. Postspinel transformations in the system Mg₂SiO₄-Fe₂SiO₄ and some geophysical implications. *J. Geophys. Res.* 94, 10637–10646.
- Jackson, J.M., Sturhahn, W., Shen, G., Zhao, J., Hu, M.Y., Errandonea, D., Bass, J.D., Fei, Y., 2005. A synchrotron Mössbauer spectroscopy study of (Mg,Fe)SiO₃ perovskite up to 120 GPa. *Am. Mineral.* 90, 199–205.
- Jephcoat, A.P., Olson, P., 1987. Is the inner core of the Earth pure iron? *Nature* 322, 332–335.
- Josephson, B.D., 1960. Temperature-dependent shift of gamma rays emitted by a solid. *Phys. Rev. Lett.* 4, 341–342.
- Kaneshima, S., 1999. Dipping low-velocity layer in the mid-lower mantle: Evidence for geochemical heterogeneity. *Science* 283, 1888–1892.
- Kantor, I., Dubrovinsky, L., McCammon, C., Steinle-Neumann, G., Kantor, a., Skorodumova, N., Pascarelli, S., Aquilanti, G., 2009. Short-range order and Fe clustering in Mg_{1-x}Fe_xO under high pressure. *Phys. Rev. B* 80, 1–12.
- Kent, T.A., 1998. WMoss v2.5.

Chapter 7 References

- Keppler, H., Frost, D. j., 2005. Mineral behavior at extreme conditions, in: Miletich, R. (Ed.), Vol. 7 EMU Notes in Mineralogy. Eötvös University Press, pp. 1–30.
- Keppler, H., Rubie, D.C., 1993. Pressure-induced coordination changes of transition-metal ions in silicate melts. *Nature* 364, 54–56.
- Kesson, S., Gerald, J.D.F., O'Neill, H.S.C., Shelley, J.M.G., 2002. Partitioning of iron between magnesian silicate perovskite and magnesiowüstite at about 1 Mbar. *Phys. Earth Planet. In.* 131, 295–310.
- Klotz, S., Braden, M., 2000. Phonon dispersion of bcc iron to 10 GPa. *Phys. Rev. Lett.* 85, 3209–3212.
- Kurnosov, A., Kantor, I., Boffa-Ballaran, T., Lindhardt, S., Dubrovinsky, L., Kuznetsov, A., Zehnder, B.H., 2008. A novel gas-loading system for mechanically closing of various types of diamond anvil cells. *Rev. Sci. Instrum.* 79, 045110.
- Kuznetsov, A.Y., 2007. In-situ combined X-ray diffraction and electrical resistance measurements at high pressures and temperatures in diamond anvil cells. *High Pressure Res.* 27, 213–222.
- Lagarec, K., Rancourt, D., 1997. Extended Voigt-based analytic lineshape method for determining N-dimensional correlated hyperfine parameter distributions in Mössbauer spectroscopy. *Nucl. Instrum. Meth. B* 129, 266–280.
- Lagarec, K., Rancourt, D.G., 1998. Recoil, Mössbauer spectral analysis software for windows. Version 1.0.
- Larson, A.C., Von Dreele, R.B., 2004. General structure analysis system (GSAS). Los Alamos National Laboratory Report LAUR 86, 748.
- Lauterbach, S., McCammon, C.A., van Aken, P., Langenhorst, F., Seifert, F., 2000. Mössbauer and ELNES spectroscopy of (Mg,Fe)(Si,Al)O₃ perovskite: a highly oxidized component of the lower mantle. *Contrib. Mineral. Petrol.* 17–26.
- Lavina, B., Dera, P., Downs, R., Yang, W., Sinogeikin, S., Meng, Y., Shen, G., Schiferl, D., 2010. Structure of siderite FeCO₃ to 56 GPa and hysteresis of its spin-pairing transition. *Phys. Rev. B* 82, 1–7.
- Lay, T., Garnero, E.J., Williams, Q., 2004. Partial melting in a thermo-chemical boundary layer at the base of the mantle. *Phys. Earth Planet. In.* 146, 441–467.
- Lee, S.K., Lin, J., Cai, Y.Q., Hiraoka, N., Eng, P.J., Okuchi, T., Mao, H., 2008. X-ray Raman scattering study of MgSiO₃ glass at high pressure: Implication for triclustered MgSiO₃ melt in Earth's mantle. *Proc. Natl. Acad. Sci. U. S. A.* 105, 7925–7929.
- Li, J., Mao, H.K., Fei, Y., Gregoryanz, E., Eremets, M., Zha, C.S., 2002. Compression of Fe₃C to 30 GPa at room temperature. *Phys. Chem. Miner.* 29, 166–169.
- Lin, J., Weir, S.T., Jackson, D.D., Evans, W.J., Vohra, Y.K., Qiu, W., Yoo, C., 2007. Electrical conductivity of the lower-mantle ferropericlase across the electronic spin transition. *Geophys. Res. Lett.* 34, L16305.

Chapter 7 References

- Lin, J.-F., Fukui, H., Prendergast, D., Okuchi, T., Cai, Y., Hiraoka, N., Yoo, C.-S., Trave, A., Eng, P., Hu, M., Chow, P., 2007. Electronic bonding transition in compressed SiO₂ glass. *Phys. Rev. B* 75, 1–4.
- Lin, J.-F., Gavriluk, A., Struzhkin, V., Jacobsen, S., Sturhahn, W., Hu, M., Chow, P., Yoo, C.-S., 2006. Pressure-induced electronic spin transition of iron in magnesiowüstite-(Mg,Fe)O. *Phys. Rev. B* 73, 73–76.
- Lin, J.-F., Struzhkin, V., Mao, H., Hemley, R., Chow, P., Hu, M., Li, J., 2004. Magnetic transition in compressed Fe₃C from x-ray emission spectroscopy. *Phys. Rev. B* 70, 1–4.
- Lin, J.-F., Struzhkin, V.V., Jacobsen, S.D., Hu, M.Y., Chow, P., Kung, J., Liu, H., Mao, H.-K., Hemley, R.J., 2005. Spin transition of iron in magnesiowüstite in the Earth's lower mantle. *Nature* 436, 377–80.
- Lin, J.-F., Vankó, G., Jacobsen, S.D., Iota, V., Struzhkin, V.V., Prakapenka, V.B., Kuznetsov, A., Yoo, C.-S., 2007. Spin transition zone in Earth's lower mantle. *Science* 317, 1740–3.
- Lin, J.-F., Watson, H., Vankó, G., Alp, E.E., Prakapenka, V.B., Dera, P., Struzhkin, V.V., Kubo, A., Zhao, J., McCammon, C., Evans, W.J., 2008. Intermediate-spin ferrous iron in lowermost mantle post-perovskite and perovskite. *Nat. Geosci.* 1, 688–691.
- Lin, J.-F., Wheat, A., 2011. Electronic spin transition of iron in the Earth's lower mantle. *Hyperfine Interact.* 207, 81–88.
- Mao, H.K., Xu, J., Bell, P.M., 1986. Calibration of the ruby pressure gauge to 800 kbar under quasi-hydrostatic conditions. *J. Geophys. Res.* 91, 4673–4676.
- Mao, Z., Lin, J.-F., Liu, J., Prakapenka, V.B., 2011. Thermal equation of state of lower-mantle ferropervicite across the spin crossover. *Geophys. Res. Lett.* 38, 2–5.
- McCammon, C., 1994. A Mössbauer milliprobe: Practical considerations. *Hyperfine Interact.* 92, 1235–1239.
- McCammon, C., 1997. Perovskite as a possible sink for ferric iron in the lower mantle. *Nature* 387, 694–696.
- McCammon, C., Dubrovinsky, L., Narygina, O., Kantor, I., Wu, X., Glazyrin, K., Sergueev, I., Chumakov, A.I., 2010. Low-spin Fe²⁺ in silicate perovskite and a possible layer at the base of the lower mantle. *Phys. Earth Planet. In.* 180, 215–221.
- McCammon, C., Kantor, I., Narygina, O., Rouquette, J., Ponkratz, U., Sergueev, I., Mezouar, M., Prakapenka, V., Dubrovinsky, L., 2008. Stable intermediate-spin ferrous iron in lower-mantle perovskite. *Nat. Geosci.* 1, 684–687.
- McCammon, C.A., 2000. Insights into phase transformations from Mössbauer spectroscopy. *Rev. Mineral. Geochem.* 39, 241–264.
- McCammon, C.A., Lauterbach, S., Seifert, F., Langenhorst, F., van Aken, P.A., 2004. Iron oxidation state in lower mantle mineral assemblages I. Empirical relations derived from high-pressure experiments. *Earth Planet. Sci. Lett.* 222, 435–449.
- McDonough, W.F., Sun, S. -s., 1995. The composition of the Earth. *Chem. Geol.* 2541, 223–253.

Chapter 7 References

- McSween, H.Y., 1999. Meteorites and their parent planets. Cambridge Univ. Press, Cambridge, NY.
- Mccammon, C., 2005. The paradox of mantle redox. *Science* 307, 807–808.
- Merlini, M., Hanfland, M., Gemmi, M., Huotari, S., Simonelli, L., Strobel, P., 2009. Fe³⁺ spin transition in CaFe₂O₄ at high pressure. *Am. Mineral.* 95, 200–203.
- Miller, G.H., Stolper, E.M., Ahrens, T.J., 1991. The equation of state of a molten Komatiite: Shock wave compression to 36 GPa. *J. Geophys. Res.* 96, 11831–11848.
- Murakami, M., Bass, J.D., 2010. Spectroscopic evidence for ultrahigh-pressure polymorphism in SiO₂. *Glass. Phys. Rev. Lett.* 104, 1–4.
- Murakami, M., Bass, J.D., 2011. Evidence of denser MgSiO₃ glass above 133 gigapascal (GPa) and implications for remnants of ultradense silicate melt from a deep magma ocean. *Proc. Natl. Acad. Sci. U. S. A.* 108, 17286–9.
- Murakami, M., Hirose, K., Kawamura, K., Sata, N., Ohishi, Y., 2004. Post-perovskite phase transition in MgSiO₃. *Science* 304, 855–8.
- Murakami, M., Hirose, K., Sata, N., Ohishi, Y., 2005. Post-perovskite phase transition and mineral chemistry in the pyrolitic lowermost mantle. *Geophys. Res. Lett.* 32, L03304.
- Nakajima, Y., Frost, D.J., Rubie, D.C., 2012. Ferrous iron partitioning between magnesium silicate perovskite and ferropericlase and the composition of perovskite in the Earth's lower mantle. *J. Geophys. Res.* 117, 1–12.
- Narygina, O., Dubrovinsky, L.S., Samuel, H., McCammon, C. a., Kantor, I.Y., Glazyrin, K., Pascarelli, S., Aquilanti, G., Prakapenka, V.B., 2011. Chemically homogeneous spin transition zone in Earth's lower mantle. *Phys. Earth Planet. In.* 185, 107–111.
- Narygina, O., Mattesini, M., Kantor, I., Pascarelli, S., Wu, X., Aquilanti, G., McCammon, C., Dubrovinsky, L., 2009. High-pressure experimental and computational XANES studies of (Mg,Fe)(Si,Al)O₃ perovskite and (Mg,Fe)O ferropericlase as in the Earth's lower mantle. *Phys. Rev. B* 79, 1–10.
- Nomura, R., Ozawa, H., Tateno, S., Hirose, K., Hernlund, J., Muto, S., Ishii, H., Hiraoka, N., 2011. Spin crossover and iron-rich silicate melt in the Earth's deep mantle. *Nature* 473, 199–202.
- Ohta, K., Hirose, K., Ichiki, M., Shimizu, K., Sata, N., Ohishi, Y., 2010. Electrical conductivities of pyrolitic mantle and MORB materials up to the lowermost mantle conditions. *Earth Planet. Sci. Lett.* 289, 497–502.
- Ohta, K., Hirose, K., Onoda, S., Shimizu, K., 2007. The effect of iron spin transition on electrical conductivity of (Mg,Fe)O magnesiowüstite. *Proc. Jpn. Acad., Ser. B* 83, 97–100.
- Ohta, K., Hirose, K., Shimizu, K., Sata, N., Ohishi, Y., 2010. The electrical resistance measurements of (Mg,Fe)SiO₃ perovskite at high pressures and implications for electronic spin transition of iron. *Phys. Earth Planet. In.* 180, 154–158.
- Ohta, K., Onoda, S., Hirose, K., Sinmyo, R., Shimizu, K., Sata, N., Ohishi, Y., Yasuhara, A., 2008. The electrical conductivity of post-perovskite in Earth's D'' layer. *Science* 320, 89–91.

Chapter 7 References

- Ohtani, E., Maeda, M., 2001. Density of basaltic melt at high pressure and stability of the melt at the base of the lower mantle. *Earth Planet. Sci. Lett.* 193, 69–75.
- Ono, S., Mibe, K., 2010. Magnetic transition of iron carbide at high pressures. *Phys. Earth Planet. In.* 180, 1–6.
- Pasternak, M.P., Xu, W.M., Rozenberg, G.K.H., Taylor, R.D., 2002. Electronic, magnetic and structural properties of the $RFeO_3$ antiferromagnetic-perovskites at very high pressures. *Mater. Res. Soc. Symp. Proc.* 718, 1–10.
- Potapkin, V., Chumakov, A.I., Smirnov, G.V., Celse, J.P., Ruffer, R., McCammon, C., Dubrovinsky, L., 2012. The ^{57}Fe synchrotron Mössbauer source at the ESRF. *J. Synchrotron Radiat.* 19, 559–69.
- Prescher, C., McCammon, C., Dubrovinsky, L., 2012. MossA - a program for analyzing energy-domain Mössbauer spectra from conventional and synchrotron sources. *J. Appl. Crystallogr.* 45, 329–331.
- Rigden, S.M., Ahrens, T.J., Stolper, E.M., 1984. Densities of liquid silicates at high pressures. *Science* 226, 1071–4.
- Ringwood, A.E., 1991. Phase transformations and their bearing on the constitution and dynamics of the mantle. *Geochim. Cosmochim. Acta* 55, 2083–2110.
- Rouquette, J., Kantor, I., Mccammon, C.A., Dmitriev, V., Dubrovinsky, L.S., 2008. High-Pressure Studies of $(\text{Mg}_{0.9}\text{Fe}_{0.1})_2\text{SiO}_4$ Olivine Using Raman Spectroscopy, X-ray Diffraction, and Mössbauer Spectroscopy. *Inorg. Chem.* 47, 2668–2673.
- Rueff, J.P., Krisch, M., Cai, Y.Q., Kaprolat, A., Hanfland, M., Lorenzen, M., Masciovecchio, C., Verbeni, R., Sette, F., 1999. Magnetic and structural alpha-epsilon phase transition in Fe monitored by X-ray emission spectroscopy. *Phys. Rev. B* 60, 510–512.
- Ruffer, R., Chumakov, A.I., 1996. Nuclear resonance beamline at ESRF. *Hyperfine Interact.* 97-98, 589–604.
- Sakai, T., Ohtani, E., Terasaki, H., Sawada, N., Kobayashi, Y., Miyahara, M., Nishijima, M., Hirao, N., Ohishi, Y., Kikegawa, T., 2009. Fe-Mg partitioning between perovskite and ferropericline in the lower mantle. *Am. Mineral.* 94, 921–925.
- Sarkisyan, V.A., Troyan, I.A., Lyubutin, I.S., Gavrilyuk, A.G., Kashuba, A.F., 2002. Magnetic collapse and the change of electronic structure of FeBO_3 antiferromagnet under high pressure. *JETP Lett* 76, 788–793.
- Sata, N., Hirose, K., Shen, G., Nakajima, Y., Ohishi, Y., Hirao, N., 2010. Compression of FeSi , Fe_3C , $\text{Fe}_{0.95}\text{O}$, and FeS under the core pressures and implication for light element in the Earth's core. *Radiat. Res.* 115, 1–13.
- Sato, T., Funamori, N., 2008. Sixfold-Coordinated Amorphous Polymorph of SiO_2 under High Pressure. *Phys. Rev. Lett.* 101, 1–4.
- Scott, H.P., Williams, Q., Knittle, E., 2001. Stability and equation of state of Fe_3C to 73 GPa: Implications for carbon in the Earth's core. *Geophys. Res. Lett.* 28, 1875–1878.

Chapter 7 References

- Shearer, P., Masters, G., 1990. The density and shear velocity contrast at the inner core boundary. *Geophys. J. Int.* 102, 491–498.
- Sheldrick, G.M., 2008. A short history of SHELX. *Acta Crystallogr. A* 64, 112–22.
- Sinmyo, R., Hirose, K., Muto, S., Ohishi, Y., Yasuhara, A., 2011. The valence state and partitioning of iron in the Earth's lowermost mantle. *J. Geophys. Res.* B 116, B07205.
- Sinmyo, R., Hirose, K., Nishio-Hamane, D., Seto, Y., Fujino, K., Sata, N., Ohishi, Y., 2008. Partitioning of iron between perovskite/postperovskite and ferroperriclinite in the lower mantle. *J. Geophys. Res.* 113, 1–11.
- Smirnov, G.V., van Buerck, U., Chumakov, A.I., Baron, A.Q.R., Rüffer, R., 1997. Synchrotron Mössbauer source. *Phys. Rev. B* 55, 5811–5815.
- Smirnov, G.V., Chumakov, A.I., Potapkin, V.B., Rüffer, R., Popov, S.L., 2011. Multispace quantum interference in a ^{57}Fe synchrotron Mössbauer source. *Phys. Rev. A* 84, 053851.
- Stackhouse, S., Brodholt, J.P., Price, G.D., 2007. Electronic spin transitions in iron-bearing MgSiO_3 perovskite. *Earth Planet. Sci. Lett.* 253, 282–290.
- Stevenson, D.J., 1981. Models of the Earth's Core. *Science* 214, 611–619.
- Stixrude, L., Karki, B., 2005. Structure and freezing of MgSiO_3 liquid in Earth's lower mantle. *Science* 310, 297–9.
- Stixrude, L., Lithgow-Bertelloni, C., 2005. Thermodynamics of mantle minerals - I. Physical properties. *Geophys. J. Int.* 162, 610–632.
- Stixrude, L., Lithgow-Bertelloni, C., 2011. Thermodynamics of mantle minerals - II. Phase equilibria. *Geophys. J. Int.* 184, 1180–1213.
- Stixrude, L., Wassermann, E., Cohen, R.E., 1997. Composition and temperature of Earth's inner core. *J. Geophys. Res.* B 102, 24729–24739.
- Sturhahn, W., Jackson, J.M., Lin, J.-F., 2005. The spin state of iron in minerals of Earth's lower mantle. *Geophys. Res. Lett.* 32, 1–5.
- Tarits, P., Mandéa, M., 2010. The heterogeneous electrical conductivity structure of the lower mantle. *Phys. Earth Planet. In.* 183, 115–125.
- Thomas, C.W., Liu, Q., Agee, C.B., Asimow, P.D., Lange, R. a., 2012. Multi-technique equation of state for Fe_2SiO_4 melt and the density of Fe-bearing silicate melts from 0 to 161 GPa. *J. Geophys. Res.* 117, 1–18.
- Tonks, W.B., Melosh, H.J., 1993. Magma ocean formation due to giant impacts. *J. Geophys. Res.* 98, 5319–5333.
- Torchio, R., Monza, a., Baudelet, F., Pascarelli, S., Mathon, O., Pugh, E., Antonangeli, D., Itié, J.P., 2011. Pressure-induced collapse of ferromagnetism in cobalt up to 120 GPa as seen via X-ray magnetic circular dichroism. *Phys. Rev. B* 84, 5–8.

Chapter 7 References

- Trampert, J., Deschamps, F., Resovsky, J., Yuen, D., 2004. Probabilistic tomography maps chemical heterogeneities throughout the lower mantle. *Science* 306, 853–6.
- Tsuzuki, A., Sago, S., Hirano, S.-I., Naka, S., 1984. High temperature and pressure preparation and properties of iron carbides Fe_7C_3 and. *J. Mater.* 19, 2513–2518.
- Vanpeteghem, C.B., Angel, R.J., Ross, N.L., Jacobsen, S.D., Dobson, D., Litasov, K.D., Ohtani, E., 2006. Al, Fe substitution in the MgSiO_3 perovskite structure: A single-crystal X-ray diffraction study. *Phys. Earth Planet. In.* 155, 96–103.
- Verhoeven, O., Mocquet, A., Vacher, P., Rivoldini, A., Menvielle, M., Arrial, P., Choblet, G., Tarits, P., Dehant, V., Hoolst, T.V., 2009. Constraints on thermal state and composition of the Earth's lower mantle from electromagnetic impedances and seismic data. *J. Geophys. Res.* 114, B03302.
- Vocadlo, L., Brodholt, J., Dobson, D.P., Knight, K.S., Marshall, W.G., Price, G.D., Wood, I.G., 2002. The effect of ferromagnetism on the equation of state of Fe_3C studied by first-principles calculations. *Earth Planet. Sci. Lett.* 203, 567–575.
- Volkert, C.A., Minor, A.M., 2007. Focused ion beam micromachining. *MRS Bull.* 32, 389–399.
- Weigel, C., Cormier, L., Calas, G., Galois, L., Bowron, D.T., 2008. Nature and distribution of iron sites in a sodium silicate glass investigated by neutron diffraction and EPSR simulation. *J. Non-Cryst. Solids* 354, 5378–5385.
- Williams, Q., Garnero, E.J., 1996. Seismic evidence for partial melt at the base of Earth's mantle. *Science* 273, 1528–1530.
- Wood, B.J., 1993. Carbon in the core. *Earth Planet. Sci. Lett.* 117, 593–607.
- Wood, B.J., Pawley, a., Frost, D.R., 1996. Water and carbon in the Earth's mantle. *Philos. T. R. Soc. A* 354, 1495–1511.
- Wood, I.G., Vočadlo, L., Knight, K.S., Dobson, D.P., Marshall, W.G., Price, G.D., Brodholt, J., 2004. Thermal expansion and crystal structure of cementite, Fe_3C , between 4 and 600 K determined by time-of-flight neutron powder diffraction. *J. Appl. Crystallogr.* 37, 82–90.
- Xu, W., Naaman, O., Rozenberg, G., Pasternak, M., Taylor, R., 2001. Pressure-induced breakdown of a correlated system: The progressive collapse of the Mott-Hubbard state in RFeO_3 . *Phys. Rev. B* 64, 1–9.
- Yoo, C.S., Cynn, H., Söderlind, P., Iota, V., 2000. New $\beta(\text{fcc})$ -Cobalt to 210 GPa. *Phys. Rev. Lett.* 84, 18–21.
- Yoshino, T., Ito, E., Katsura, T., Yamazaki, D., Shan, S., Guo, X., Nishi, M., Higo, Y., Funakoshi, K., 2011. Effect of iron content on electrical conductivity of ferropericlase with implications for the spin transition pressure. *J. Geophys. Res.* 116, B04202.
- Zha, C., Hemley, R.J., Mao, H., Duffy, T.S., Meade, C., 1994. Acoustic velocities and refractive index of SiO_2 glass to 57.5 GPa by Brillouin scattering. *Phys. Rev. B* 50, 13105–13112.

Chapter 7 References

- Zhang, F., Oganov, A.R., 2006. Valence state and spin transitions of iron in Earth's mantle silicates. *Earth Planet. Sci. Lett.* 249, 436–443.
- Žák, T., Jirásková, Y., 2006. CONFIT: Mössbauer spectra fitting program. *Surf. Interface Anal.* 38, 710–714.

Erklärung

Hiermit erkläre ich, dass ich die vorliegende Arbeit selbständig verfasst und keine anderen als die von mir angegebenen Quellen und Hilfsmittel benutzt habe.

Ferner erkläre ich, dass ich nicht anderweitig versucht habe, mit oder ohne Erfolg eine Dissertation einzureichen und auch keine gleichartige Doktorprüfung an einer anderen Hochschule endgültig nicht bestanden habe.

Bayreuth, den 9. November 2012

Clemens Prescher